ISBN 978-82-326-1336-6 (printed version)
ISBN 978-82-326-1337-3 (electronic version)
ISSN 1503-8181

NTNU
Norwegian University of
Science and Technology

Qin Zhang

Doctoral Thesis

Doctoral theses at NTNU, 2015:340

Qin Zhang

Image Processing for Ice Parameter Identification in Ice Management

NTNU
Norwegian University of
Science and Technology
Faculty of Engineering
Science and Technology
Department of MarineTechnology

NTNU
Norwegian University of
Science and Technology

Doctoral theses at NTNU, 2015:340

NTNU

Qin Zhang

Image Processing for Ice Parameter Identification in Ice Management

Thesis for the degree of Philosophiae Doctor

Trondheim, December 2015

Norwegian University of Science and Technology
Faculty of Engineering
Science and Technology
Department of MarineTechnology

NTNU
Norwegian University of
Science and Technology

NTNU
Norwegian University of Science and Technology

Thesis for the degree of Philosophiae Doctor

Faculty of Engineering
Science and Technology
Department of MarineTechnology

ISBN 978-82-326-1336-6 (printed version)
ISBN 978-82-326-1337-3 (electronic version)
ISSN 1503-8181

Doctoral theses at NTNU, 2015:340

Printed by Skipnes Kommunikasjon as

Abstract

Various types of remotely sensed data and imaging technology will aid the development of sea-ice observation to, for instance, support estimation of ice forces critical to Dynamic Positioning (DP) operations in Arctic waters. The use of cameras as sensors for offshore operations in ice-covered regions will be explored for measurements of ice statistics and ice properties, as part of a sea-ice monitoring system. This thesis focuses on the algorithms for image processing supporting an ice management system to provide useful ice information to dynamic ice estimators and for decision support. The ice information includes ice concentration, ice types, ice floe position and floe size distribution, and other important factors in the analysis of ice-structure interaction in an ice field.

The Otsu thresholding and k-means clustering methods are employed to identify the ice from the water and to calculate ice concentration. Both methods are effective for model-ice images. However, the k-means method is more effective than the Otsu method for the sea-ice images with a large amounts of brash ice and slush.

The derivative edge detection and morphology edge detection methods are used to try to find the boundaries of the ice floes. Because of the inability of both methods to separate connected ice floes in the images, the watershed transform and the gradient vector flow (GVF) snake algorithm are applied.

In the watershed-based method, the grayscale sea-ice image is first converted into a binary image and the watershed algorithm is carried out to segment the image. A chain code is then used to check the concavities of floe boundaries. The segmented neighboring regions that have no concave corners between them are merged, and over-segmentation lines are removed automatically. This method is applicable to separate the seemingly connected floes whose junctions are invisible or lost in the images.

In the GVF snake-based method, the seeds for each ice floe are first obtained by calculating the distance transform of the binarized image. Based on these seeds, the snake contours with proper locations and radii are initialized, and the GVF snakes are then evolved automatically to detect floe boundaries and separate the connected floes. Because some holes and smaller ice pieces may be contained inside larger floes, all the segmented ice floes are arranged in order of increasing size after segmentation. The morphological cleaning is then performed to the arranged ice floes in sequence to enhance their shapes, resulting in individual ice floes identification. This method is applicable to identify non-ridged ice floes, especially in the marginal ice zone and managed

ice resulting from offshore operations in sea-ice.

For ice engineering, both model-scale and full-scale ice will be discussed. In the model-scale, the ice floes in the model-ice images are modeled as square shapes with predefined side lengths. To adopt the GVF snake-based method for model-ice images, three criteria are proposed to check whether it is necessary to reinitialize the contours and segment a second time based on the size and shape of model-ice floe. In the full-scale, sea-ice images are shown to be more difficult than the model-ice images analyzed. In addition to non-uniform illumination, shadows and impurities, which are common issues in both sea-ice and model-ice image processing, various types of ice (e.g., slush, brash, etc.), irregular floe sizes and shapes, and geometric distortion are challenges in sea-ice image processing. For sea-ice image processing, the "light ice" and "dark ice" are first obtained by using the Otsu thresholding and k-means clustering methods. Then, the "light ice" and "dark ice" are segmented and enhanced by using the GVF snake-based method. Based on the identification result, different types of sea-ice are distinguished, and the image is divided into four layers: ice floes, brash pieces, slush, and water. This then makes it possible to present a color map of the ice floes and brash pieces based on sizes. It also makes it possible to present the corresponding ice floe size distribution histogram.

Acknowledgements

This thesis is submitted to the Norwegian University of Science and Technology (NTNU) for partial fulfilment of the requirements for the degree of philosophiae doctor (PhD).

This doctoral work has been performed at the Department of Marine Technology, NTNU, Trondheim, with main supervisor Prof. Roger Skjetne and with co-supervisors Prof. Aleksey Marchenko and Prof. Sveinung Løset.

This doctoral work was supported by the Research Council of Norway through the KMB: Arctic DP project 199567/I40, with industrial partners Statoil, Kongsberg Maritime, and DNV GL.

First, I would like to express my sincere gratitude to Prof. Roger Skjetne for giving me the PhD opportunity to work on the Arctic DP project and for guiding me during the whole period of my PhD study. I would like to thank him for helping me to overcome a number of scientific challenges, improving my confidence to go forward, and teaching me how to become an independent and good researcher. I would also like to thank him for the advice in other aspects of life.

Second, I would like to thank Prof. Aleksey Marchenko and his wife, Nataly Marchenko, for their supports during my study abroad at the University Centre in Svalbard (UNIS). Thanks to Prof. Sveinung Løset for kindly and patiently teaching me the knowledge of Arctic engineering.

I would like to acknowledge the Centre for Research-based Innovation SAM-CoT through Project No. 203471, the MARTEC ERA-NET project DYPIC through Project No. 196897, and the Hamburg Ship Model Basin for providing experimental data. I would also like to acknowledge the support of PhD Esten Grøtli and NORUT for organizing the remote sensing UAV mission to Ny-Ålesund and the support of Raed Lubbard for organizing the research cruise with KV Svalbard.

I would like to express thanks to Arctic DP members and my colleagues: Prof. Lars Imsland, Bo Zhao, Francesco Scibilia, Ivan Metrikin, Joakim Haugen, Ulrik Jørgensen, Øivind Kjerstad, Petter Norgren, Laxminarayan Thorat, and Andreas Reason Dahl, for their cooperations during my work.

Most of all, I am deeply grateful to my families. I am greatly indebted to my mother, Yuzhi Chen; my father, Zhijian Zhang; my elder sister, Yu Zhang; and my little nephew, Minxuan Xiao in China for their consistent and unconditional support and encouragement throughout the years. Without them, I couldn't go

so far. My special appreciations go to my husband, Biao Su, for his love, confidence, and support in me, my work, and my life.

Qin Zhang
March 12, 2015
Trondheim, Norway

Contents

Abstract i

Acknowledgements iii

Contents vii

List of Tables ix

List of Figures xiv

1 Introduction 1
- 1.1 Research Background . . . 1
  - 1.1.1 Arctic DP system . . . 2
  - 1.1.2 Imagery for ice observation . . . 6
- 1.2 Ice Parameter Identification . . . 7
  - 1.2.1 Ice concentration . . . 7
  - 1.2.2 Ice types . . . 8
  - 1.2.3 Ice floe size and floe size distribution . . . 9
- 1.3 Objective, Scope, and Applications . . . 9
- 1.4 Ice Image Data Source . . . 11
  - 1.4.1 Model-ice image data . . . 11
  - 1.4.2 Sea-ice image data . . . 12
- 1.5 Thesis Structure, Research Methods, and Contributions . . . 13
- 1.6 Publications . . . 17

2 Ice Pixel Detection 19
- 2.1 Thresholding . . . 19
  - 2.1.1 The Otsu thresholding method . . . 20
  - 2.1.2 Local thresholding . . . 21
- 2.2 Clustering . . . 21
  - 2.2.1 The k-means clustering . . . 22
- 2.3 Experimental Results and Discussion . . . 23

2.3.1 Model-ice image test 23
2.3.2 Sea-ice image test 35

3 Ice Edge Detection **41**
3.1 Derivative Edge Detection 41
3.2 Morphology Edge Detection 44
3.2.1 Erosion and dilation 45
3.2.2 Morphological gradient 47
3.3 Experimental Results and Discussion 49

4 Watershed-based Connected Ice Floe Segmentation **55**
4.1 Watershed transform 55
4.2 Neighboring-region Merging 57
4.3 Concave detection by chain code 57
4.4 Experimental Results and Discussion 62

5 Ice Image Segmentation and Ice Floe Identification **67**
5.1 Snake Models 68
5.1.1 Parametric Snake Model 69
5.1.2 Gradient Vector Flow Snake 70
5.2 Contours Initialization for the GVF Snake 71
5.2.1 The location of initial contour 72
5.2.2 The shape and size of the initial contour 72
5.2.3 Automatic contour installation based on the distance transform 74
5.3 Ice Image Segmentation 77
5.4 Ice Shape Enhancement 79
5.5 Discussion 81

6 Model Ice Image Processing **83**
6.1 Locating Initial Contours for Crowded Model-ice Floes 83
6.2 Algorithm Overview 85
6.3 Experimental Results and Discussions 87
6.3.1 Sub-image tests 87
6.3.2 Overall ice tank image 89
6.3.3 Model-ice floe modeling 94
6.3.4 Ice concentration 95
6.4 Application: Monitoring Maximum Floe Size 97

7 Sea-ice Image Processing **99**
7.1 Ice Image Processing Methods 100
7.1.1 Sea-ice pixel extraction 100
7.1.2 Sea-ice edge detection 101

7.1.3 Sea-ice shape enhancement 104
7.1.4 Ice types classification and floe size distribution 106
7.2 Case Studies and Discussions 106
7.2.1 Simple sea-ice image case 106
7.2.2 Complex sea-ice image case 109
7.2.3 Sea-ice modeling 115
7.3 Applications on Ice Engineering 120
7.3.1 Application 1: Processing of shipboard sea-ice image with fisheye distortion 120
7.3.2 Application 2: The 360-degree camera system and ice image processing 122

8 Conclusion **127**

A Geometric Orthorectification **131**

B Fisheye Calibration **135**

References **136**

List of Tables

1.1 Managed ice conditions in the test runs, target values (model-scale). 12
1.2 CryoWing technical specifications. 14
1.3 Visible spectrum camera specifications. 14

2.1 Ice concentrations derived from different methods. 27
2.2 Average IC after reaching saturation in all test runs. 33
2.3 Ice concentrations of sea-ice images. 35

4.1 Number of over- and under-segmented lines compared with manual inspection. 65

6.1 The parameter values of the GVF field for each sub-image. . . 93

List of Figures

1.1 Arctic oil and gas map, from USGS (2008) 2
1.2 Dynamic positioning (DP) vessel 3
1.3 Topology of an Arctic DP system. 4
1.4 Ice management (IM) 5
1.5 Ice intelligence system 6
1.6 Image processing system in support to Arctic DP operation . . 7
1.7 Location of site for the remote sensing mission 13
1.8 The CryoWing UAV operation at Ny-Ålesund (Photographer: Qin Zhang). 14
1.9 Executed UAV flight path, from NORUT 15

2.1 Bimodal histogram 20
2.2 Overall tank image for run no. 5100 23
2.3 Histogram of the overall tank image for run no. 5100 24
2.4 Run no. 5100. Global Otsu method 24
2.5 Run no. 5100. Locall Otsu method 24
2.6 Run no. 5100. Global Otsu method 25
2.7 Overall tank image for run no. 5200 25
2.8 Histogram of the overall tank image for run no. 5200 25
2.9 Run no. 5200. Global Otsu method 26
2.10 Run no. 5200. Locall Otsu method 26
2.11 Run no. 5100. Global Otsu method 26
2.12 Original frame in the video and pre-processed frame 28
2.13 Frames of run no. 5100 at 816s and ice detection 29
2.14 Time-varying IC of run no. 5100 based on Otsu and k-means 29
2.15 Time-varying IC of run no. 5100 based on Otsu and k-means at 801-851s 30
2.16 Frames of run no. 5200 at 600s and ice detection 30
2.17 Time-varying IC of run no. 5200 based on Otsu and k-means 31
2.18 Frames of run no. 5300 at 700s and ice detection 31
2.19 Time-varying IC of run no. 5300 based on Otsu and k-means 32

2.20 Frames of run no. 5400 at 1400s and ice detection 32
2.21 Time-varying IC of run no. 5400 based on Otsu and k-means 33
2.22 Time-varying IC of run nos. 5100-5400 based on Otsu thresholding 34
2.23 Sea-ice Image 1 and ice detection 36
2.24 Sea-ice Image 2 and ice detection 37
2.25 Sea-ice Image 3 and ice detection 38
2.26 Ice identification of Figure 2.25(a) by k-means with 3 clusters 39

3.1 Examples of the edge detector masks and the first-order derivatives they implement 43
3.2 Examples of the edge detector masks and the second-order derivatives they implement 44
3.3 The process of erosion 46
3.4 The process of dilation 48
3.5 Edge detections of overall model-ice tank image for run no. 5200 49
3.6 Edge detections of model-ice frames for run no. 5100 at 816s . 50
3.7 Edge detections of sea-ice image 51
3.8 Comparison of the derivative and the morphology methods. . . 52
3.9 Weakly connected ice floes separation 53

4.1 The topological surface of a complemented grayscale ice image 56
4.2 Watershed-based segmentation 57
4.3 Flow chart of the watershed-based segmentation and neighboring-region merging 58
4.4 Numbering scheme of the chain code 59
4.5 A boundary's chain code and its first difference 60
4.6 Concave detection by chain code 62
4.7 Watershed-based connected ice floe segmentation 63
4.8 Segmented floes and floe size distribution 64
4.9 Examples of over- and under-segmentation 64
4.10 An example of the ambiguously segmented lines 66

5.1 External forces. 70
5.2 Initial contours located at different positions and their corresponding curve evolutions 73
5.3 Initial circles with different radii and their curve evolutions . . 75
5.4 Contour initialization algorithm based on distance transform . 76
5.5 The procedure of ice segmentation algorithm 78
5.6 The segmentation of ice floe image with speckle 79
5.7 Morphological cleaning by using a 2×2 square structuring element 80

5.8 Ice shape enhancement result of Figure 5.6(b) 81

6.1 Crowded model-ice floes segmentation 84
6.2 Model-ice floe segmentation result 1 87
6.3 Model-ice floe segmentation result 2 88
6.4 Model-ice floe segmentation result 3 88
6.5 Model-ice floe segmentation result 4 88
6.6 Image border effects 89
6.7 Overall model-ice tank image 90
6.8 Ice floe identification after illumination correction and floe size distribution 91
6.9 Error segmentation by using improper parameters 92
6.10 Overlapping floes image segmentation 92
6.11 Final model-ice floe identification result and floe size distribution 93
6.12 Light reflection impact 94
6.13 Ice floe rectangularization 95
6.14 Rectangular floe size distribution and its error differences . . . 96
6.15 Model-ice video processing 97
6.16 Maximum floe size entering the protected vessel 98

7.1 Original sea-ice image 100
7.2 "Light ice" extracted by the thresholding method 101
7.3 Ice extraction using the k-means method 102
7.4 "Dark ice" image 102
7.5 Sea-ice segmentation image 103
7.6 Sea-ice shape enhancement 105
7.7 Labeled and colorized ice pieces 105
7.8 Sea-ice image classification 107
7.9 Floe size distribution histogram of Figure 7.8(a) 108
7.10 Residue ice (boundary pixels) 108
7.11 Aerial image of the marginal ice zone 109
7.12 Identification result producing four layers for Figure 7.11 . . . 110
7.13 Floe and brash ice size distribution for Figure 7.11 111
7.14 Floe size distribution histogram obtained from Figure 7.13 . . 111
7.15 Sea-ice image with perspective distortion 112
7.16 Local segmentation procedure 113
7.17 Ice floe and brash size distribution without orthorectification . 114
7.18 Ice floe and brash size distribution after orthorectification. . . . 116
7.19 Ice floe size distribution histogram of Figure 7.18. 116
7.20 Sea-ice modeling for Figure 7.13 118
7.21 Comparison between identification and modification results. . 118
7.22 Polygonized floe size distribution and its error diffrences . . . 119

7.23 Shipboard sea-ice image with fisheye distortion and its segmentation result. 121
7.24 Floe and brash ice size distribution of Figure 7.23(b) 122
7.25 360-degree panorama image 123
7.26 Identified ice floe distribution of Figure 7.25 124
7.27 Time-varying ice concentration of pushing test 125

A.1 Geometric orthorectification 132
A.2 Orthorectification result 134

B.1 Fisheye calibration 136
B.2 Fisheye calibration result 137

Chapter 1

Introduction

1.1 Research Background

In 2008, the U.S. Geological Survey (USGS) estimated that the area north of the Arctic circle has 90 billion barrels of undiscovered, technically recoverable oil, $1,670$ trillion cubic feet of technically recoverable natural gas, and 44 billion barrels of technically recoverable natural gas liquids in 25 geologically defined potential areas. Taken together, these resources account for about 22% of the undiscovered, technically recoverable resources in the world. Breaking it down by resource, the Arctic accounts for about 13% of the undiscovered oil, 30% of the undiscovered natural gas, and 20% of the undiscovered natural gas liquids in the world (see Figure 1.1). About 84% of the estimated resources are expected to occur offshore [1]. Moreover, the distance of traditional sailing routes from northern European to northern Pacific ports can be reduced by one-third if the Arctic shipping routes are reliable. The sailing time and costs for transportation will thereby be significantly saved. It will bring tremendous commercial and economic benefits. The Arctic Human Development Report (AHDR) stated that oil and gas exploration, production, and transportation would be the driving force behind the formal development of the Arctic economy in the coming decades.

However, the exploration of the Arctics is still in the early stages. It is more technically and physically challenging than for any other environment due to low temperatures, remoteness, darkness, and the prevalence of ice. Despite this, with increases in technology and continuing high oil prices, the region is now receiving the interest of the petroleum industry. The Norwegian petroleum supplier industry is seeing an increased demand for offshore vessels capable of performing safe and green dynamic positioning (DP) operations in ice-covered

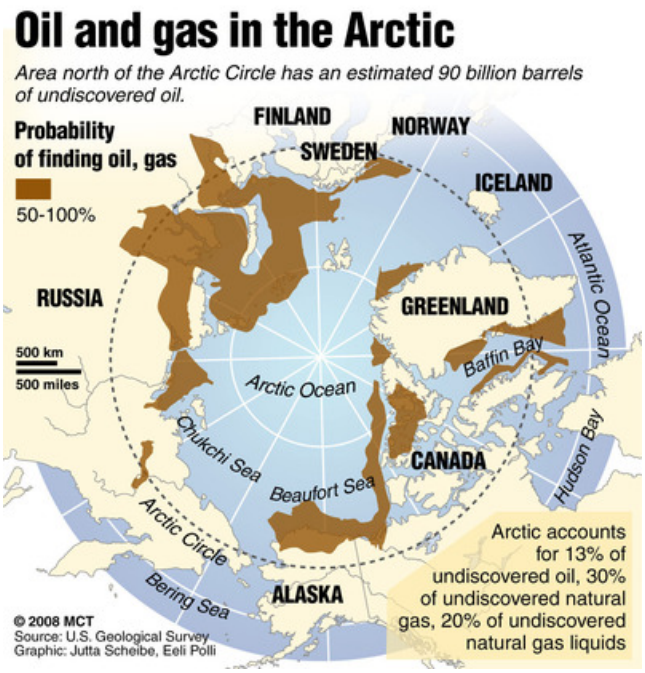

Figure 1.1: Arctic oil and gas map, from USGS (2008).

Arctic areas. It is expected that such operations will be more frequent in the future due to exploration drilling, the possibility for hydrocarbon production, and other emerging advanced marine operations north of the polar circle. Despite a few expeditions involving DP operations in ice conditions, in practice today, there is no experience with and little knowledge of DP operations in Arctic ice conditions available, neither in the public domain nor among companies. Therefore, developing new knowledge and insights into technological methods, operational procedures, and limitations are essential for performing safe commercial operations in a very harsh and ecologically sensitive Arctic environment. Many research works on Arctic technology and operations have been conducted, such as [2, 3, 4, 5].

1.1.1 Arctic DP system

A DP vessel maintains its position and heading (fixed location or pre-determined track) exclusively by means of active thrusters, as shown in Figure 1.2 [6]. The environmental forces acting on the vessel directly influence its stationkeeping capability. Position reference systems (e.g., Global Navigation Satellite Systems, Hydroacoustic Position Reference Systems, Taut Wire) and sensors

(e.g., gyrocompasses, inertial measurement unit, wind sensors, wave sensors, and current sensors) provide DP control computer with information about the vessel's position and the environmental forces. The computer control system thereby ensures automatically maintaining a desired position and heading by giving setpoints to the propellers and thrusters [7, 8].

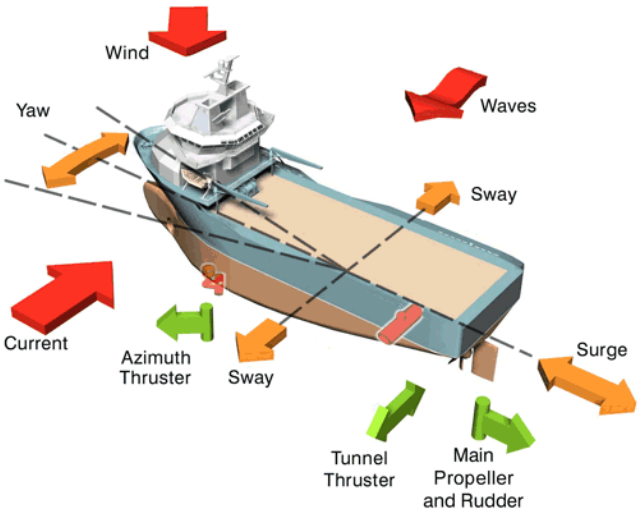

Figure 1.2: Dynamic positioning (DP) vessel. Courtesy: Kongsberg Maritime.

DP technology has been developed and successfully used for decades in different offshore operations, such as offshore oil drilling, coring, and pipelaying. The environmental loads usually arise from wind, waves, and current. However, findings have shown that the conventional DP system is infeasible for operations in Arctic ice conditions. This is because the nature of ice forces is highly varying and significantly different from other environmental forces. Multiple problems will challenge the use of DP operations in ice [9]:

- Forces acting on the vessel.
- Forces caused by ice dynamics.
- Turning yaw moment.
- Changes in ice movement direction.
- Predictability of ice load behaviour.
- New type of thruster control allocation.
- Forbidden or required sectors for ice flow management.
- Specific methods to lower ice loads.

- Ice management and operational risk control.

Ice forces involve a direct interaction with a rigid mass. Ice concentration, ice thickness, floe size distribution, ice material properties, and relative velocity between the vessel and ice are important factors affecting the vessel's station-keeping capabilities under ice loads. Figure 1.3 shows the topology proposal of the Arctic DP system [10].

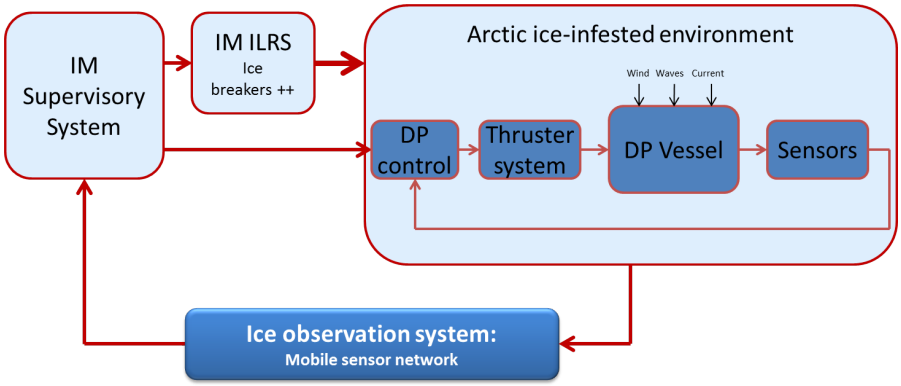

Figure 1.3: Topology of an Arctic DP system. Courtesy: Skjetne et al.. [10]

To determine the appropriate actions for a DP vessel and avoid damage from ice actions, ice management (IM) is typically employed in the stationary operations with ice-breaking vessels to cover the approach and for providing safe operation and safe exit when required [3, 4, 11, 12]. IM ice load reduction system (ILRS) is the sum of all activities in which the objective is to reduce or avoid actions from any kind of ice features [13]. This will include, but is not limited to, the following:

- Detection, tracking, and forecasting of sea-ice, ice ridges and icebergs.
- Threat evaluation.
- Physical ice management, such as ice breaking and iceberg towing.
- Procedures for disconnection of offshore structures applied in search for or production of hydrocarbons.

An Arctic DP vessel operating in a wide range of ice conditions usually depends on an ice management system where icebreakers manage the incoming ice into smaller pieces to reduce the ice loads on the ship hull as shown in Figure 1.4 [14]. By maintaining the heading toward the direction of ice drift motion, the operating vessel is able to minimize the loads on the hull by only

letting the smallest projected area of the vessel undergo friction from the broken ice. The DP controller is constructed for the vessel to cope with the resulting large variations in the managed ice loads and to maintain its position and heading [15, 16, 17].

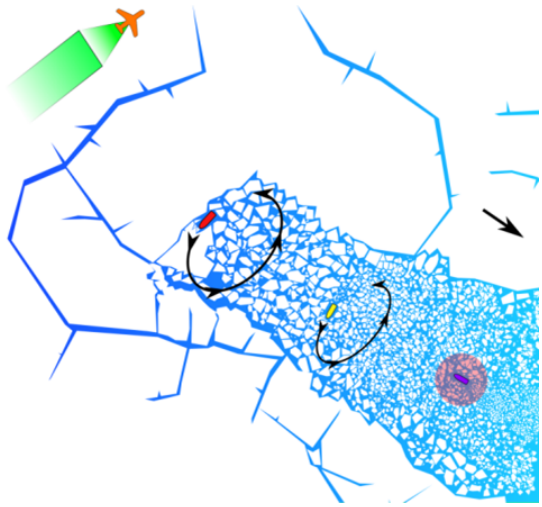

Figure 1.4: Ice management (IM). The ice breakers break the incoming ice into smaller pieces to reduce the ice loads on the ship hull. Courtesy: J. Haugen [14]

To detect, track, and forecast ice features, an ice intelligence system is required in an IM system. The ice intelligence system, as shown in Figure 1.5, is the process of collecting and analyzing relevant information about the ice environment in a region of interest. This includes surface ice intelligence scouting tools, such as satellites, airborne recognizance, shipbord sensors, radar systems, drift buoys, and visual observations [18], and subsurface ice intelligence scouting tools such as sonars and unmanned underwater vehicles (UUVs) [19, 20]. Thus, a complete ice intelligence system will consist of several sensor platforms for obtaining the required ice information. The collected ice information, as the input to some computer software, will be analyzed to provide useful output information. The output information constitutes visualization to human operators, suggested operational decisions, and tasks to other automated systems [21].

Figure 1.5: Ice intelligence system collects and analyzes the ice environment information from surface and subsurface scouting tools. Illustration by Bjarne Stenberg. Copyright: NTNU

1.1.2 Imagery for ice observation

Various types of ice are in the ice-covered regions. Ice concentration, ice floe size distribution, and ice types are important parameters in the field observations of sea-ice to estimate ice loads. Because the sizes of the ice floes and brash ice can range from about one meter to a few kilometers, the temporally and spatially continuous field observations of sea-ice are necessary for marine activities. To that end, one of the best ways to observe the ice conditions in the oceans is by using aerial or nautical imagery and applying the digital visual image techniques to ice observation.

Various types of remote sensing technologies and corresponding image processing algorithms for analysis of sea-ice statistics and ice properties have been developed. Satellite remote sensing has been widely used to extract ice concentration [22], classify ice types [23, 24, 25], and analyze ice floes [26, 27]. Digital visual image techniques are also applied to ice observation. [26] measured the sea-ice floe size distribution by manually identifying the ice floes from aerial photographs. In [28], a sea-ice digital image collection and processing system was utilized to monitor the ice parameters in the JZ20-2 oil-gas field of the Liaodong Bay, and ice thickness, ice velocity, and ice concentration in the Bohai Sea are determined by this system. In the model tests performed by [29], a machine vision system based on boundary detection and thresholding was used to analyze and record the ice conditions surrounding the vessel in real time.

The analysis of image information obtained from cameras can enhance the reliability through image correlation and improve definition through image complementation. The reliability and complementation can also help to obtain a more comprehensive and distinct environment. Image processing can reduce or suppress the ambiguities, incompleteness, uncertainties, and errors of the object and the environment by multi-image information extraction and synthesis. Finally, it can make the information of the object and environment more accurate and reliable by maximizing the use of image information from a variety of information sources.

Due to those advantages, the use of cameras as sensors on mobile sensor platforms (e.g., unmanned vehicles) in Arctic DP operations will be explored for ice motion monitoring to characterize ice conditions, as shown in Figure 1.6 [30]. Cameras as sensors have the potential of continuous measurements with high precision, which is particularly important for providing detailed localized information of sea-ice to ensure safe operations of structures in ice-covered regions [21].

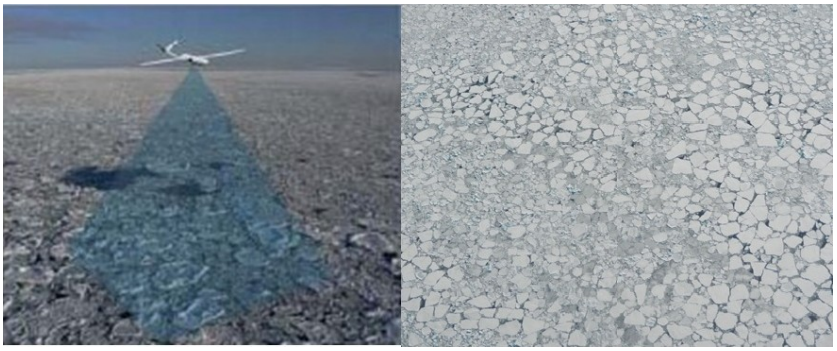

Figure 1.6: Image processing system in support to Arctic DP operation. The cameras are used as sensors on the unmanned aerial vehicle (UAV) to monitor the conditions of sea-ice.

1.2 Ice Parameter Identification

1.2.1 Ice concentration

Ice concentration (IC) is the ratio of ice on unit area of sea surface. It has been identified as one of the most influential parameters on the magnitude of experienced forces during model tests [31, 32]. To obtain IC from a visual ice image, only the visible ice can be considered, including brash ice and, if visible

in the image, submerged ice. With the image area, height of image taken above the ice sheet, and the segmentation, which is the identification of the ice from water, the actual area of sea-ice and sea surface can be derived. However, the actual domain area is not necessary for calculating the ice concentration.

In simplified terms, ice concentration from a digital visual image is, in our research, defined as, as a fraction of the whole sea surface domain area, as the area of sea surface covered by visible ice observable in the 2D visual image taken vertically from above. Hence, it is the ratio of the number of pixels of visible ice to the total number of pixels within the image domain. An image may contain parts of land or other non-relevant areas. Herein, the domain area is therefore, an effective area within the image. The ice concentration is then given by the following:

$$\begin{aligned} IC &= f(image\ area,\ height\ above\ ice\ sheet,\ segmentation) \\ &= \frac{Area\ of\ all\ visible\ ice}{Actual\ domain\ area} \\ &= \frac{Number\ of\ pixels\ of\ visible\ ice\ in\ the\ image\ domain}{Total\ number\ of\ pixels\ in\ the\ image\ domain} \end{aligned} \tag{1.1}$$

1.2.2 Ice types

Sea-ice is any form of ice found at sea that has originated from the freezing of sea water [33]. Different types of sea-ice have different physical properties. Since one generally assumes that brash ice has a dampening effect in models for calculating ice pressure and ice forces, it may be more convenient to estimate the distribution between three classes: the ratio of ice floes, the ratio of brash ice, and the ratio of water.

As defined in [34, 35, 36],

- Floe is any relatively flat piece of sea-ice 20 m or more across. It is subdivided according to horizontal extent. A giant flow is over 10 km across; a vast floe is 2 - 10 km across; a big floe is 500 to 2000 m across; a medium floe is 100 to 500 m across; and a small floe is 20 to 100 m across.
- Ice cake is any relatively flat piece of sea-ice less than 20 m across.
- Brash ice is accumulations of floating ice made up of fragments not more than 2 m across and the wreckage of other forms of ice. It is common between colliding floes or in regions where pressure ridges have collapsed.
- Slush is snow that is saturated and mixed with water on land or ice surfaces, or as a viscous floating mass in water after heavy snowfall.

For simplicity, the size of sea-ice piece is the only criterion to distinguish ice floe and brash ice in this thesis. That is, any relatively flat piece of sea-ice 2 m or more across is considered as "ice floe", while any relatively flat piece of sea-ice less than 2 m across is considered as "brash ice (piece)". The remaining of ice pixels are considered to be "slush".

1.2.3 Ice floe size and floe size distribution

The estimation of ice floe size and floe size distribution among the "ice floes" gives an important set of parameters from ice images.

In image processing, the ice floe size can be determined by the number of pixels in the identified floe. If the focal length f and camera height are available, the actual size in SI unit of the ice floes and floe size distribution can also be calculated [37] by converting the image pixel size to its SI unit size.

In practice other parameters are typically used to represent the size of the floes, such as the "representative diameter". The algorithms proposed in this thesis produce a complete database of all floes in the image, where the pixels of each floe is stored. Hence, any 2D geometric parameter can easily be calculated from the database. The floe size distribution can thus be easily recalculated based on the "representative diameter" of the floes.

1.3 Objective, Scope, and Applications

The objective of this thesis is to develop image processing algorithms to extract useful information from the ice images. This information can supplement data provided by other sensors onboard the ship or a buoy in form of ice concentration, ice floe boundaries, and ice types in the surrounding region. These methods can be used further to develop tools, based on the processed ice data, that can be applied for decision support in Arctic offshore operations.

The scope of the present work includes the following:

- Segmenting ice regions from water regions.
- Detecting ice floe boundaries and locating floe positions.
- Classifying different types of sea-ice.
- Estimating ice concentration and floe size distribution.

This process results in an identified model of broken ice floes that can be used in several ways:

- To quantify the efficiency of ice management for Arctic offshore drilling operations and automatically detect hazardous conditions, for example, by identifying large floes that escape the icebreakers operating upstream of the stationary drilling vessel. The size and shape of those floes, as identified by the image processing system, can be compared with the maximal allowed values, and a warning signal can be sent to the risk management system. Eventually, a decision to disconnect the floater might be taken based on the identified operational ice conditions.

- The managed ice concentration and ice floe sizes are essential parameters in the empirical formulas that estimate the ice loads on stationary Arctic offshore structures [38, 39]. One of the largest concerns of ice management modeling is accurately predicting not just the mean floe size resulting from an ice management system, but also the floe size distribution [40].

- Individual ice floes identified by the image processing system, can be used to initialize high-fidelity numerical models, such as those in [41, 42, 43, 44, 45, 46]. Individual snapshots of identified ice floes can be used to validate the numerical models at various moments in time by matching the simulated ice fields with the actual ones.

- The ice floe size and shape distribution, calculated from an identified ice field, can be used in synthetic ice field generators. These generators draw polygons from the distribution and use packing algorithms to place the polygons on a 2D plane. Such synthetic ice fields may be used to study various packing configurations with the same ice concentrations and floe size distributions as well as the variability of the resulting ice loads on an offshore structure.

- The identification of the ice field may provide early warning of an ice compaction event, which can be dangerous if the ice-structure interaction mode changes from a “slurry flow”-type to a “pressured ice”-type, as defined by [47] and discussed in [39].

- Finally, the ice-drift speed and direction (velocity) can be estimated by applying an image analysis to sequential frames. The ice-drift velocity is an important parameter for ice management because it poses requirements on the speed of icebreaking vessels and may indicate an approaching ice drift reversal scenario (which usually happens when the ice drift tends to zero velocity).

In addition to the above application areas, the ice floe identification algorithm may potentially help to illuminate the momentum exchange from atmosphere to ice discussed in [48], the melting rate of ice floes discussed in [49], and the possibly of providing a clue to the understanding of ice-floe formation processes, as discussed in [27].

1.4 Ice Image Data Source

This thesis focuses on ice information extraction from both model- and sea-ice images. The model-ice images were obtained from Hamburgische Schiffbau-Versuchsanstalt (HSVA) Ice Model Basin [50, 31], and the sea-ice images were obtained from an unmanned aerial vehicle (UAV) mission [30].

1.4.1 Model-ice image data

DP experiments in model ice were carried out in the ice tank at HSVA in the summer of 2011. In these experiments, the behavior of two different ships in a broken-ice field were studied.

Experimental setup

In the research project "Dynamic Positioning in Ice Covered Waters (DYPIC)" [51], two different model ships have been tested at HSVA - an Arctic drillship and a polar research vessel. Each vessel was tested both in free running and oblique towing configurations. For image processing, the analysis is limited to the drillship in the oblique towing mode, based on the test campaign conducted in May 2011. Different heading and velocity profiles were tested. In the analyzed runs, the heading was constant at 180° and the velocity of the towing carriage with the model was increased halfway. By doing this, the full-scale ice-drift velocity of 0.25 knots was simulated in the first part of the test and 0.50 knots in the second part.

A managed ice condition was obtained by cutting the level ice layer into predefined ice floe shapes. Four different types of ice fields were tested, varying in ice concentration and ice floe size distribution, as shown in Table 1.1. The runs were sequentially executed, starting with run no. 5100. This initial ice field was prepared by cutting a 54-meter long ice sheet into pieces and distributing them over 64 meters of the tank length.

The cutting procedure was as follows. First, several strips of ice were cut in the longitudinal direction of the ice tank. One strip of 1.50 m width, four strips of 1.00 m width, and nine strips of 0.50 m width coincide with the percentages recorded in Table 1.1. Next, these strips were cut off such that the length was equal to the width of the strip, resulting in square ice floes. For run 5200 a number of floes were taken out of the basin in order to reduce the ice concentration. For run 5300, all present ice floes were cut into half diagonally. Finally, the removed ice floes were reinserted, but cut in half, in run 5400.

Table 1.1: Managed ice conditions in the test runs, target values (model-scale).

Run no.	Ice Concentration [%]	Floe size 1 (45%) [m]	Floe size 2 (40%) [m]	Floe size 3 (15%) [m]
5100	86	0.50	1.00	1.50
5200	70	0.50	1.00	1.50
5300	70	0.25	0.50	0.75
5400	86	0.25	0.50	0.75

Ice conditions were captured by several means. First, a top-view camera was used before each test run to take 28 pictures over the total ice-covered basin. Stitching these photos together resulted in a complete overview of the ice floe distribution in the ice tank. Second, a top-view video camera moving along with the carriage and model was used to capture the local conditions around the model vessel during each run. Other video cameras were installed as well in order to investigate the behavior of the model ship in the broken ice. Photographs were also taken manually during the tests.

1.4.2 Sea-ice image data

A remote sensing mission to determine ice conditions was performed by the Northern Research Institute (NORUT) at $78°55'N$ $11°56'E$, Hamnerabben, Ny-Ålesund (see Figure 1.7) from May 6th to 8th, 2011. The objectives of this mission were to observe and learn from UAV operation in the Arctic and obtain remotely sensed data of sea-ice features from a mobile sensor platform.

A CryoWing [52] [53] UAV, as shown in Figure 1.8, was used as a mobile sensor platform for the mission. This UAV was designed for cryospheric measurements and environmental monitoring. It has flexibility in coverage and in spatial and temporal resolution, which are three important sensor-platform attributes. The technical specification of CryoWing is found in Table 1.2. The basic instrumentation of the CryoWing is an onboard computer that controls the different payload instruments, stores data to a solid-state disk, and relays

data to the ground. The onboard payload system has a GPS receiver and a 3-axis orientation sensor independent of the avionics system. The sensor device used in this analysis is a digital visual camera with specifications found in Table 1.3.

Figure 1.7: Location of site for the remote sensing mission.

The UAV flew in the inner part of Kongsfjorden close to a buoy that had been deployed on the ice cover (see Figure 1.9) to collect high-resolution images of sea-ice.

1.5 Thesis Structure, Research Methods, and Contributions

Chapter 1: Introduction. This chapter gives a brief introduction concerning background, motivation and objectives of this thesis. The definitions of ice concentration from a digital visual ice image, ice floe, brash ice and slush for this thesis are also given in this chapter.

Chapter 2: Ice Pixel Detection. This chapter presents the ice pixel detection methods for the calculation of ice concentration from ice images. The main contributions in this chapter are as follows:

Figure 1.8: The CryoWing UAV operation at Ny-Ålesund (Photographer: Qin Zhang).

Table 1.2: CryoWing technical specifications.

Weight	30 kg max take off weight
Wingspan	3.8 m
Cruise speed	100 - 120 km/h
Range/endurance	500 km / 5 h
Max altitude	2500 m dynamic range, 5000 m absolute
Payload capacity	Max 15 kg including fuel load
Engine	Two stroke gasoline
Navigation	GPS
Ground equipment	PC with modem, RC control
Flight	Autonomous, but under ground control
Communication	GSM or Iridium satellite modem

Table 1.3: Visible spectrum camera specifications.

Camera model	Canon EOS 450D
Lens type	Canon EF 28 mm f/2.8
Aperture value	11.00
Sensor	22.2 $\times$14.8 mm CMOS
ISO	200
Dimensions	4290 $\times$2856
Resolution	960 dpi
Exposure time	1/250 sec
Sampling frequency	0.66 Hz

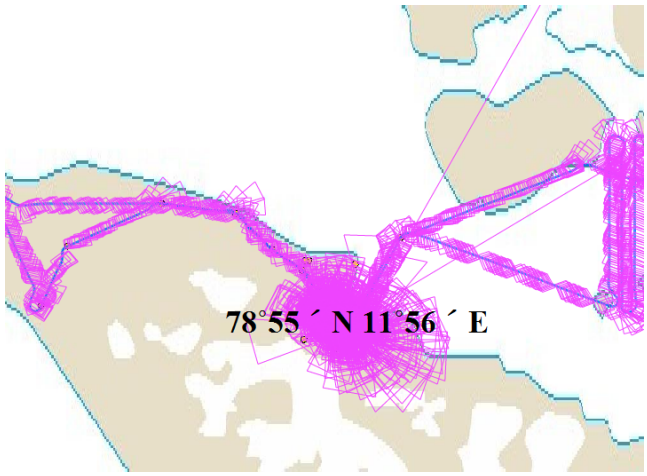

Figure 1.9: Executed UAV flight path, from NORUT.

1. Introduce the Otsu thresholding and k-means clustering methods for the extraction of ice pixels from ice images.

2. Compare these two methods and their applicable scope.

This work was published in [50] and [30].

Chapter 3: Ice Edge Detection. This chapter introduces two common edge detection methods for the detection of ice floe boundaries. The main contributions in this chapter are as follows:

1. Apply the derivative edge detection and morphology edge detection methods to detect ice boundaries.

2. Compare and analyze the pros and cons of these two methods.

This work was published in [50] and [30].

Chapter 4: Watershed-based Connected Ice Floe Segmentation. This chapter adopts the watershed transform to separate seemingly connected sea-ice floes, and proposes a neighboring-region merging algorithm to reduce the over-segmentation automatically. The main contributions in this chapter are as follows:

1. Give an assumption of ice floe shapes.

2. Apply chain code to identify the concave corners of the segmented floe boundaries and automatically remove the over-segmentation lines caused by watershed.

3. Discuss the limitations and applicable scope of the method.

This work was published in [54].

Chapter 5: Ice Image Segmentation and Ice Floe Identification. This chapter adopts the gradient vector flow (GVF) snake algorithm to identify ice floe boundaries, and morphology cleaning algorithm to enhance ice shapes. The main contributions in this chapter are as follows:

1. Determine the required initial contours for the GVF snake.
2. Propose an automatic initial contours algorithm for the GVF snake based on the distance transform.
3. Identify ice floe boundaries and separate the connected floes into individual ones.
4. Enhance ice shapes and identify individual ice floes based on the morphology cleaning algorithm.

This work was published in [55, 56, 57].

Chapter 6: Model-ice Image Processing. This chapter presents the methods to process model-ice images. The main contributions in this chapter are as follows:

1. Propose three criteria to determine the seeds for crowed model-ice floes based on their characters.
2. Identify the individual model-ice floes from crowed model-ice images based on the proposed criteria and the method proposed in Chapter 5.
3. Obtain model-ice floe position, area, and size distribution.
4. Propose a model of the managed ice field's configuration.

This work was published in [55].

Chapter 7: Sea-ice Image Processing. This chapter presents the methods for the analysis of sea-ice images. The main contributions in this chapter are as follows:

1. Derive "light ice" and "dark ice" from the sea-ice image by using both Otsu thresholding and k-means clustering methods, and identify individual ice pieces.
2. Derive four different layers - ice floes, brash pieces, slush, and water - from the sea-ice image based on the identification result, and derive the floe (brash) size distribution.

3. Give case studies to illustrate the sea-ice image processing procedure, including local processing and geometric calibration.

4. Propose a model of sea-ice field's configuration.

5. Give applications on ice engineering.

This work was published in [56, 57].

Chapter 8: Conclusion. This chapter summarizes the thesis work, and provides suggestions for future work.

Appendix A: Geometric Orthorectification. This chapter gives a geometric orthorectification method for calibrating the distortion caused by the oblique angle in the sea-ice image in Chapter 7.

Appendix B: Fisheye calibration. This chapter gives a geometric method for calibrating the fisheye distortion caused by the GoPro camera in the sea-ice image in Chapter 7.

1.6 Publications

Journal

1. **Zhang, Q.** and Skjetne, R. "Image processing for sea-ice floe identification and size distribution". *IEEE Transactions on Geoscience and Remote Sensing*. Vol. 53, No. 5, Pages 2913-2924, May 2015.

2. **Zhang, Q.**, Skjetne, R., Metrikin, I., and Sveinung Løset. "Image processing for ice floe analyses in broken-ice model testing". *Cold Region Science and Technology*. Vol.111, Pages 27-38, March 2015.

3. **Zhang, Q.** and Skjetne, R. "Image techniques for identifying sea-ice parameters". *Journal of Modeling, Identification and Control*. Vol. 35, No. 4, Pages 293-301, December 2014.

Conference

1. **Zhang, Q.**, Skjetne, R., and Su, B. "Automatic image segmentation for boundary detection of apparently connected sea-ice floes". In *Proceedings of the 22nd International Conference on Port and Ocean Engineering under Arctic Conditions.* Espoo, Finland, June 09-03, 2013.

2. **Zhang, Q.**, van der Werff, S., Metrikin, I., Sveinung Løset, and Skjetne, R. "Image processing for the analysis of an evolving broken-ice field in model testing". In *Proceedings of 31st International Conference on*

Ocean, Offshore and Arctic Engineering. Rio de Janeiro, Brazil, July 01-06, 2012.

3. **Zhang, Q.**, Skjetne, R., Sveinung Løset, and Marchenko, A. "Digital image processing for sea ice observation in support to arctic DP operation". In *Proceedings of 31st International Conference on Ocean, Offshore and Arctic Engineering.* Rio de Janeiro, Brazil, July 01-06, 2012.

4. van der Werff, S., Haase, A., Huijsmans, R., and **Zhang, Q.** "Influence of the ice concentration on the ice loads on the hull of a ship in a managed ice field." In *Proceedings of 31st International Conference on Ocean, Offshore and Arctic Engineering.* Rio de Janeiro, Brazil, July 01-06, 2012.

Chapter 2

Ice Pixel Detection

Ice concentration, as defined, is a binary decision of each pixel to determine whether it belongs to the class "ice" or to the class "water". From Equation 1.1, it is clear that, the identification of the ice pixels from water pixels is crucial to obtain the ice concentration from an ice image.

A digital visual image is a numeric representation of a two-dimensional picture, and it is composed of pixels, which are the smallest individual elements in the image. A pixel holds quantized values that represent the color or gray level of the image at a particular point. Based on that, ice is whiter than water, and the pixel values are different between ice and water in normal conditions. In this chapter, Otsu thresholding and k-means clustering methods are introduced to extract the ice pixels from open water in ice images. The work presented in this chapter was published in [30, 50].

2.1 Thresholding

The pixels in the same region have similar intensity, and thresholding is a natural way to segment such regions. The thresholding method is based on the pixel's gray-level. Assuming that an object is brighter than the background, the object and background pixels have intensity levels grouped into two dominant modes. The threshold T is selected to extract the objects from the background. Individual pixels are marked as "object" pixels if their value is greater than the threshold value and as "background" pixels otherwise, that is:

$$g(x,y) = \begin{cases} 1 & \text{if } f(x,y) \geq T, \\ 0 & \text{if } f(x,y) < T. \end{cases} \tag{2.1}$$

where $g(x, y)$ and $f(x, y)$ are the pixel values located in the x^{th} column, y^{th} row of the binary and grayscale image, respectively. Then, the grayscale image is turned into a binary image. The key to using the thresholding method is in how to select the threshold value, for which there are several different methods.

2.1.1 The Otsu thresholding method

The Otsu thresholding method [58] is one of the most common threshold segmentation algorithms. It is used to automatically perform histogram shape-based image thresholding. The assumptions of the Otsu thresholding method are as follows:

- The histogram (the distribution of gray value) is bimodal (see Figure 2.1).
- The illumination is uniform.

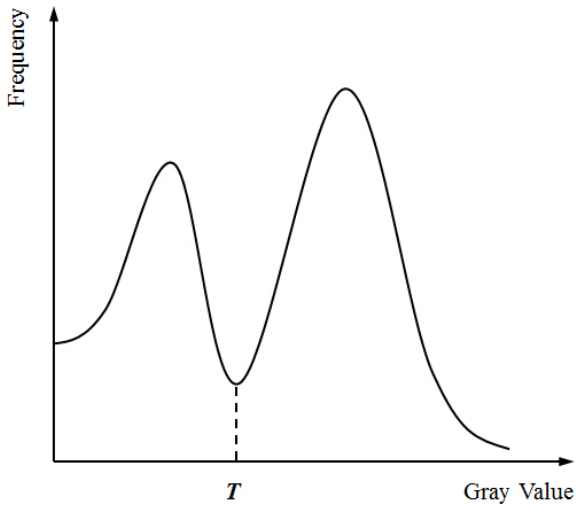

Figure 2.1: Bimodal histogram.

The histogram is divided into two classes (i.e., the pixels are identified as either foreground or background), and the goal is to find the threshold value that minimizes the within-class variance [58], given by:

$$\sigma_w^2(T) = \omega_1(T)\sigma_1^2(T) + \omega_2(T)\sigma_2^2(T), \tag{2.2}$$

where ω_1 and ω_2 are the probabilities of the two classes separated by a threshold T and σ_1 and σ_2 are the variances of these two classes. The threshold

with the maximum between-class variance also has the minimum within-class variance. According to [58], the between-class variance is given by:

$$\begin{aligned}\sigma_b^2(T) &= \omega_1(T)(\mu_1(T) - \mu(T))^2 + \omega_2(T)(\mu_2(T) - \mu(T))^2 \\ &\cong \omega_1(T)\omega_2(T)(\mu_1(T) - \mu_2(T))^2\end{aligned} \tag{2.3}$$

where μ_1 and μ_2 are the means of these two classes and where $\mu(T) = \omega_1(T)\mu_1(T) + \omega_2(T)\mu_2(T)$. This expression can also be used to find the best threshold and to update the threshold value iteratively.

2.1.2 Local thresholding

When a constant threshold value is used over the image, it is called global thresholding. Global threshold segmentation is simple, but it may fail if parts of the image are brighter (e.g., under the light) and parts are darker (e.g., under the shadow); these variations caused by changes in illumination across the scene.

Instead of using a single global threshold value, the local thresholding, which determines the thresholds locally, is typically required to handle uneven illumination problems. This method allows the threshold to continuously vary across the image. A common way is to divide the original image into sub-images and use different threshold values to segment each sub-image [59]. Local adaptive thresholding has a better performance for images with uneven illumination, but this method induces difficulties, such as subdivision and subsequent threshold estimation [59].

2.2 Clustering

Clustering is a technique for statistical data analysis. It is trying to find hidden structures in unlabeled data and assigning the unlabeled data into groups so that the data in one group are more similar to each other than to those in other groups. Several clustering algorithms exist [60]:

- Hierarchical: find successive clusters by using previously established clusters.
- Partitional: determine all clusters at once.
- Subspace: look for clusters that can only be seen in a particular projection of the data.

A distance measure is important in most clustering. This will determine the similarity of two calculated elements and affect the shape of the clusters. Whether the distance is symmetric or asymmetric, that is, whether the distance from *Object 1* to *Object 2* is the same as the distance from *Object 2* to *Object 1*, is also important. Some common symmetric distance functions include the following [60]:

- The Euclidean distance.
- The maximum norm.
- The Mahalanobis distance.
- The angle between two vectors.
- The Hamming distance.

Clustering analysis is a good way for a quick review of data, especially if the objects are classified into many groups [61]. Clustering is widely used, for instance, in machine learning, pattern recognition, image processing, information retrieval, and bioinformatics. In image processing, clustering is always applied for image segmentation.

2.2.1 The k-means clustering

K-means clustering is a widely used clustering method. It minimizes the within-cluster sum of distance to partition a set of data into k clusters. The step-by-step algorithm for this method is described below [62]:

Step 1: For image processing, a set of gray-levels is given:

$$f(x_1, y_1), f(x_2, y_2), \cdots, f(x_n, y_n). \tag{2.4}$$

Step 2: Partition this set into k clusters:

$$f_i(x_1, y_1), f_i(x_2, y_2), \cdots, f_i(x_{n_i}, y_{n_i}) \quad i = 1, 2, \cdots, k. \tag{2.5}$$

Step 3: Calculate the local means of each cluster:

$$c_i = \frac{1}{n_i} \sum_{m=1}^{n_i} f_i(x_m, y_m) \quad i = 1, 2, \cdots, k. \tag{2.6}$$

Step 4: Gray level $f(x_j, y_j) \quad (j = 1, 2, \cdots, n)$ belongs to set $p \quad (p = 1, 2, \cdots, k)$ if it has the shortest distance to set p than any other sets:

$$|f(x_j, y_j) - c_p| \leq |f(x_j, y_j) - c_i| \quad i = 1, 2, \cdots, k. \tag{2.7}$$

Iterate *Steps 3* and *4* until the local means are unchanged.

2.3 Experimental Results and Discussion

2.3.1 Model-ice image test

HSVA provided the image data from the performed tests. The data included two complete overview pictures from run nos. 5100 and 5200 (Table 1.1) and the videos of each of the four model test runs. One of the main parameters characterizing a broken-ice field is the ice concentration, defined as the fraction of the total water area covered by ice. In this section, image processing techniques are applied to derive the ice concentration in the model basin. Several points in time are analyzed in order to describe the evolution of the ice field. The Otsu thresholding and k-means clustering methods are applied for calculating the ice concentration in the vicinity of the model ship.

Overall tank image processing

The overall tank images were retrieved by stitching 28 top-view pictures taken before execution of the model tests. The total images in Figure 2.2 and Figure 2.7 show the distribution of ice floes over the tank length in run no. 5100 and run no. 5200, and Figure 2.3 and Figure 2.3 show their grayscale histograms.

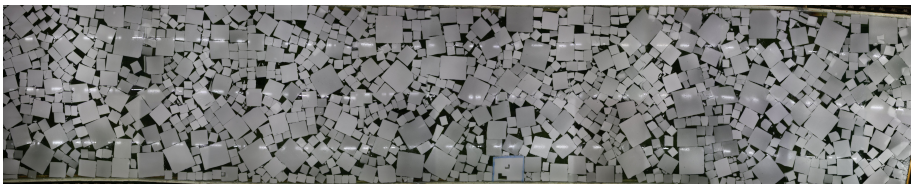

Figure 2.2: Overall tank image for run no. 5100. Target ice concentration 86%.

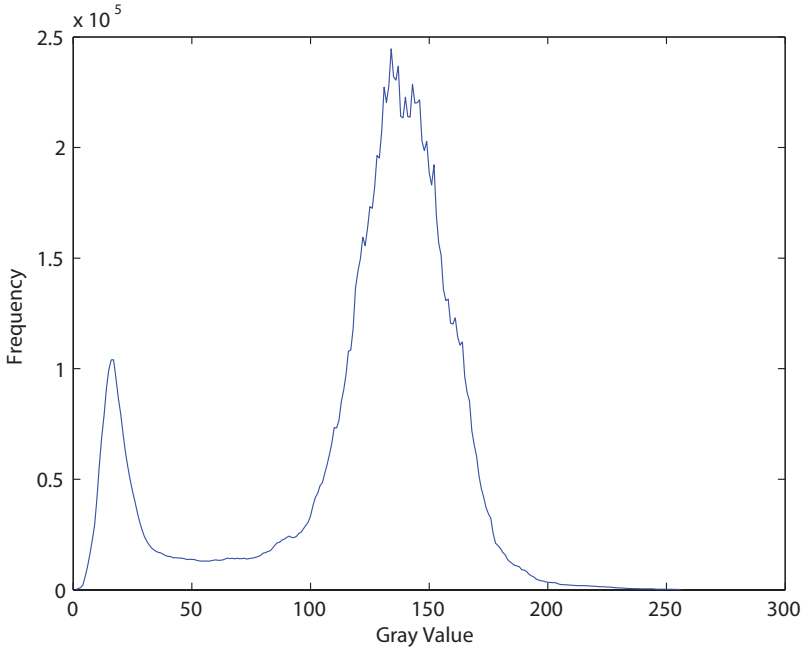

Figure 2.3: Histogram of the overall tank image for run no. 5100.

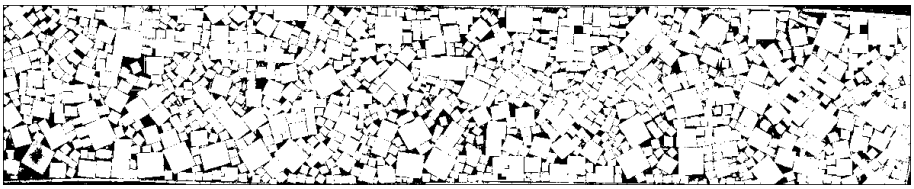

Figure 2.4: Run no. 5100. Global Otsu method, $IC = 83.17\%$, threshold $= 84$.

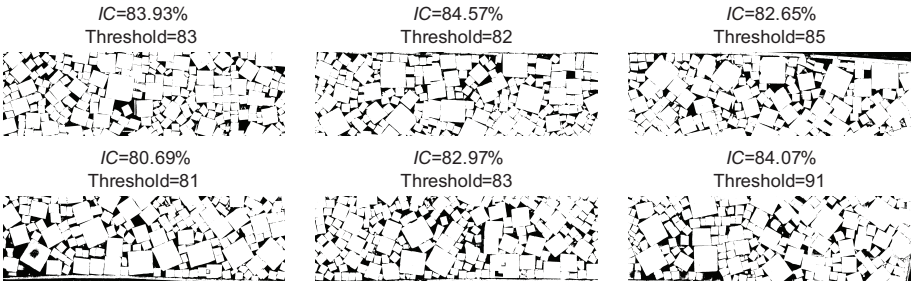

Figure 2.5: Run no. 5100. Local Otsu method, average $IC = 83.14\%$, average threshold $= 84$.

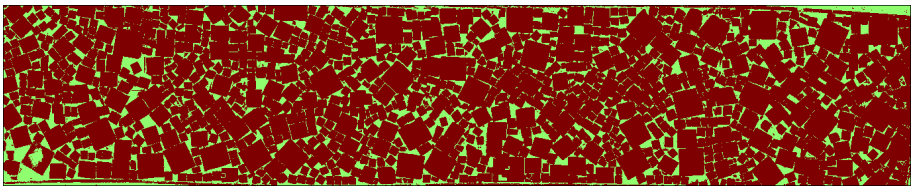

Figure 2.6: Run no. 5100. K-means method, 2 clusters, $IC = 82.86\%$.

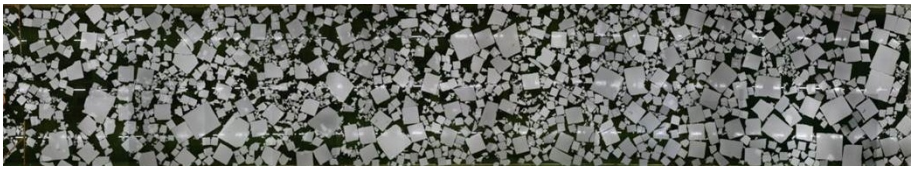

Figure 2.7: Overall tank image for run no. 5200. Target ice concentration 70%.

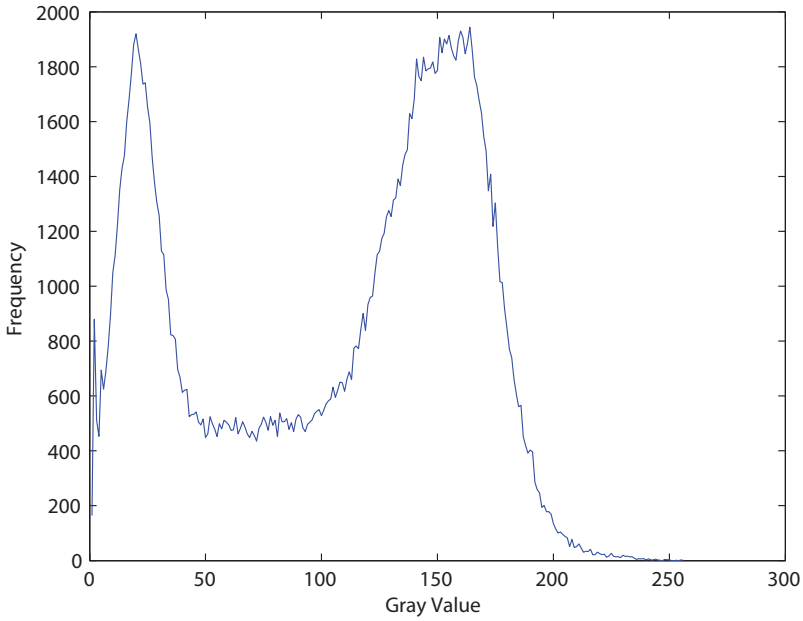

Figure 2.8: Histogram of the overall tank image for run no. 5200.

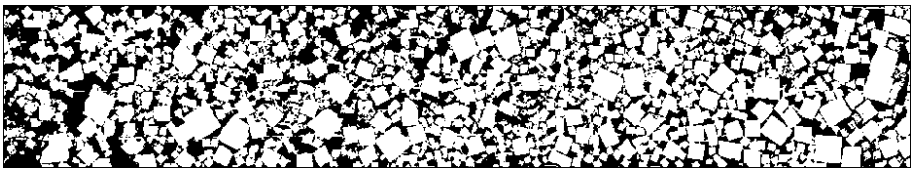

Figure 2.9: Run no. 5200. Global Otsu method, $IC = 62.51\%$, threshold $= 91$.

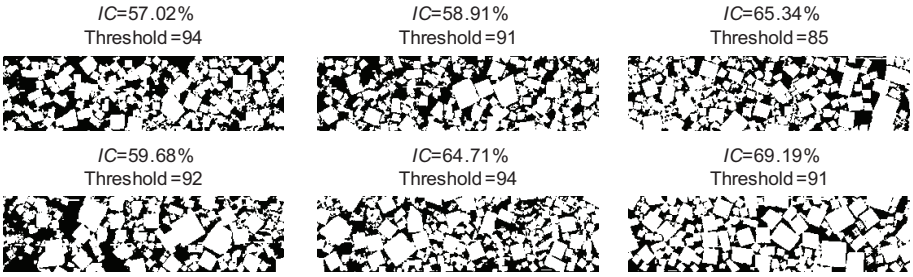

Figure 2.10: Run no. 5200. Local Otsu method, average $IC = 62.15\%$, average threshold $= 91$.

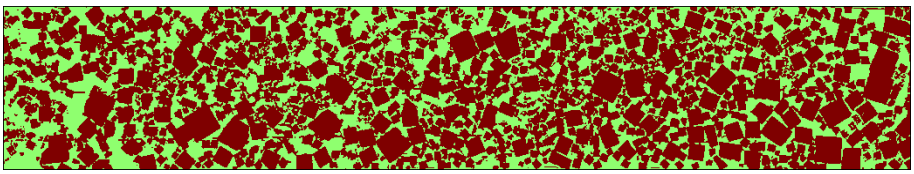

Figure 2.11: Run no. 5200. K-means method, 2 clusters, $IC = 62.00\%$.

The ice floes were segmented from the water by applying the global Otsu, local Otsu, and k-means methods. The ice concentrations were calculated individually based on these three methods. The results can be found in Figures 2.4 - 2.6 for run no. 5100 and in Figures 2.9 - 2.11 for run no. 5200.

The grayscale histograms of the overall tank images are clearly bimodal (see Figures 2.3 and 2.8 and compare with Figure 2.1). Moreover, the illumination of the overall tank image is almost uniform and only one type of ice existed in the tank. It means that both assumptions of the global Otsu thresholding method hold true. Hence, the differences in the calculated results between the global and local Otsu methods are small. Furthermore, the k-means method demonstrates results that are very close to the Otsu thresholding methods. Both of the methods are effective.

The results of the ice concentration analysis were compared with the target ice concentration values. The results are presented in Table 2.1. The ice concentrations derived from the different methods are approximately $3 - 8\%$ smaller than the targeted value. A source of error is the upper right corner of the image that sits outside the tank. However, the main reason is believed to be imperfect ice sheet preparation, where a portion of the ice sheet was lost during the ice redistribution. This led to decreased ice concentration compared to the target values.

Table 2.1: Ice concentrations derived from different methods.

Methods	Target Value	Global Otsu	Local Otsu	K-means
Run no. 5100	86%	83.17%	83.14%	82.86%
Run no. 5200	70%	62.50%	62.51%	62.00%

Model-ice video processing

A video is composed from a sequence of frames. The motions captured by the video are retrieved by analyzing a number of frames. The time variation of the ice concentration can be evaluated by plotting the individual frame analysis results over time.

The four videos supplied by HSVA are more than 24 minutes long with a frame rate of 25 fps. Before applying the algorithms to these videos, one frame per second is found sufficient, and each frame was fed to the program for further processing.

The distortion in the videos, caused by the fisheye camera, has not been calibrated. Therefore, the scale in the middle of the videos is larger than the

circumambience. This phenomenon has an insignificant effect on the boundary detection. However, it may have some influence on the analyses of the ice concentration and ice floe sizes.

The light sources in the ice tank were reflected by the water and the ice. Due to the bright characteristics of the lights, they may be identified as ice floes by the algorithm, and consequently, the ice concentration may be estimated slightly too high.

The impediments around the tank are removed, and the vessel in the middle bottom of the tank is eliminated by a black rectangle (see Figure 2.12). The vessel box removed from the images may slightly decrease the quality of the results for ice concentration.

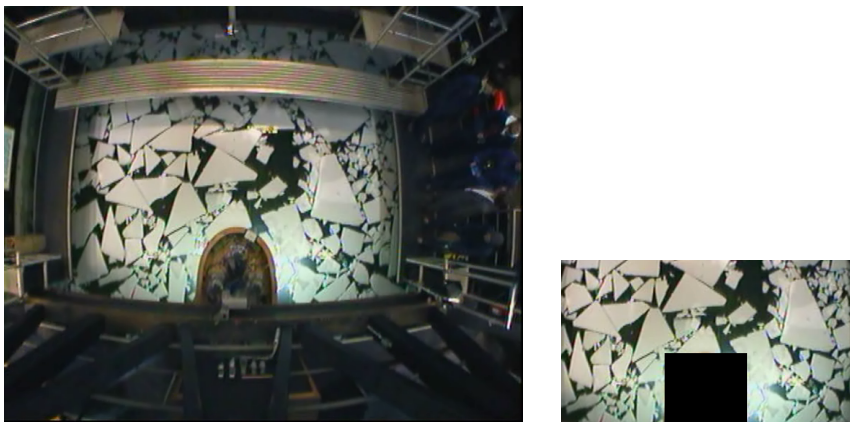

(a) One frame in the original video. (b) Domain image.

Figure 2.12: Original frame in the video and pre-processed frame. Run no. 5400.

The global Otsu and the k-means clustering methods were applied in the video processing to calculate the ice concentration as a function of time. The results are presented in Figures 2.13 - 2.21.

The analysis of the test run no. 5100 indicates that the ice concentration reached a limiting value of around 89% at approximately 200 s after the start of the test. This value is only 3% higher than the target value, and it is, therefore, concluded that the ice sheet was prepared well in this test run.

In the 5200 test run, the ice concentration reached a limit value of around 80% at approximately 300 s after the start of the test. This value is 10% higher than the target value, which is a large deviation. It is, therefore, concluded that the ice sheet should have been prepared better in this test run.

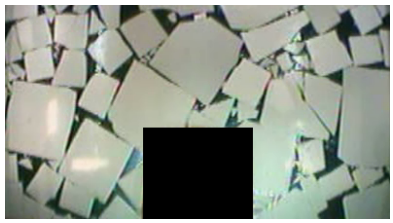

(a) Run no. 5100: Time=816s.

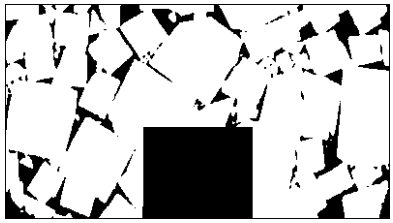

(b) Otsu, $IC = 87.26\%$, threshold $= 100$.

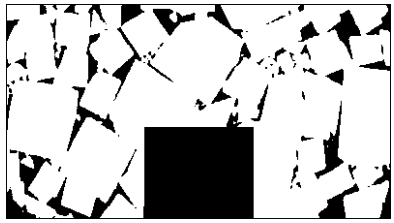

(c) K-means, $IC = 86.91\%$.

Figure 2.13: Frames of run no. 5100 at 816s and ice detection.

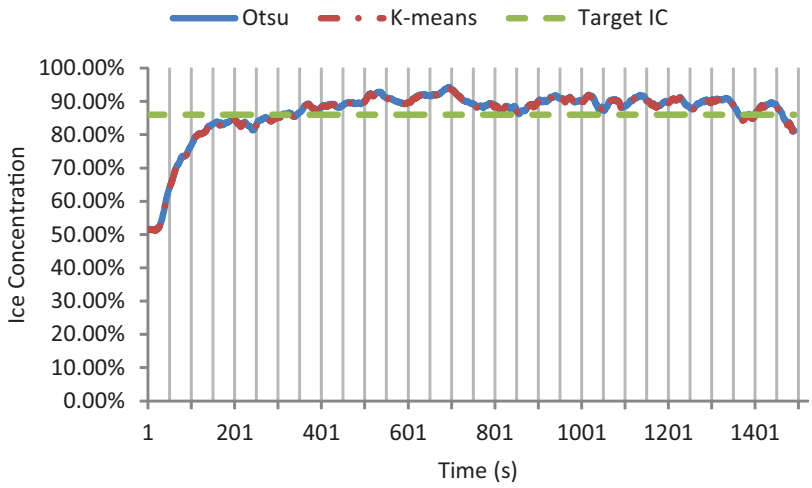

Figure 2.14: Time-varying IC of run no. 5100 based on Otsu and k-means. Target $IC = 86\%$.

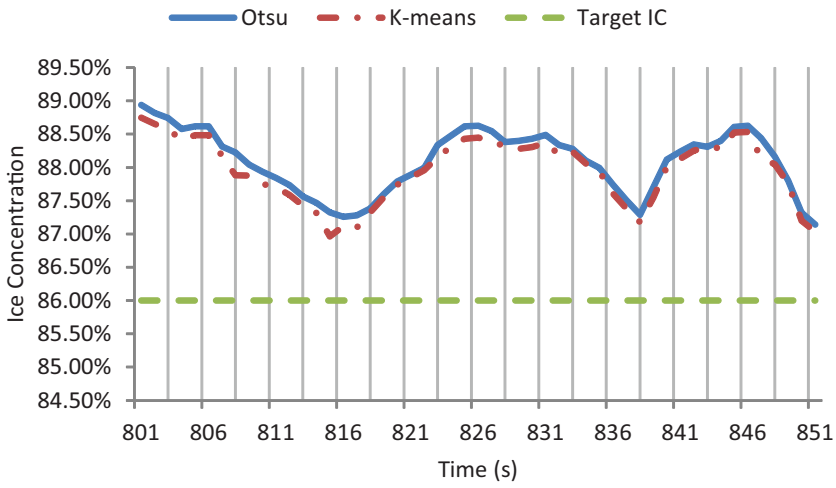

Figure 2.15: Time-varying IC of run no. 5100 based on Otsu and k-means at 801-851s. Target $IC = 86\%$.

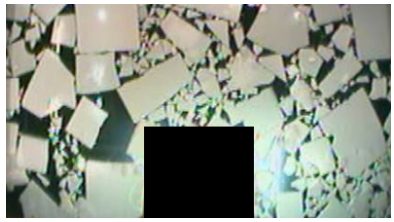

(a) Run no. 5200: Time=600s.

(b) Otsu, $IC = 80.79\%$, threshold $= 108$.

(c) K-means, $IC = 80.55\%$.

Figure 2.16: Frames of run no. 5200 at 600s and ice detection.

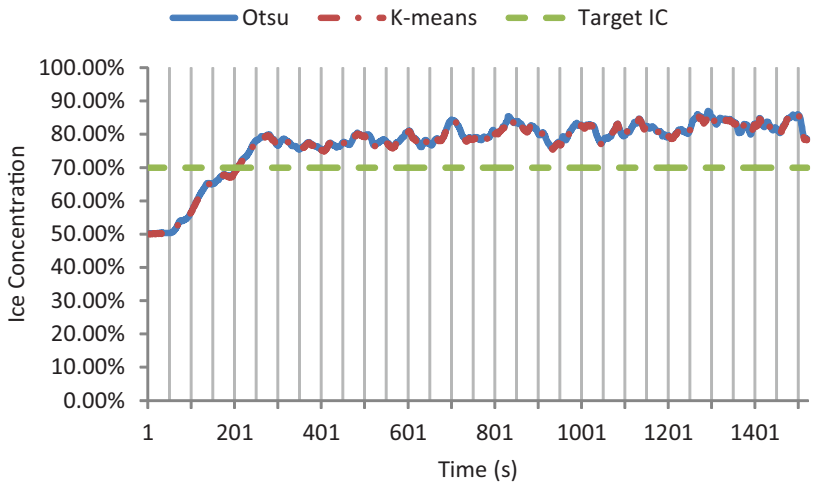

Figure 2.17: Time-varying IC of run no. 5200 based on Otsu and k-means. Target $IC = 70\%$.

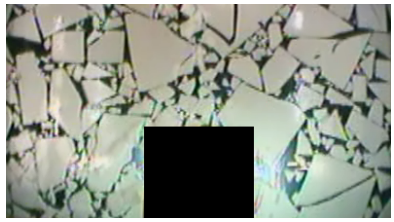

(a) Run no. 5300: Time=700s.

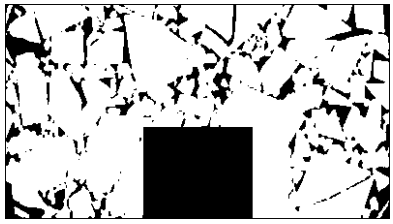

(b) Otsu, $IC = 85.33\%$, threshold $= 104$.

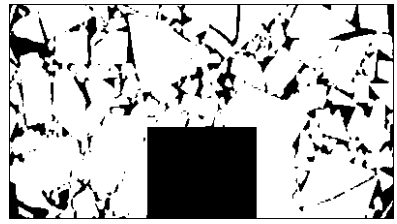

(c) K-means, $IC = 85.06\%$.

Figure 2.18: Frames of run no. 5300 at 700s and ice detection.

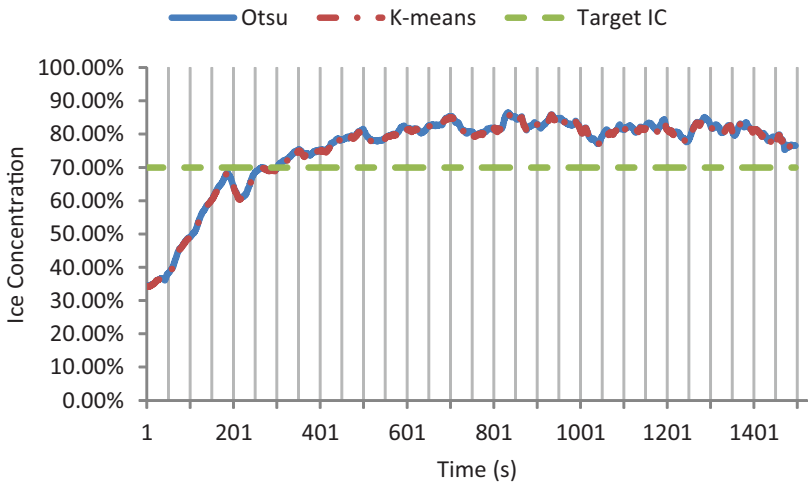

Figure 2.19: Time-varying IC of run no. 5300 based on Otsu and k-means. Target $IC = 70\%$.

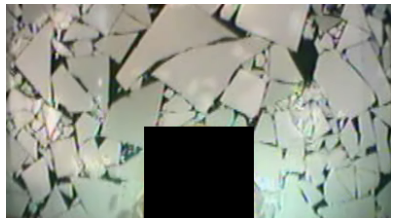

(a) Run no. 5400: Time=1400s.

(b) Otsu, $IC = 90.00\%$, threshold $= 98$.

(c) K-means, $IC = 89.81\%$.

Figure 2.20: Frames of run no. 5400 at 1400s and ice detection.

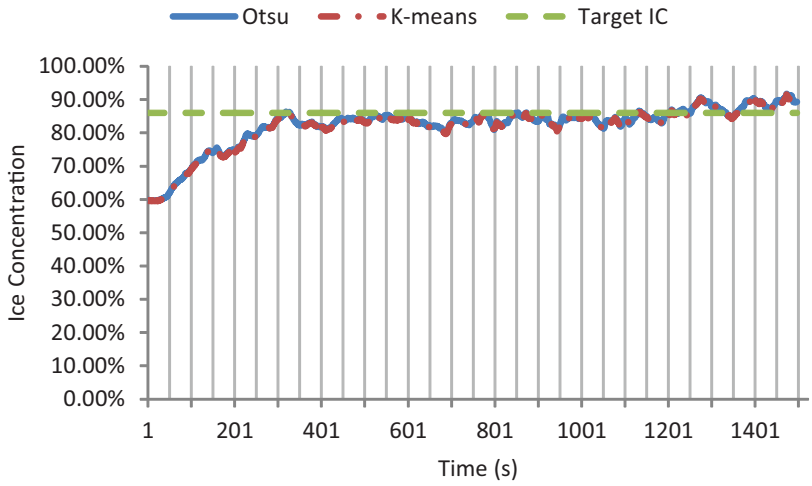

Figure 2.21: Time-varying IC of run no. 5400 based on Otsu and k-means. Target $IC = 86\%$.

In the 5300 test run, the ice concentration reached a limit value of around 82% at approximately 600 s after the start of the test. This value is 12% higher than the target value. Moreover, the effective length of the ice tank is almost halved due to the ice concentration buildup in the beginning of the test. Based on these two observations, it is possible to conclude that the ice sheet was not prepared correctly in this test run.

Finally, in test run no. 5400, the ice concentration reached a steady value of around 84% at approximately 300 s after the start of the test. However, in the end of the test, the ice concentration goes up to 90%, which is 4% higher than the target value. These deviations are considered relatively small, and it is concluded that the ice sheet was prepared properly in this test run.

Figure 2.22 shows the variation of the Otsu method's threshold in time for all test runs. The average ice concentrations after reaching the limiting values in all test runs are summarized in Table 2.2.

Table 2.2: Average IC after reaching saturation in all test runs.

Run no.	5100	5200	5300	5400
Start time (s)	200	300	600	300
Average IC	88.93%	80.39%	81.69%	84.83%

Reduced ice concentration in the initial part of the test runs (before conver-

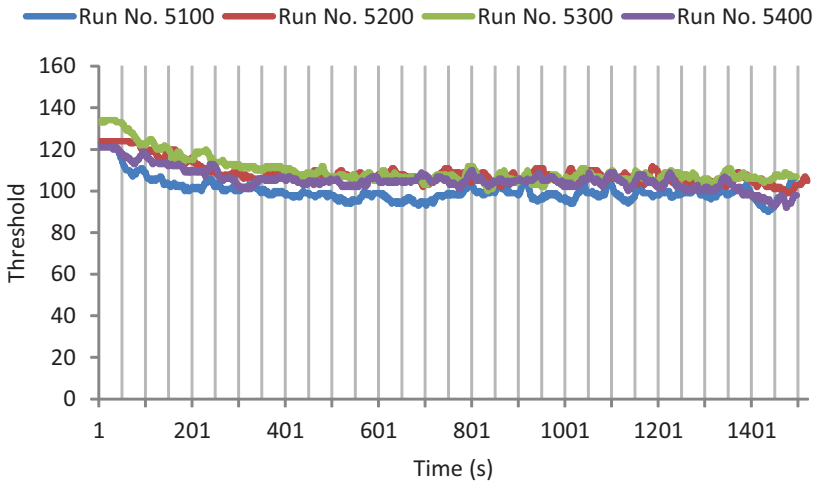

Figure 2.22: Time-varying IC of run no. 5100-5400 based on Otsu thresholding.

gence) is related to the model ship positioning. It is an unwanted phenomenon, since it reduces the effective length of the ice tank. It is recommended to develop mitigation procedures in the future to help avoid this issue.

In all test runs, it was observed that the ice concentration in the near vicinity of the model was reaching a limiting value of approximately $80 - 89\%$, irrespective of the starting ice concentrations and floe sizes. This phenomenon can be explained by the tank's wall effect. That is, the ice floes were compacted by the model ship toward the end of the basin, such that the ice concentration asymptotically approached a limiting value.

The results of the video processing confirm that the difference between the Otsu and the k-means methods is quite small. The differences between the target ice concentration and the actual values obtained from the image processing indicate that the broken ice sheet preparation procedures could be improved. Specifically, more attention could be paid to preparing ice sheets with low ice concentrations ($< 80\%$). By comparing the original images to the processed ones, both of these methods are effective if there is only one type of ice on the water.

2.3.2 Sea-ice image test

The results obtained from applying the Otsu thresholding and the k-means clustering methods to calculate the ice concentration for the model-scale experimental data can be considered satisfactory. In order to test the applicability of these methods for full-scale sea-ice observation, they are also applied to image data derived from the remote sensing mission at Ny-Ålesund in early May 2011 [30]. In k-means clustering, we divide the image into only two clusters. The first group represents sea-ice, and the other group represents water. Parts of the processed images and ice concentration results are presented in Figures 2.23 - 2.25. The calculated ice concentrations are summarized in Table 2.3.

Table 2.3: Ice concentrations of sea-ice images.

Image no.	1	2	3
Otsu	15.37%	32.84%	73.73%
K-means	15.65%	32.49%	96.50%

Figures 2.23 and 2.24, and their calculated ice concentrations in Table 2.3, show that the ice pixel detection using the Otsu thresholding method is similar to the detection using the k-means method by dividing the image into two clusters when the intensity values of all the ice pixels are significantly higher than water pixels. However, the Otsu thresholding method can only find "light ice" pixels. The "dark ice" (e.g., ice that is submerged in water, brash ice, slush), whose pixel intensity values are close to water pixels, may be lost. However, both "light ice" and "dark ice" are required to further identify the different types of sea-ice (the details are described in Chapter 7).

In order to identify more ice pixels, the k-means clustering method can be applied to divide the image into three or more clusters [62] [60]. In this research, we divided the image into three groups, which we roughly interpret as "ice cluster 1" with the highest average pixel grayscale in red regions, water with the lowest average pixel grayscale in blue regions, and "ice cluster 2" with the average pixel grayscale between in yellow regions. The "ice cluster 1" region contains most of the ice floes in the image, and the "ice cluster 2" region contains most of brash ice and slush in the image. The coverage of each cluster was also calculated. The result is presented in Figure 2.26.

By comparing the calculated results for Figure 2.25(a) based on Otsu (Figure 2.25(b)), k-means clustering method with 2 clusters (Figure 2.25(c)), and k-means clustering method with 3 clusters (Figure 2.26), it is the rather large content of brash ice and slush that results in the large difference between the ice concentration from Otsu and ice concentration calculated by k-means. Since

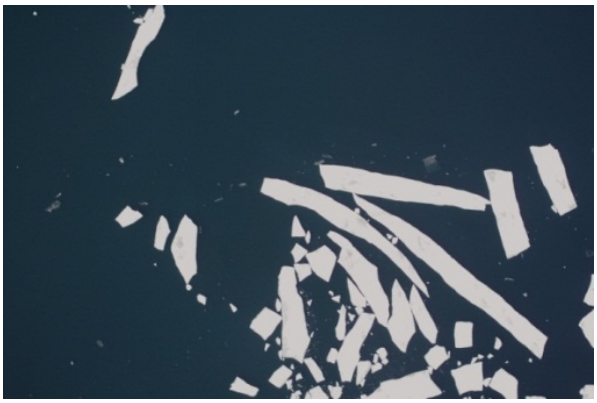

(a) Original sea-ice Image 1.

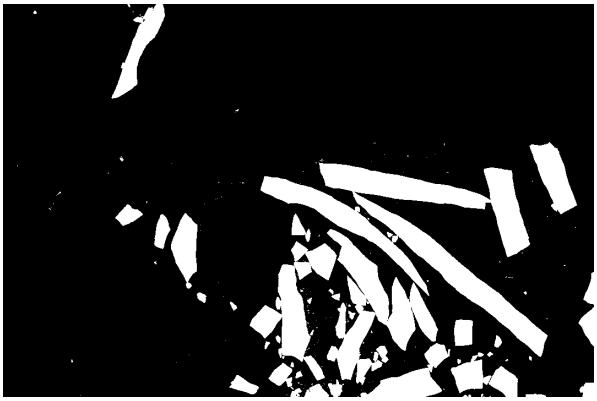

(b) Otsu thresholding method, $IC = 15.37\%$.

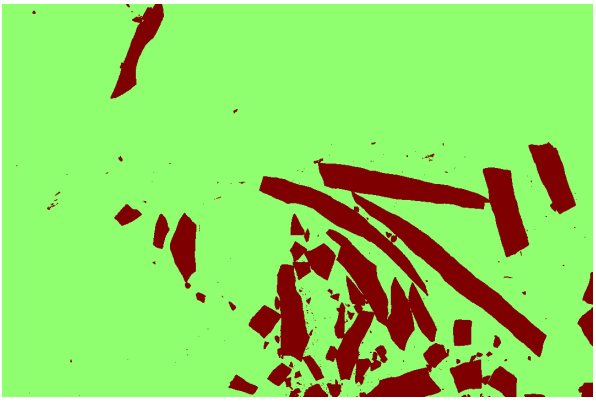

(c) K-means clustering method with 2 clusters, $IC = 15.65\%$.

Figure 2.23: Sea-ice image 1 and ice detection.

(a) Original sea-ice Image 2.

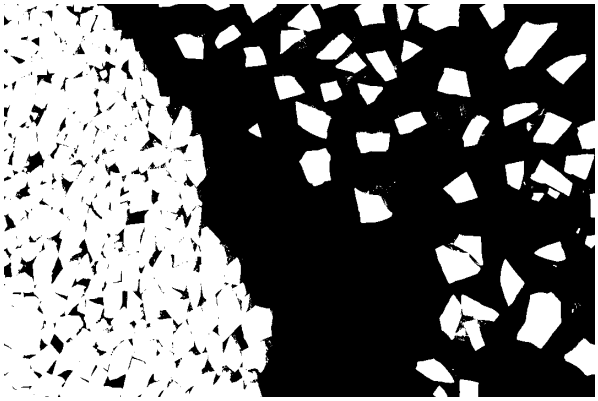

(b) Otsu thresholding method, $IC = 42.19\%$.

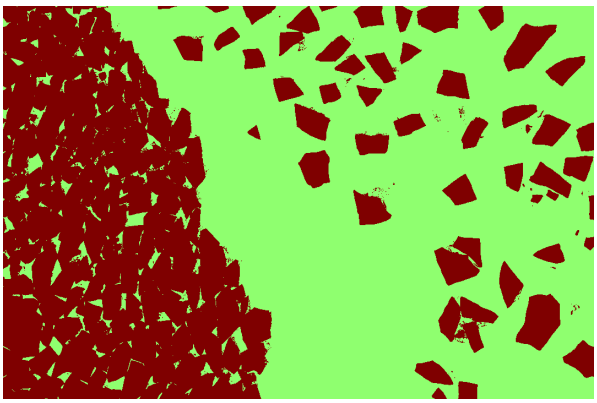

(c) K-means clustering method with 2 clusters, $IC = 42.29\%$.

Figure 2.24: Sea-ice image 2 and ice detection.

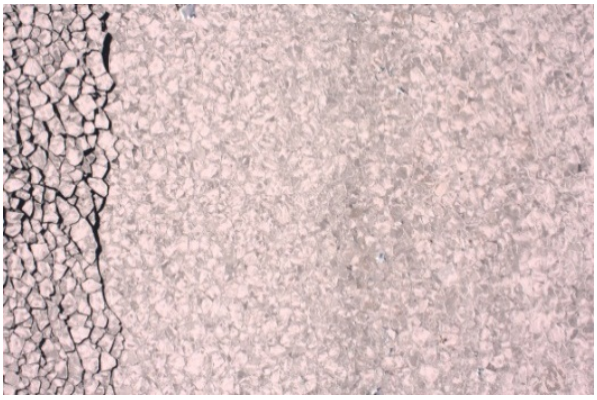

(a) Original sea-ice Image 3.

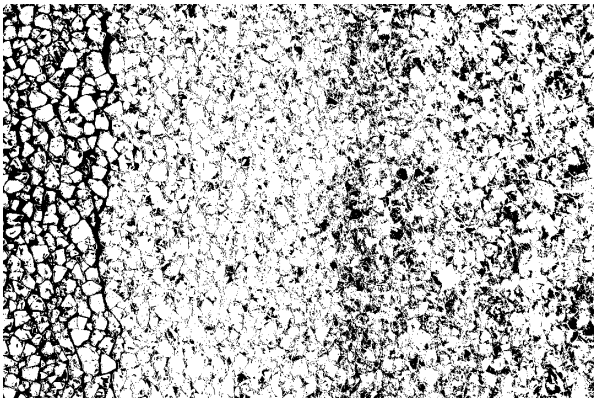

(b) Otsu thresholding method, $IC = 73.73\%$.

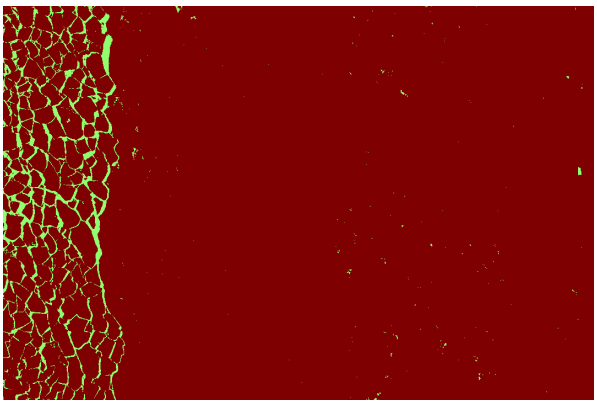

(c) K-means clustering method with 2 clusters, $IC = 96.50\%$.

Figure 2.25: Sea-ice image 3 and ice detection.

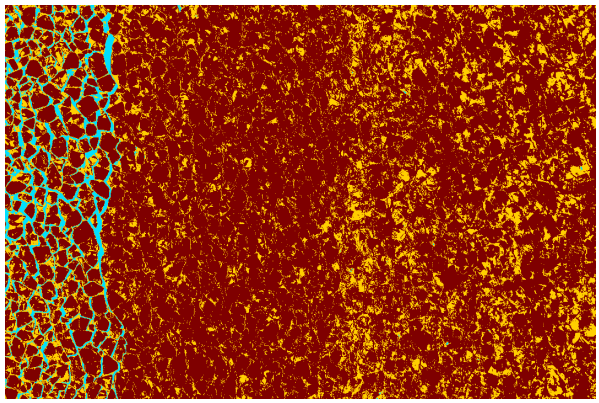

Figure 2.26: Ice identification of Figure 2.25(a) by k-means with 3 clusters. $IC = 97.11\%$, "ice cluster 1" in red: 77.91%, , "ice cluster 2" in yellow: 19.20%, water in blue: 2.89%.

brash ice and slush are parts of the ice cover in the definition of ice concentration, we can then assume that an IC value of approximately $96 - 97\%$ is the more correct number. The k-means clustering method, on the other hand, has a better detection by dividing the image into three or more clusters, as shown in Figure 2.26. Additionally, it is found that the Otsu method is less effective than the k-means methods for the identification of the ice from the water when the image has a high ice concentration with a large amount of brash ice and slush.

Chapter 3

Ice Edge Detection

The ice floe size distribution plays an important role in ice-structure analyses, the dynamic and thermodynamic processes. In image processing, the detection of individual ice floe boundaries is a key tool for extracting information of floe size distribution from ice images. A common approach for detecting object boundaries is to use edge detection. Edge detection can be used in feature detection and feature extraction, object location, and some properties such as area, perimeter, and shape measurements. This means that, with this technique, ice floe boundaries may be obtained to distinguish individual ice floes, and the properties of ice floes together with the floe size distribution can thereby be estimated.

This chapter introduces two common edge detection methods - derivative edge detection and morphology edge detection. These methods are applied to both model-ice and sea-ice images to try to extract ice floe boundaries and distinguish individual floes. The advantages and disadvantage of these two methods are also discussed. The work presented in this chapter was published in [30, 50].

3.1 Derivative Edge Detection

Derivative edge detection is one of the most popular techniques in image processing. Edges characterize object (or surface) boundaries that represent the change from one object (or surface) to another. This gives a rapid change in image brightness between neighboring pixels, which is useful for segmentation, registration, and identification of objects in a scene.

In image processing, we identify the edges by identifying the difference between regions, and this is measured by the gradient vector (first-order derivative) of a digital image with pixel value $f(x, y)$ [59],

$$\bigtriangledown \overrightarrow{f} = \begin{bmatrix} G_x \\ G_y \end{bmatrix} = \begin{bmatrix} \frac{\partial f}{\partial x} \\ \frac{\partial f}{\partial y} \end{bmatrix}, \tag{3.1}$$

The gradient vector has a direction toward the most rapid change in intensity. The magnitude is given by:

$$\bigtriangledown f = \left[G_x^2 + G_y^2\right]^{\frac{1}{2}} = \left[\left(\frac{\partial f}{\partial x}\right)^2 + \left(\frac{\partial f}{\partial y}\right)^2\right]^{\frac{1}{2}}, \tag{3.2}$$

while the direction is given by:

$$\theta = \tan^{-1}\left(\frac{G_x}{G_y}\right). \tag{3.3}$$

The discrete derivative can be approximated by:

$$\frac{\partial f}{\partial x}(x, y) \approx f(x + 1, y) - f(x, y), \tag{3.4a}$$

$$\frac{\partial f}{\partial y}(x, y) \approx f(x, y + 1) - f(x, y). \tag{3.4b}$$

Many discrete differentiation operators are used for computing an approximation of the gradient of the image intensity function, such as Sobel and Prewitt, and Figure 3.1 shows their edge detector masks and the first-order derivatives they implement [59].

Similarly, the second-order derivative (the Laplacian of an image) is defined as:

$$\bigtriangledown^2 f = \frac{\partial^2 f}{\partial x^2} + \frac{\partial^2 f}{\partial y^2}, \tag{3.5}$$

Using the discrete approximations:

$$\frac{\partial^2 f}{\partial x^2}(x, y) \approx f(x + 1, y) + f(x - 1, y) - 2f(x, y), \tag{3.6a}$$

$$\frac{\partial^2 f}{\partial y^2}(x, y) \approx f(x, y + 1) + f(x, y - 1) - 2f(x, y), \tag{3.6b}$$

this gives:

$$\bigtriangledown^2 f(x, y) \approx f(x-1, y)+f(x+1, y)+f(x, y-1)+f(x, y+1)-4f(x, y). \tag{3.7}$$

$f(x-1,y-1)$	$f(x,y-1)$	$f(x+1,y-1)$
$f(x-1,y)$	$f(x,y)$	$f(x+1,y)$
$f(x-1,y+1)$	$f(x,y+1)$	$f(x+1,y+1)$

(a) Image neighborhood.

-1	-2	-1
0	0	0
1	2	1

$$G_x = [f(x-1,y+1) + 2f(x,y+1) + f(x+1,y+1)] - [f(x-1,y-1) + 2f(x,y-1) + f(x+1,y-1)]$$

-1	0	1
-2	0	2
-1	0	1

$$G_y = [f(x+1,y-1) + 2f(x+1,y) + f(x+1,y+1)] - [f(x-1,y-1) + 2f(x-1,y) + f(x-1,y+1)]$$

(b) Sobel edge detector.

-1	-1	-1
0	0	0
1	1	1

$$G_x = [f(x-1,y+1) + f(x,y+1) + f(x+1,y+1)] - [f(x-1,y-1) + f(x,y-1) + f(x+1,y-1)]$$

-1	0	1
-1	0	1
-1	0	1

$$G_y = [f(x+1,y-1) + f(x+1,y) + f(x+1,y+1)] - [f(x-1,y-1) + f(x-1,y) + f(x-1,y+1)]$$

(c) Prewitt edge detector.

Figure 3.1: Examples of the edge detector masks and the first-order derivatives they implement.

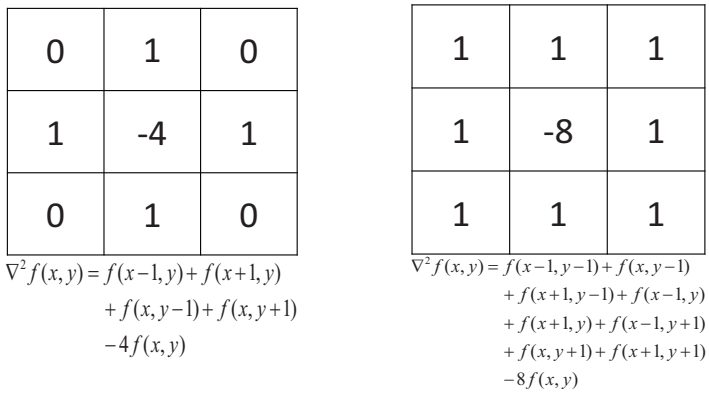

(a) 4-neighbor. (b) 8-neighbor.

Figure 3.2: Examples of the edge detector masks and the second-order derivatives they implement.

For a rapid change, the first-order derivative has a large magnitude and the second-order derivative crosses zero, which are the two criteria that can be used to identify which pixels in an image may belong to an edge. However, the second-order derivative is seldom used by itself for edge detection because it is sensitive to noise, unable to detect edge direction, and produces double edges [63]. A common method to detect edges is by estimating the gradient of the image at every point to generate a "gradient" image, and then thresholding the gradient image.

3.2 Morphology Edge Detection

Morphology refers to geometrical characteristics related to the form and structure of objects, such as size, shape, and orientation. In image processing, mathematical morphology is used to extract image components based on shapes that are useful in representation and description of region shapes, such as boundaries, skeletons, and the convex hull [63].

Morphological operations create an output image of the same size as the input image by applying a structuring element, such as disk, rectangle, ring, etc. The structuring element is a shape that is used to probe an input image and draw conclusions on how the structuring element fits or misses the shapes in the input image. In a morphological operation, the value of each pixel in the output image is based on a comparison of the corresponding pixel in the input image with its neighbors, i.e., the structuring element is translated to each

pixel's position, and the points within the translated structuring element are compared with the pixels of the input image. By choosing the size and shape of the neighborhood, it is possible to construct a morphological operation that is sensitive to specific shapes in the input image.

3.2.1 Erosion and dilation

The number of pixels added or removed from the objects in an image depends on the size and shape of the structuring element used to process the image. The state of any given pixel in the output image is determined by applying the rule to the corresponding pixel and its neighbors in the input image. The operations of erosion and dilation are fundamental to morphological image processing.

An erosion operation "shrinks" or "thins" objects by removing pixels on object boundaries. The value of the output pixel is the minimum value of all the pixels in the input pixel's neighborhood for the erosion operator. If A is a binary image (1-valued pixels indicate object, while 0-valued pixels indicate background), B is a chosen structuring element, according to [63], the erosion of A by B, denoted by $A \ominus B$, is the set of all structuring element origin locations where the translated B has no overlap with the background of A. The mathematical definition of erosion is defined as follow [63]:

$$A \ominus B = \{z|(B)_z \cap A^c \neq \varnothing\} \tag{3.8}$$

where $(B)_z$ is the translation of B by the point $z = (z_1, z_2)$, defined as

$$(B)_z = \{b + z|b \in B\}, \tag{3.9}$$

and A^c is the complement of A (0-valued pixels set to 1-valued and 1-valued pixels set to 0-valued, for a binary image) defined as

$$A^c = \{w|w \notin A\}. \tag{3.10}$$

The structuring element translates the origin throughout the domain of the image and checks to see where it fits entirely within the foreground of the image. The output image has a value of 1 at each location of the origin of the structuring element, such that the element overlaps only 1-valued pixels of the input image (i.e., it does not overlap any of the image background) [63]. The process of erosion is shown in Figure 3.3.

A dilation operation "grows" or "thickens" objects by adding pixels to the objects boundaries. The value of the output pixel is the maximum value of all the pixels in the input pixel's neighborhood for the dilation operator. The

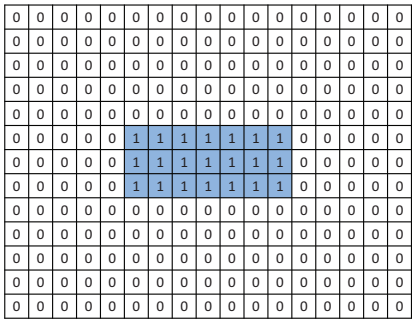

(a) Binary image with rectangular object.

(b) Structuring element with three pixels arranged in a vertical line. The origin of the structuring element is shown in red.

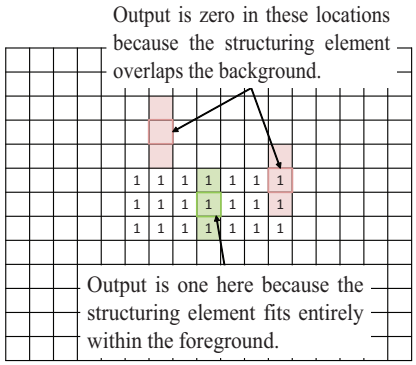

(c) Structuring element translated to several locations on the image.

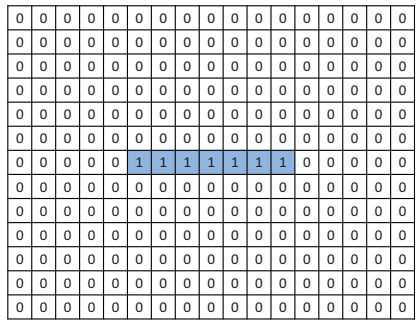

(d) Output image matrix.

Figure 3.3: The process of erosion. Courtesy: [63].

dilation of A by B, denoted by $A \oplus B$, is the set consisting of all the structuring element origin locations where the reflected and translated B overlaps at least some portion of A [63]. The mathematical definition of dilation is defined as follows [63]:

$$A \oplus B = \{z|(\widehat{B})_z \cap A \neq \varnothing\} \tag{3.11}$$

where $\widehat{B}$ is the reflection of B, defined as

$$\widehat{B} = \{w| - w \in B\}. \tag{3.12}$$

The structuring element translates the origin throughout the domain of the image and checks to see where it overlaps with 1-valued pixels. The output image is 1 at each location of the origin, such that the structuring element overlaps at least one 1-valued pixel in the input image [63]. The process of dilation is shown in Figure 3.4.

3.2.2 Morphological gradient

Morphological gradients are based on the difference between extensive and anti-extensive transformations [64]. Erosion and dilation can be used to extract edge information from images.

The Beucher gradient (the basic morphological gradient), defined as the difference between the dilated and the eroded of the image A with the structuring element B, is given by:

$$\rho = (A \oplus B) - (A \ominus B), \tag{3.13}$$

Similarly, the internal gradient, defined as the difference between the original image and the eroded image, is given by:

$$\rho_{int} = A - (A \ominus B), \tag{3.14}$$

and the external gradient, defined as the difference between the dilated image and the original image, is given by:

$$\rho_{ext} = (A \oplus B) - A. \tag{3.15}$$

From Equation 3.13 - 3.15, we obtained:

$$\rho_{int} + \rho_{ext} = \rho. \tag{3.16}$$

The internal and external gradients are “half gradients” and "thinner" than the Beucher gradient. The internal gradient generates internal edges of the object,

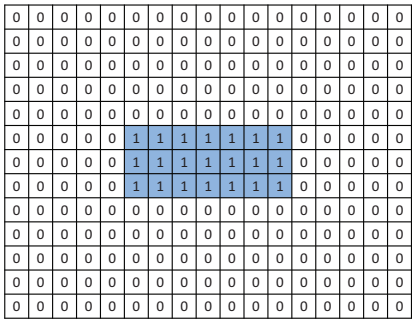

(a) Binary image with rectangular object.

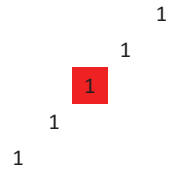

(b) Structuring element with five pixels arranged in a diagonal line. The origin of the structuring element is shown in red.

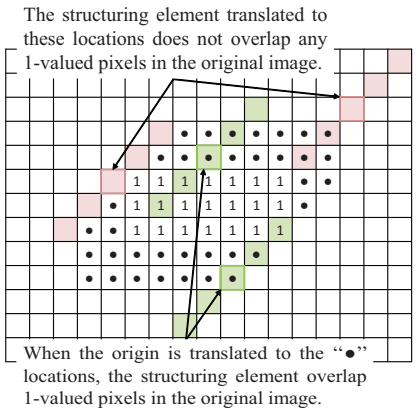

(c) Structuring element translated to several locations on the image.

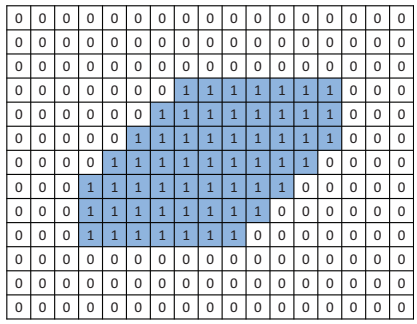

(d) Output image matrix.

Figure 3.4: The process of dilation. Courtesy: [63].

and the external gradient generates external edges, while the Beucher gradient generates both internal and external edges. The internal and external gradients are used when thin contours are needed. The choice between internal or external gradient depends on the nature of the objects to be extracted [64].

3.3 Experimental Results and Discussion

The derivative and morphology edge detection methods are applied to extract the boundaries of both model- and sea-ice floes. Parts of results are shown in Figure 3.5 - 3.7.

(a) Overall model-ice tank image for run no. 5200.

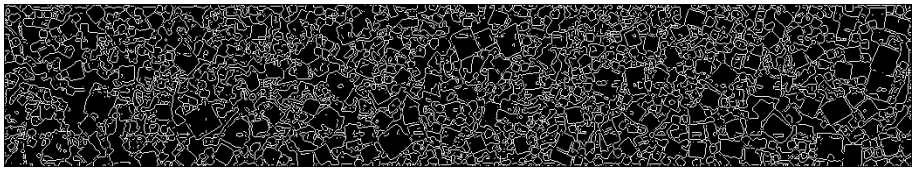

(b) Edge detection of (a) - Derivative method (Sobel edge detector, threshold = 0.02).

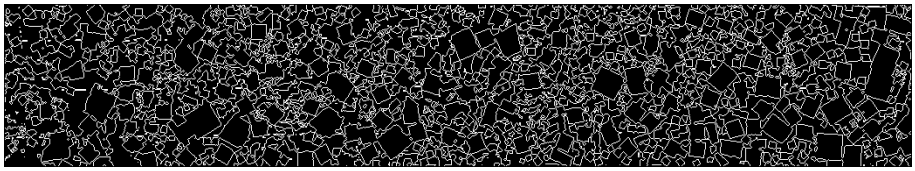

(c) Edge detection of (a) - Morphology method (the internal gradient using a disk structural element with 1-pixel radius).

Figure 3.5: Edge detections of overall tank image for run no. 5200.

Both derivative and morphology methods can extract the floe boundaries correctly when ice floes are far away from others, as seen the sea-ice floes on the right part in Figure 3.7. However, when the ice floes are close or connecting to each other, as seen in the model-ice floes in Figure 3.5, Figure 3.6, and sea-ice floes on the left part in Figure 3.7, neither methods can completely find the edges between those floes. Thus, those floes will be miskatenly considered as one big floe, and this will affect later size distribution and ice force estimations.

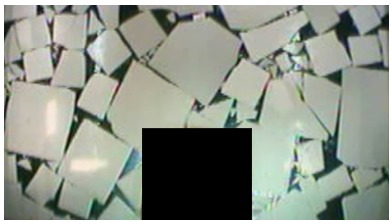

(a) Run no. 5100: Time=816s.

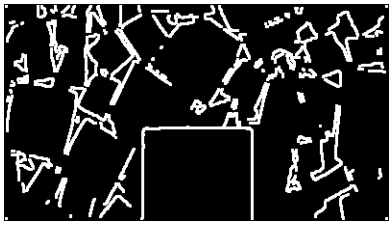

(b) Edge detection of (a) - Derivative method (Sobel edge detector, threshold $= 0.05$).

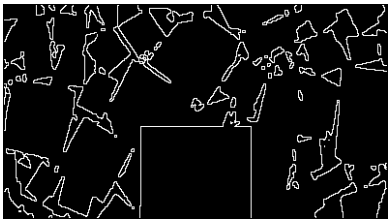

(c) Edge detection of (a) - Morphology method (the internal gradient using a disk structural element with 1-pixel radius).

Figure 3.6: Edge detections of frames for run no. 5100 at 816s.

Because the derivative method is to identify the rapid intensity changes in the image, more weak edge pixels between the connected floes can be detected by the derivative method, as seen in Figure 3.5. However, the derivative method is more sensitive to the noise than the morphology method. As shown in Figure 3.8, when decreasing the threshold for the derivative gradient, the derivative method can find more edges, but at the cost of more noise. Moreover, the derivative method also produces more non-closed boundaries (especially the detected weak boundaries between connected floes). Such non-closed boundaries indicate the loss of boundary information, and cannot separate the connected floes.

Since the morphology method is to identify the difference between extension and anti-extension of region's shape, a good description of the object's shape is given by this method. The morphology method is better in closing the boundaries than the derivative method. Moreover, since the erosion operation is to shrink objects, the thin connections between floes can be broken when using internal or Beucher gradient with a proper structuring element, and the weakly connected ice floes are thereby separated.

Figure 3.9 shows an example of the weakly connected sea-ice floes separation by the morphology method using the internal gradient. As shown in Figure 3.9(b), the detected boundaries are thin, and the connected ice floes cannot be separated when using a 5-pixel-radius disk-structuring element. When

(a) Sea-ice image.

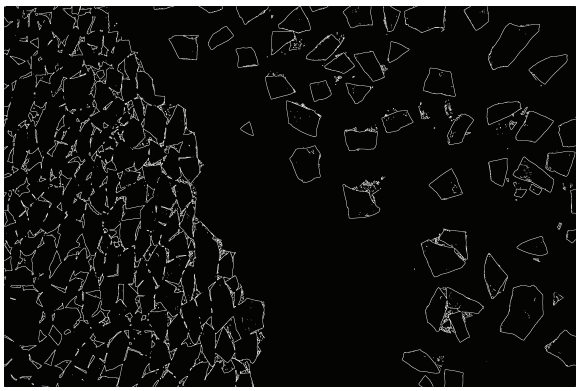

(b) Edge detection of (a) - Derivative (Sobel edge detector, threshold $= 0.05$).

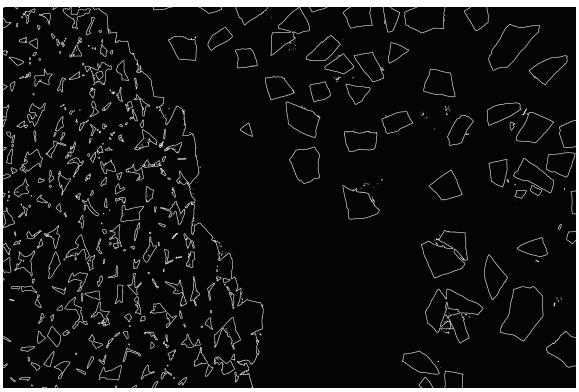

(c) Edge detection of (a) - Morphology method (the internal gradient using a disk structural element with 5-pixel radius).

Figure 3.7: Edge detections of sea-ice image.

(a) A sample of connected model-ice floes from Figure 3.5(a).

(b) Edge detection of (a) by the morphology method. The detected boundaries are closed, but the weak edges between the connected floes are lost.

(c) Edge detection of (a) by the derivative using Sobel edge detector with the threshold of 0.02. Part of the weak edges (non-closed) between the connected floes are found.

(d) Edge detection of (a) by the derivative using Sobel edge detector with the threshold of 0.01. More weak edges (non-closed) between the connected floes are found at the cost of more noise.

Figure 3.8: Comparison of the derivative and the morphology methods.

enlarging the structuring element to a 16-pixel-radius disk, the detected floe boundaries become thick enough to break the connections between the floes and separate the connected floes. However, because of the various sizes and shapes of the ice floes (especially sea-ice floes), it is difficult to find a proper structuring element for an ice image. Furthermore, the size of ice floe will decease when the detected floe boundaries become thicker. Therefore, this method only works when separating the weakly connected ice floes, and will fail in the separation of the strongly connected ice floes, such as the connected model-ice floes in Figure 3.8(a).

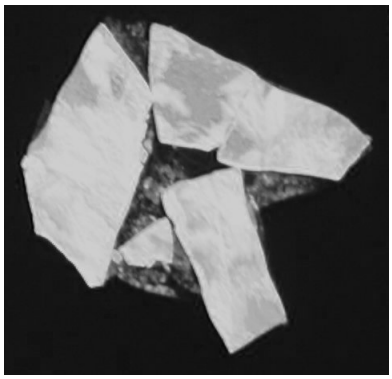

(a) A sample of connected sea-ice floes from Figure 3.7(a).

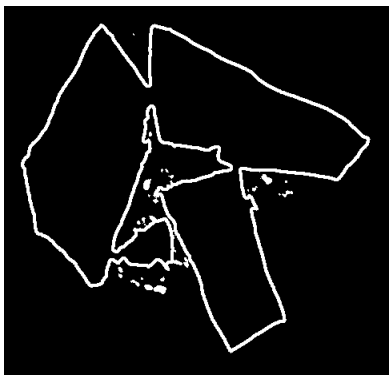

(b) Edge detection of (a) by the morphology method using the internal gradient with a 5-pixel-radius disk-structuring element. The detected floe boundaries are thin, and ice floes are connected.

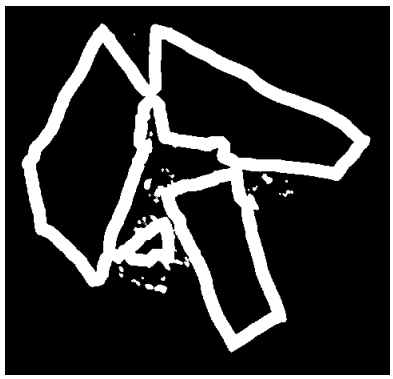

(c) Edge detection of (a) by the morphology method using the internal gradient with a 16-pixel-radius disk-structuring element. The detected floe boundaries become thicker, and the weakly connected ice floes are separated.

Figure 3.9: Weakly connected ice floes separation.

Our experimental results show that, individual ice floes cannot be distinguished well by neither derivative nor morphology methods when the floes are too close to each other with possible touching. The inaccuracy of the ice floe boundary detection will result in missing boundary information or non-closed boundaries, and these failures will affect the statistical ice floe size distribution result. Therefore, in order to derive the precise ice floe size distribution, the development of an effective algorithm for ice floe boundary detection, especially the connected floes separation, is a main topic in this thesis, and this will be addressed in the following chapters.

Chapter 4

Watershed-based Connected Ice Floe Segmentation

In the actual sea-ice covered environment, ice floes typically touch each other and possibly overlap, and the junctions are usually difficult to detect in the digital images. A remedy to this problem is to use the watershed transform to separate the connected ice floes.

The watershed transform and its improvements have been widely used to separate connected objects with acceptable results in several research areas, such as grain [65] and cell nuclei images [66]. [67] also adopted the watershed transform to separate the connected sea-ice floes into individual floes. They removed brash ice by using image opening and erosion operators literally and then used the watershed transform to segment the connected ice floes. However, over- and under-segmentation of the ice floes are the major issues in watershed-based segmentation. Due to an ineluctable over-segmentation problem, [67] manually removed these over-segmented lines. To remove the over-segmentation automatically, the combination of concave detection and neighboring-region merging is proposed in this chapter. The work presented in this chapter was published in [54].

4.1 Watershed transform

The watershed transform is a morphological-based algorithm used to segment images. The pixel values are interpreted as heights, and a grayscale image is considered as a topological surface. Water falling on this topological surface flows toward the "nearest" minimum, which lies at the end of the path of

steepest descent and would collect in the areas called catchment basins. Additionally, water falling exactly on the called watershed ridge line would be equally likely to collect in either of the two catchment basins [59]. Figure 4.1 shows the topological surface of a complemented grayscale ice image.

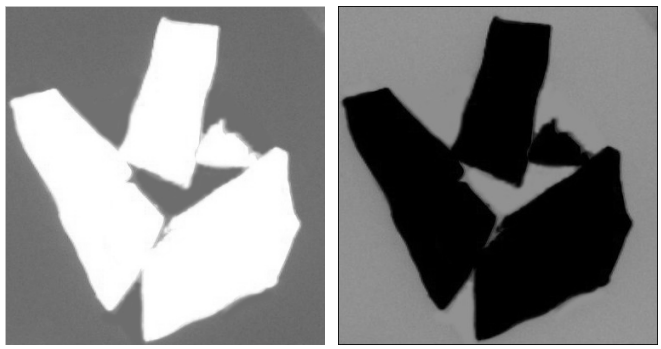

(a) Gray scale image. (b) Complement of (a).

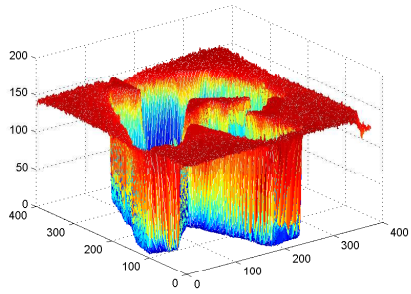

(c) Topological surface of (a).

Figure 4.1: The topological surface of a complemented grayscale ice image.

The watershed-based segmentation could be used to solve a connected objects division problem. The watershed will first check the local minima in the image and then perform the transformation based on these. The number of segmented regions depends on local minima in the image. Usually, there is more than one minimum for each object, and this will induce over-segmentation (e.g., see Figure 4.2). Over-segmentation is a major problem of this watershed. Refinements, such as minima-combination [68], mark-controlled [59] [69], and H-dome transform [70] were adopted to improve the over-segmentation. However, due to varieties of sea-ice floe shapes and sizes, it is hard to automatically locate the correct local minima or markers for each ice floe. In this chapter, all the ice floes in the image are first identified by the Otsu threshold or k-means clustering algorithm [30, 50], and the grayscale image is converted into

a binary image. Then, the seed points for the individual ice floes are located, and the watershed algorithm is carried out to segment the image. Finally a neighboring-region merging method is proposed to reduce over-segmentation after the watershed-based sea-ice image segmentation.

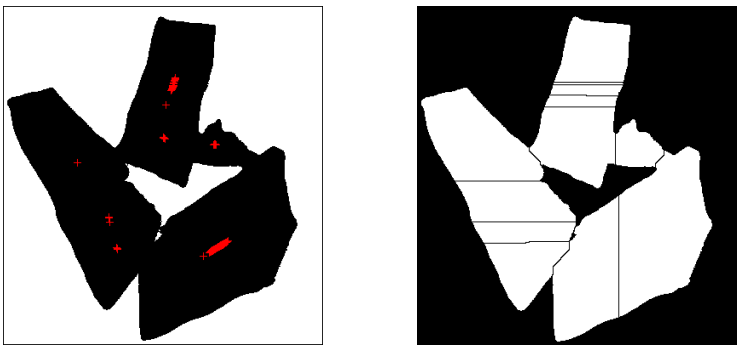

(a) Local minima superimposed in binary image.

(b) Over-segmented image.

Figure 4.2: Watershed-based segmentation.

4.2 Neighboring-region Merging

In this method, it is assumed that each ice floe has a convex boundary and that the junction line between two connected ice floes has at least one concave ending point. Based on this assumption, the junction lines obtained from the watershed-based segmentation are filtered by deleting those that have two convex ending points.

Figure 4.3 shows a flow chart of the watershed-based segmentation and the neighboring-region merging algorithm.

The differential chain code method [71] is applied to check the concavity of the two ending points of a proposed junction line between two connected ice floes, where the junction lines and the corresponding ice floes are obtained from the watershed-based segmentation.

4.3 Concave detection by chain code

Chain codes are used to represent a boundary by a connected sequence of straight-line segments of specified length and direction [72]. Typically, this

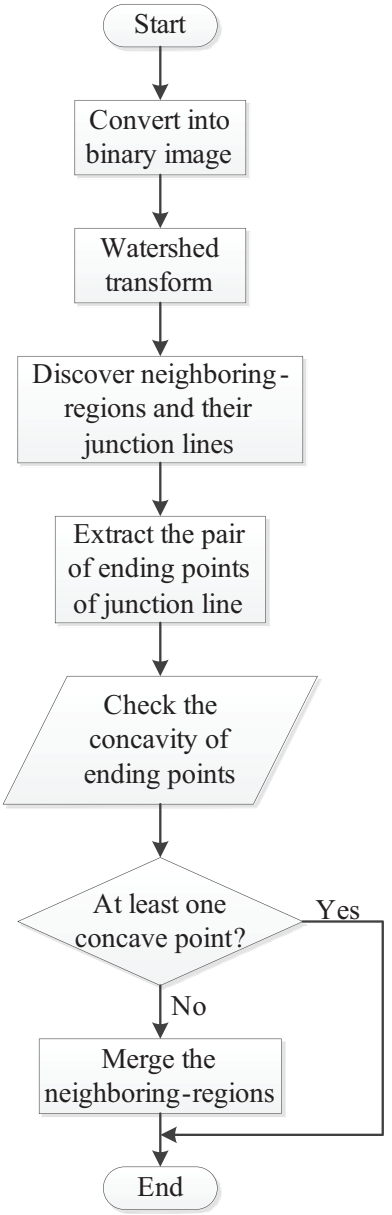

Figure 4.3: Flow chart of the watershed-based segmentation and neighboring-region merging.

representation is based on 4 or 8-connectivity of the segments. The direction of each segment is coded by using a numbering scheme, as shown in Figure 4.4. The chain code of a boundary depends on the stating point. However, it can be normalized with respect to the starting point by treating it as a circular sequence of direction numbers and redefining the starting point so that the resulting sequence of numbers forms an integer of minimum magnitude.

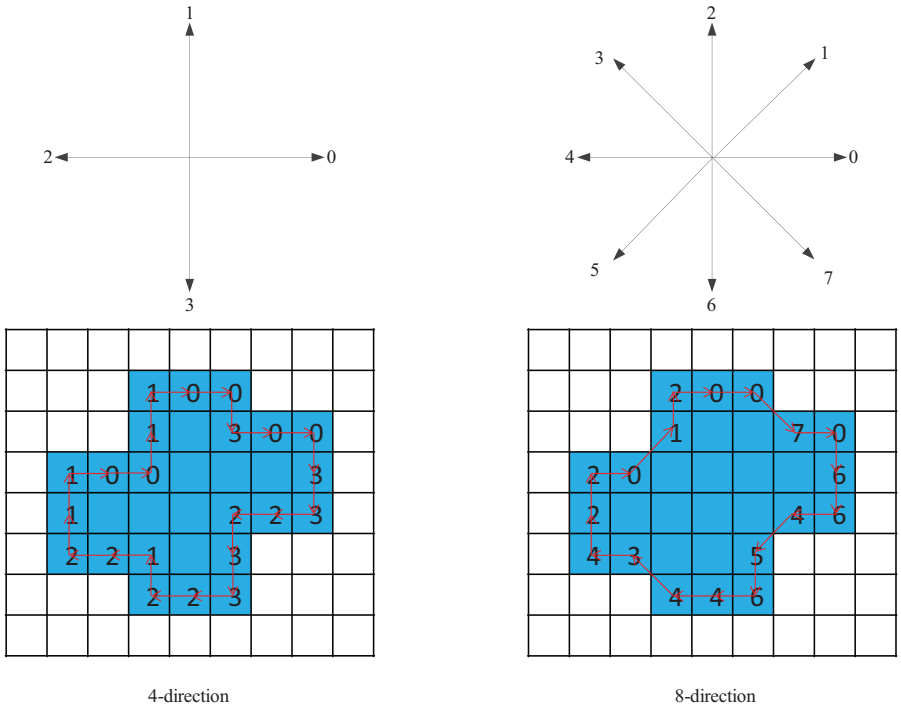

Figure 4.4: Numbering scheme of the chain code.

The first difference of the chain code reflects the spatial relationships between boundary segments, which are independent of rotation. This is obtained by counting the number of direction changes that separate two adjacent elements of the code. If the difference is less than 0, the difference should be modulo 8. Figure 4.5 gives an example of a boundary's chain code and its first difference.

Changes in the code direction indicate a corner on the boundary. By analyzing the direction changes as we travel in a clockwise direction along the boundary, we can determine and mark the convex and concave corners. However, the chain code has a low accuracy since it only represents 8 directions. Therefore, we use absolute chain code sum [71] to increase the accuracy.

Figure 4.5: A boundary's chain code and its first difference.

Assume $C(i)$ and $C(i-1)$ is the chain code of current $Node\ i$ and former $Node\ i-1$, $R(i)$ is the relative chain code, given by:

$$R(i) = [C(i) - C(i-1) + 8]\ MOD\ 8, \tag{4.1}$$

$$\text{IF } (R(i) > 4) \text{ THEN } R(i) = R(i) - 8. \tag{4.2}$$

The relative chain code indicates that $Node\ i$ has rotated $R(i) \times 45°$ counter-clockwise (the negative value indicates the clockwise direction) to $Node\ i-1$.

The absolute chain code $A(i)$ is the sum of relative chain code from the starting node to $Node\ i$, and the absolute chain code of the starting node is 0, therefore,

$$A(0) = 0, \tag{4.3}$$

$$A(i) = A(i-1) + R(i). \tag{4.4}$$

When the total number of boundary nodes is N with the notation from 0 to $N-1$, clockwise, it should be noted that the ending node is denoted as N, which is actually the starting node 0, and the difference of absolute chain codes between the starting node and the ending node is 8, that is,

$$A(0) - A(N) = 8. \tag{4.5}$$

The absolute chain code sum of three sequential nodes is

$$S(i) = A(i) + A(i-1) + A(i-2), \tag{4.6}$$

When calculating the starting two nodes, the former absolute chain code should be shifted to the ends of the sequence and adjusted accordingly since the

boundary is closed, that is,

$$S(0) = A(0) + A(N-1) + A(N-2) + 16, \tag{4.7}$$

$$S(1) = A(1) + A(0) + A(N-1) + 8. \tag{4.8}$$

Similar to Equation 4.5, we have

$$S(0) - S(N) = 24. \tag{4.9}$$

The absolute chain code sum has 24 directions, which is more accurate than the original 8-direction chain code, and can be used to represent the tangent direction (slope) of the edge points instead.

Then, the differential chain code, which is the difference of the absolute chain code sum, is given by:

$$D(i) = S(i+3) - S(i), \tag{4.10}$$

Similarly, when calculating the last 3 nodes, the latter absolute chain code sum should start at the starting nodes and be adjusted accordingly, that is,

$$D(N-j) = S(N-j+3) - S(N-j) \tag{4.11}$$

$$= S(3-j) - 24 - S(N-j). \tag{4.12}$$

where $j = 1, 2, 3$.

The differential chain code is proportional to the curvature of the edges, and defines the change of direction between two neighboring boundary segments:

$$\theta = D(i) \times 15^{\circ}. \tag{4.13}$$

Therefore, Node i is identified as a concave point if the differential chain code, $D(i)$, is positive when tracing clockwise along the boundary. Considering the rough of the boundary, the nodes with the differential chain code between 3 and 10 are detected as concave points in this research, that is,

$$Node\ i \text{ is a concave point if } 3 \leq D(i) \leq 10. \tag{4.14}$$

The detection result is shown in Figure 4.6.

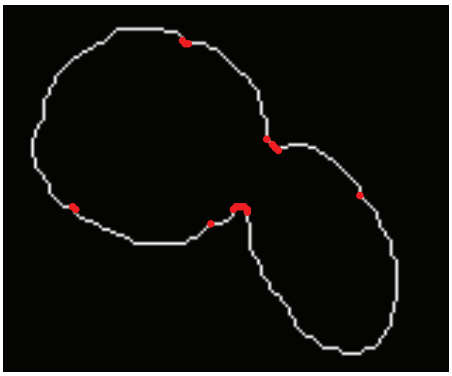

Figure 4.6: Concave detection by chain code. The detected concave points are denoted by red dots.

4.4 Experimental Results and Discussion

Image segmentation by using the watershed transform is powerful for connected object segmentation. However, there is a problem with over- and under-segmentation with this transform that must be overcome. As mentioned in [59], the over-segmentation problem can be serious enough to render the segmented result useless. Therefore, a neighboring-region merging algorithm is applied in this chapter to improve the ice image segmentation.

A few sea-ice images obtained from a remote sensing mission of ice conditions carried out at Ny-Ålesund in early May 2011 [30] are applied in a case study. It should be noted that the brash ice has been removed manually from the images before segmentation. Some examples of the experimental results are then shown in Figure 4.7. Based on the segmented ice image, the floe size can be calculated by the number of pixels within each ice floe. Figure 4.8 shows an example of the segmented ice image and the calculated floe size distribution (grouped by pixel numbers that can be scaled to real size).

As seen from Figure 4.7, most of the over-segmented lines have been removed, but some lines still exist. This is because the applied neighboring-region merging algorithm is based on a very simple assumption, namely that the watershed-segmented line is taken as a correct junction line if it has one or two concave ending points, an assumption that is not always correct since a real ice floe is typically not a perfect convex shape. As shown in Figure 4.9(b), the segmented line highlighted by red has a concave ending point, which is just a concave corner of the floe boundary, but it is not a real junction concave corner between two floes. Even if one or both of its ending points are real junction concave corners, the segmented line obtained by using the watershed transform is still

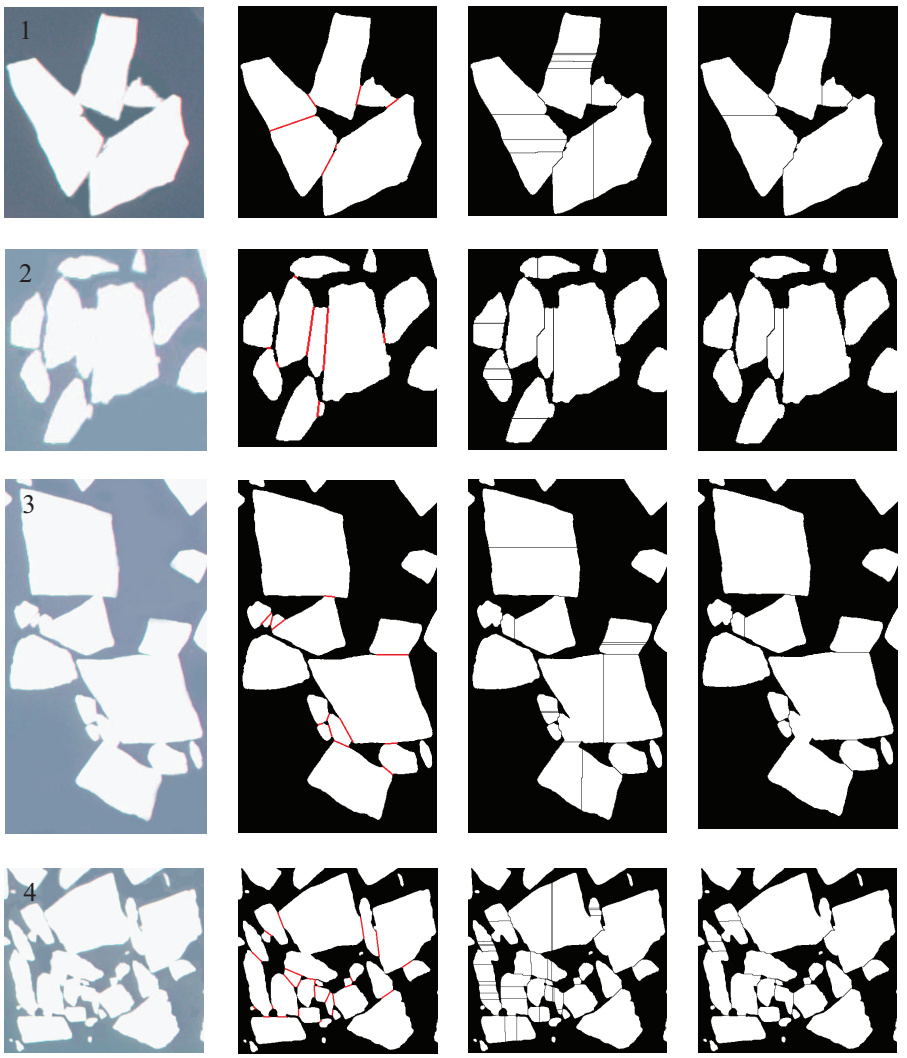

Figure 4.7: Watershed-based connected ice floe segmentation: (a) Original ice images. (b) Binary images with manually identified segmented lines between connected ice floes. (c) Segmented images based on the watershed transform. (d) Segmented images after neighboring-region merging.

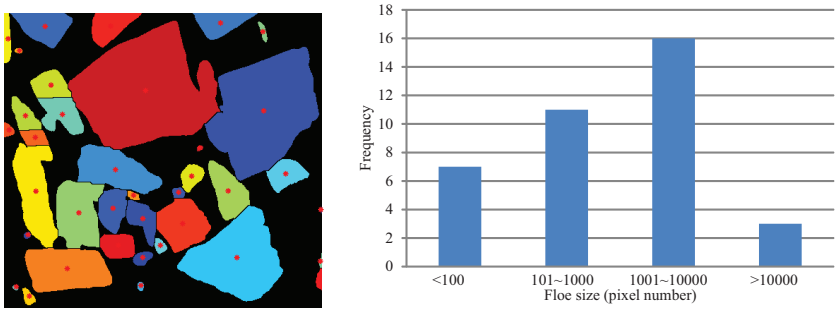

(a) Segmented image with floe center superimposed.

(b) Calculated floe size distribution.

Figure 4.8: Segmented floes and floe size distribution.

probably not a correct junction line (e.g., see the segmented line highlighted by green in Figure 4.9(b)).

(a) Manually identified segmentation.

(b) Segmentation by the established algorithm.

Figure 4.9: Examples of over- and under-segmentation.

Under-segmentation is another problem of the watershed-based segmentation, and this cannot be improved by the neighboring-region merging algorithm. As shown in Figure 4.9(a), there should be a segmented line in the region highlighted by yellow, but it is not detected by the watershed transform.

Table 4.1 lists the number of over- and under-segmented lines when compared to segmentation by manual inspection in Figure 4.7. It is found that the over-segmented lines are significantly reduced by the neighboring-region merging algorithm, while the under-segmentation is still a problem. Note, however, that when we apply the estimated floe size distribution in ice-structure interaction analysis, the under-segmentation of ice floes will typically lead to an

overestimation of ice forces, meaning a conservative estimate.

Table 4.1: Number of over- and under-segmented lines compared with manual inspection.

Image	Manual inspection	Watershed-based segmentation			Watershed-based segmentation and neighboring region merging		
	No. of floes	No. of floes	Over segment	Under segment	No. of floes	Over segment	Under segment
1	5	12	7	0	5	0	0
2	12	16	5	1	11	0	1
3	20	25	7	2	17	0	3
4	38	60	26	5	37	4	6

Besides the over- and under-segmentation problems, ambiguously segmented lines are another problem. Figure 4.10 shows an example of this problem. By looking at Figure 4.10(b) it is difficult to say whether the segmented line highlighted exists. Figure 4.10(c) shows the original image of the same sea-ice floes taken under a different reflection condition, featuring the same ice floes with more details. By looking at this image it seems as if there is a boundary in the highlighted region, but it is still difficult to identify the exact location of this segmented line. Therefore, high-resolution images would definitely provide a more accurate ice floe segmentation.

It also should be noted that the real boundary information between the connected floes are actually lost when using watershed transform. This occurs because the watershed transform operates on binary images and focuses on the morphological characteristics of ice floes. Therefore, the watershed-based method is limited by crowded ice floe images in which the ice floes in the mass are connected to each other and no “hole” or concave regions could be found after binarization. Therefore, this method should only be applicable to the ice floe images with invisible the floe junctions (such as the binary ice images).

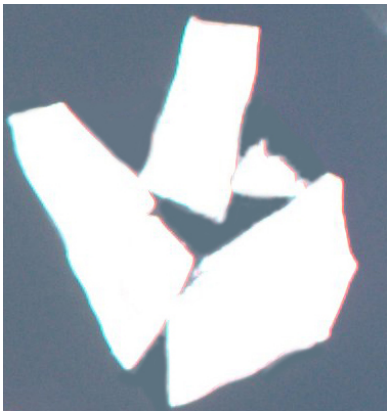

(a) Original ice image.

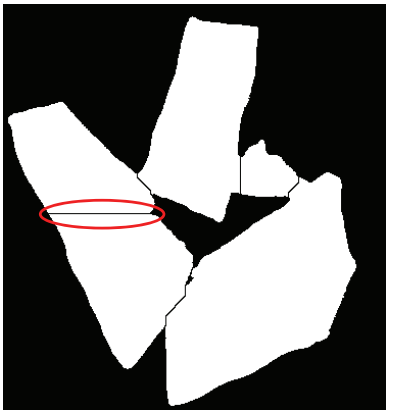

(b) Segmentation by the established algorithm.

(c) Original ice image with more details.

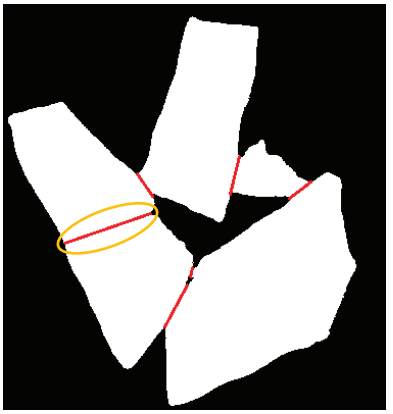

(d) Manually identified segmentation.

Figure 4.10: An example of the ambiguously segmented lines.

Chapter 5

Ice Image Segmentation and Ice Floe Identification

The size, shape, and location of the ice floes give important clues to their physical structures. Automatic identification of individual floe boundaries is crucial in obtaining such information of ice floes from ice images. Chapter 3 applied and compared derivative and morphology boundary detection algorithms in both model-ice and sea-ice images [30, 50]. Derivative edge detection is sensitive to weak boundaries and noise, and it often produces non-closed boundaries, meaning that junctions between ice floes may be difficult to identify when the floes are seemingly connected in the ice images. In contrast, morphology boundary detection results in a good description of the object shape, generates closed boundaries, and could separate weakly connected ice floes. However, some boundary information is still lost and strongly connected ice floes cannot be separated.

Traditional boundary detection algorithms cannot easily detect the boundary between connected floes. This issue challenges the boundary detection of individual ice floes and significantly affects ice floe size analysis. Therefore, the boundary hidden by an apparent connection between ice floes should be identified.

To mitigate this issue, [73, 74] separated closely distributed ice floes by setting a threshold higher than the ice-water segmentation threshold. However, this threshold did not work well when the ice floes were connected. Consequently, they manually separated the connected ice floes. [67] and Chapter 4 adopted the watershed transform to segment sea-ice images. Due to an ineluctable over-segmentation problem, [67] manually removed these over-segmented lines. In Chapter 4, we assumed that each ice floe had a convex

boundary and that the junction line between two connected ice floes had at least one concave ending point. After the watershed transform, the convexity of each pair of ending points was checked, and two neighboring floes whose junction line ending points were both convex were merged to automatically remove the over-segmentation [54].

The authors of [75] and [76] introduced a mathematical morphology together with principal curve clustering to identify ice floes and their boundaries in a near fully automated manner. First, the image is binarized using the thresholding method. The erosion-propagation algorithm (EP) is then used to provide a preliminary clustering of the boundary pixels and to produce a collection of objects as floe candidates. To remove subdivisions caused by the EP algorithm, they developed a method based on an algorithm for clustering about closed principal curves to determine which floes should be merged. However, both methods in Chapter 4 and [76] operated on the binary images, their methods focusing on the morphological characteristics of ice floes rather than on the real boundaries, and they were limited by crowded ice floe images where the mass of ice floes were connected to each other and no "hole" or concave regions could be found after binarization.

In this chapter, a gradient vector flow (GVF) snake algorithm is adopted to separate seemingly connected floes into individual ones. To avoid user interaction and to reduce the time required to run the GVF snake algorithm, an automatic contour initialization is proposed based on the distance transform. After that, an ice shape enhancement algorithm is proposed to enhance ice floe shapes and accomplish the identification of individual ice floes. Once the floe boundaries have been obtained, individual ice floes are identified, and the floe size distribution can be calculated from the resulting data. The work presented in this chapter was published in [55, 56, 57].

5.1 Snake Models

Snakes, or active contours defined as an energy-minimizing spline [77], correspond to a powerful method used to locate object boundaries. The initial curves can move under the influence of internal forces from the curve itself and under the influence of external forces computed from the image data. The algorithm stops when the internal and external forces reach equilibrium. The internal and external forces are defined such that the snake will conform to an object boundary or other desired features within an image. There are two types of active contour models: parametric active contours and geometric active contours. This study considered the parametric active contour model due

to its superior detection capability of "weak"-boundaries.

5.1.1 Parametric Snake Model

A typical snake is a curve $\mathbf{C}(s) = (x(s), y(s))$ with the normalized arc length $s \in [0, 1]$. It moves through the spatial domain of an image to minimize the sum of the internal and external energy, given by:

$$\mathbf{E} = \int_0^1 (\mathbf{E}_{int}(\mathbf{C}(s)) + \mathbf{E}_{ext}(\mathbf{C}(s)))\mathrm{d}s, \tag{5.1}$$

where $\mathbf{E}_{int}$ is the internal energy

$$\mathbf{E}_{int} = \frac{1}{2}(\alpha|\mathbf{C}^{'}(s)|^2 + \beta|\mathbf{C}^{''}(s)|^2), \tag{5.2}$$

where α and β are weight parameters that control the snake's tension and rigidity, respectively. $\mathbf{C}^{'}(s)$ denotes the first derivatives of $\mathbf{C}(s)$ with respect to s, making the snake act as a membrane, and $\mathbf{C}^{''}(s)$ denotes the second derivatives, making the snake act as a thin plate.

$\mathbf{E}_{ext}$ is the external energy defined in the image domain. It attracts snakes to salient features in the image, such as boundaries. To find boundaries in a grayscale image, $\mathbf{I}(x, y)$, the image gradient is typically chosen as the external energy [77]:

$$\mathbf{E}_{ext} = -|\nabla \mathbf{I}(x, y)|^2, \tag{5.3}$$

where $\nabla \mathbf{I}(x, y) = \left(\frac{\partial \mathbf{I}}{\partial x}, \frac{\partial \mathbf{I}}{\partial y}\right)$ is the image gradient that represents a directional change in the brightness of the image with the gradient angle $\theta = \arctan\left(\frac{\partial \mathbf{I}}{\partial y} / \frac{\partial \mathbf{I}}{\partial x}\right)$. When also considering the image noise, the external energy is defined as [77]

$$\mathbf{E}_{ext} = -|\nabla \mathbf{G}_\sigma(x, y) * \mathbf{I}(x, y)|^2, \tag{5.4}$$

where $\nabla \mathbf{G}_\sigma(x, y)$ is a two-dimensional Gaussian function with a standard deviation σ and '$*$' denotes convolution.

To minimize the energy $\mathbf{E}$, a snake must satisfy the Euler equation

$$\alpha\mathbf{C}^{''}(s) - \beta\mathbf{C}^{''''}(s) - \nabla\mathbf{E}_{ext} = 0. \tag{5.5}$$

Let $\mathbf{F}_{int} = \alpha\mathbf{C}^{''}(s) - \beta\mathbf{C}^{''''}(s)$ denote the internal force and $\mathbf{F}_{ext} = -\nabla\mathbf{E}_{ext}$ denote the external force. Then Equation 5.5 can be written as the force balance

$$\mathbf{F}_{int} + \mathbf{F}_{ext} = 0. \tag{5.6}$$

The internal force $\mathbf{F}_{int}$ discourages stretching and bending, while the external potential force $\mathbf{F}_{ext}$ pulls the snake toward the desired image boundaries.

To find a solution for Equation 5.5, $\mathbf{C}(s)$ is treated as a discrete system of normalized arc length s and time t:

$$\frac{\partial \mathbf{C}(s,t)}{\partial t} = \alpha \mathbf{C}''(s,t) - \beta \mathbf{C}''''(s,t) - \nabla \mathbf{E}_{ext}. \tag{5.7}$$

When the solution $\mathbf{C}(s,t)$ becomes stationary, $\frac{\partial \mathbf{C}(s,t)}{\partial t}$ tends to zero, the energy $\mathbf{E}$ reaches a minimum, and the curve converges toward the target boundary.

5.1.2 Gradient Vector Flow Snake

The traditional snake algorithm can solve a number of image segmentation problems effectively, particularly in detection of "weak"-boundaries. However, there are two key limitations. First, the capture range of the external force fields is limited, as seen in Figure 5.1(b). The external forces $\mathbf{F}_{ext}$ have large values near the boundaries and small values in the homogeneous regions. Consequently, it is difficult for a curve to converge in regions of low variations in intensity. The traditional snake algorithm is, therefore, sensitive to the initial contour, and the initial contour should be somewhat close to the true boundary. Otherwise, the curve will likely converge to an incorrect result. Second, it is difficult to progress into boundary concavities. According to these limitations, [78] introduced the gradient vector flow (GVF) snake to expand the capture range of the external force fields from the boundary regions to the homogeneous regions, as seen Figure 5.1(c).

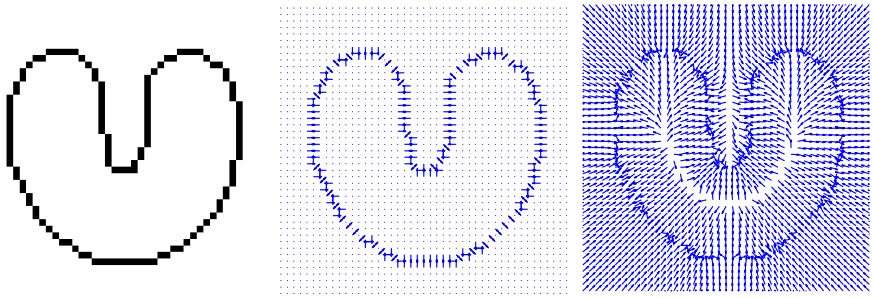

(a) Original image (b) Traditional external force (c) GVF external force

Figure 5.1: External forces.

The GVF, "computed as a spatial diffusion of the gradient of an edge map derived from the image" [79], is defined to be the vector field $\mathbf{v}(x,y) =$

$(u(x,y), v(x,y))$ that minimizes the energy functional:

$$\epsilon = \iint [\mu(u_x^2 + u_y^2 + v_x^2 + v_y^2) + |\nabla f|^2 |\mathbf{v} - \nabla f|^2] \mathrm{d}x\mathrm{d}y, \tag{5.8}$$

where u_x, u_y, v_x, v_y are the derivatives of the vector field, μ is a parameter that controls the balance between the first and second term in the integrand, and f is an edge map (which could be the image gradient $|\nabla \mathbf{I}(x,y)|^2$) that is larger near the edges of objects in the image.

In Equation 5.8, $|\nabla f|$ becomes large close to the object boundaries; in which case, the second term dominates the integrand and is minimized by $\mathbf{v} = \nabla f$. Otherwise, $|\nabla f|$ is small, and the first term dominates the integrand to ensure that the external force field varies slowly and still acts in the homogeneous regions.

The GVF field can be found by solving the Euler equations:

$$\mu \nabla^2 u - (u - f_x)(f_x^2 + f_y^2) = 0, \tag{5.9a}$$
$$\mu \nabla^2 v - (v - f_y)(f_x^2 + f_y^2) = 0. \tag{5.9b}$$

A solution to Equation5.9a and Equation 5.9b can be obtained by introducing a time variable, t, and finding the steady-state solution of the following partial differential equations:

$$u_t(x,y,t) = \mu \nabla^2 u(x,y,t) - (u(x,y,t) - f_x(x,y))(f_x(x,y)^2 + f_y(x,y)^2), \tag{5.10a}$$
$$v_t(x,y,t) = \mu \nabla^2 v(x,y,t) - (v(x,y,t) - f_y(x,y))(f_x(x,y)^2 + f_y(x,y)^2). \tag{5.10b}$$

Compared to the external force field in the traditional snake model having only f_x and f_y, the new vector fields, u and v in the GVF, are derived using an iterative method to find a solution for f_x and f_y. The result is that the capture range is effectively enlarged, and the initial contour no longer needs to be as close to the true boundary.

5.2 Contours Initialization for the GVF Snake

The GVF snake algorithm [78] is able to detect the weak connections between floes and ensures that the detected boundary is closed. As an example, shown in Figure 5.2(b), given an initial contour (red curve), the snake finds the floe

boundary (green curve) after a few iterations (yellow curves). The GVF snake is faster and less restricted by the initial contour. However, a proper initial contour is still necessary because the snake deforms itself to conform with the nearest salient contour.

5.2.1 The location of initial contour

An example is given in Figure 5.2 to illustrate the floe boundary detection results affected by initializing the contour at different locations. In Figure 5.2(a), the initial contour is located at the water, close to the ice boundaries. The snake rapidly detects the boundaries however, not the ice but the boundaries of the water region. When initializing the contour at the center of an ice floe, as shown in Figure 5.2(b), the snake accurately finds the boundary after a few iterations even if the initial contour is some distance away from the floe boundary.

A weak connection will also be detected if the initial contour is located on it, as shown in Figure 5.2(c). However, when the initial contour is located near the floe boundary inside the floe, as shown in Figure 5.2(d), the snake may only find a part of the floe boundary near the initial contour. It should be noted that the curve is always closed regardless of how it deforms, even in the cases of Figures 5.2(c) and 5.2(d), which appear to be non-closed curves. This behavior occurs because the area bounded by the closed curve tends toward zero.

Figure 5.2 illustrates that, with proper parameters, the snake will find a boundary regardless of where the initial contour is located. This fact is beneficial for connected floe segmentation. By comparing the results of Figure 5.2, the results where the initial contours are located inside of the floes are more effective, whereas the most efficient case is the one in which the initial contour is in the center of the ice floe. Thus, the initial contour should be located as close to the floe center as possible.

5.2.2 The shape and size of the initial contour

In the GVF snake algorithm, the initial contour does not need to be as close to the true boundary as for in the traditional snake algorithm. However, if the initial contour is too small, it will be slightly “far away” from the floe boundary and will need more iterations to find the boundary if the initial contour is further distanced from the floe boundary, and it may also converge to an incorrect result [78] (particularly when the grayscale of floe is uneven).

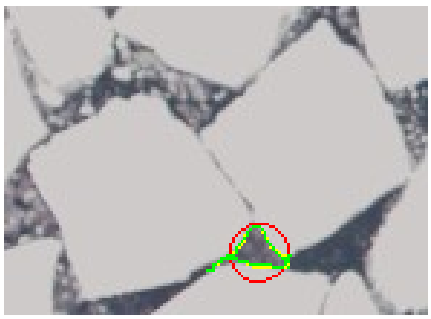

(a) Initial contour 1 located at the water, and the water region boundary is found.

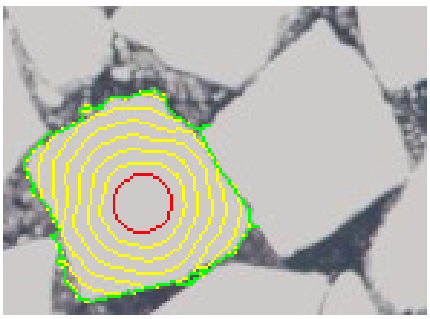

(b) Initial contour 2 located at the center of an ice floe, and the whole floe boundary is found.

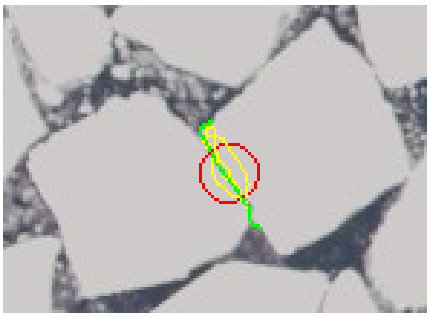

(c) Initial contour 3 located at a weak connection, and the weak connection is found.

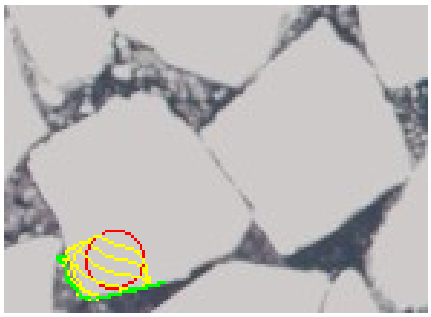

(d) Initial contour 4 located near the floe boundary inside the floe, and only a part of floe boundary is found.

Figure 5.2: Initial contours located at different positions and their corresponding curve evolutions. The red curves are the initial contours, the yellow curves are iterative runs of the GVF snake algorithm, and the green curves are the final detected boundaries.

Figure 5.3 serves as an example. Figure 5.3(a) contains some light reflection in the middle of a model-ice floe where the pixels that belong to the reflection are lighter than the other pixels of the floe. And Figure 5.3(d) contains speckle inside of a sea-ice floe where the pixels of the speckle are darker. These phenomenons will affect the boundary detection when the initial contour (the red curves in Figures 5.3(b) and 5.3(e)) is too small and not close to the actual boundary. The snake uses many steps (the yellow curves in Figures 5.3(b) and 5.3(e)) and find a part of floe boundary (the green curve in Figure 5.3(b)), or does not find the complete boundary being blocked by the speckle (the green curve in Figure 5.3(e)). If we enlarge the initial contour, as shown in Figures 5.3(c) and 5.3(f), the initial contour allows for a faster determination of the entire floe boundary. Therefore, the initial contour should still be set as possible as close to the actual floe boundary.

5.2.3 Automatic contour installation based on the distance transform

The GVF snake operates on the grayscale image in which the real boundary information, particularly "weak"-boundaries, has been preserved. Moreover, the GVF snake will ensure that the detected boundary is a closed curve. To separate seemingly connected floes into individual ones, the GVF snake algorithm is applied in this chapter. However, to start the algorithm, many initial contours are required when performing the GVF snake algorithm to identify all individual ice floes, and these should have proper locations, shapes, and sizes. Otherwise, the snake may evolve incorrectly. Therefore, a manual initialization is required in some cases, particularly in crowded floes segmentation. To solve this problem, an automatic contour installation algorithm is devised to avoid manual interaction and increase the efficiency of the ice image segmentation method based on the GVF snake algorithm.

As discussed in Section 5.2.1, the initial contours should be located inside the floes to increase the algorithm's effectiveness. In ice image analyses, the ice floes can be separated from water and converted into a binary image by using a thresholding method or k-means clustering method [30, 50]. These methods make it easy to locate the initial contours inside of the ice floes. We propose to use the distance transform [80, 81] and its local maxima to locate the initial contours as close as possible to the floe centers.

Given a binary image $f(x, y)$, whose elements only have values of '0' and '1', the pixels with a value of '0' indicate the background, while the pixels with a value of '1' indicate the object. Let $B = \{(x, y)|f(x, y) = 0\}$ be the set of background pixels and $O = \{(x, y)|f(x, y) = 1\}$ be the set of object pixels.

(a) Model-ice floe image with light reflection.

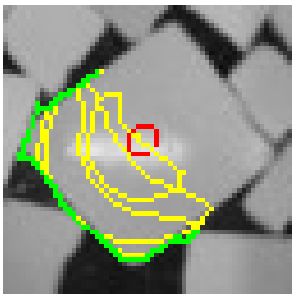

(b) A small contour initialized at the model-ice floe center, giving convergence of the snake to the incomplete boundary.

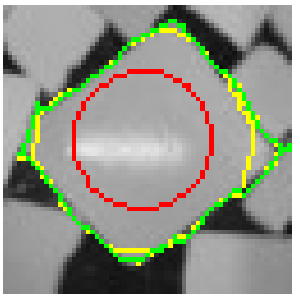

(c) A large contour initialized at the model-ice floe center, giving convergence of the snake to the correct boundary.

(d) Sea-ice floe image with speckle.

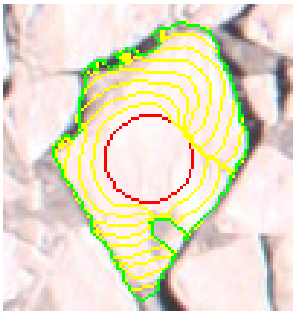

(e) A small contour initialized at the sea-ice floe center, giving erroneous evolutions of the snake.

(f) A large contour initialized at the sea-ice floe center, giving convergence of the snake to the correct boundary.

Figure 5.3: Initial circles with different radii and their curve evolutions. The red curves are the initial contours, the yellow curves are iterative runs of the GVF snake algorithm, and the green curves are the final detected boundaries.

The distance transform of a binary image f, $\mathbf{D}(x, y)$, is the minimum distance from each pixel in f to the background B, that is,

$$\mathbf{D}(x, y) = \begin{cases} 0 & \text{if } (x, y) \in B \\ \min_{b \in B} d[(x, y), b] & \text{if } (x, y) \in O, \end{cases} \tag{5.11}$$

where $d[(x, y), b]$ is some distance measure between pixel (x, y) and b [81].

For example, Figure 5.4(a) shows a small binary image matrix for a simple shape, and the matrix in Figure 5.4(b) shows the corresponding distance transform (using 'city block' distance metrics). The local maximum is the pixel whose value is greater or equal to any of its neighbors, as shown by the green numerals in Figure 5.4(b). A local maximum of the distance transform ideally corresponds to the center of an object, but more than one local maximum is detected in many cases. Thus, a dilation operator [63] is used to merge the local maximum within a short distance (within as a threshold T_{seed}) of each other. The centers of the dilated regions (red '+' in Figure 5.4(b)), which are called 'seeds', are chosen as the locations of the initial contours.

0	0	0	0	0	0	0	0
0	1	1	1	1	1	0	0
0	1	1	1	1	1	1	0
0	1	1	1	1	1	1	0
0	0	1	1	1	1	1	0
0	0	1	1	1	1	0	0
0	0	0	0	1	1	0	0
0	0	0	0	0	0	0	0

(a) Binary image matrix.

0	0	0	0	0	0	0	0
0	1	1	1	1	1	0	0
0	1	2	2	2	2	1	0
0	1	2	3	3	2	1	0
0	0	1	2	3	2	1	0
0	0	1	1	2	1	0	0
0	0	0	0	1	1	0	0
0	0	0	0	0	0	0	0

(b) Distance transform of Figure 5.4(a), local maximum, seed, and initial contour.

Figure 5.4: Contour initialization algorithm based on distance transform.

Moreover, to efficiently approach the floe boundary, as discussed in Section 5.2.2, the initial contours should be adapted to the floe sizes. Being unaware of the floe's irregular shape and orientation, the circular shape is chosen as the shape of the initial contour since this shape deforms to the floe boundary more uniformly than other shapes. The radius of the circle is then chosen according to the pixel value at the seed in the distance map. This ensures that the initial circle is inside the floe as shown, as blue circles in Figure 5.4(b), and will iteratively approach the floe boundary using adaptive initial circles

(Note: since the 'city block' distance is used to decrease the number of local maximum, the pixel values at seeds must be divided by $\sqrt{2}$ to obtain the circle radii).

After initializing the contours, the GVF snake algorithm is run on each contour to identify the floe boundary. Superimposing all the boundaries over the binarized ice image results in separation of the connected ice floes. The final segmentation result of Figure 5.5(e) is shown in Figure 5.5(f). Note that the boundary pixels are specifically labeled as "residue ice" for special handling in subsequent use.

5.3 Ice Image Segmentation

According to Section 5.2, we propose the following algorithm to segment the ice image. First, the GVF is derived from the grayscale input image. Then, the ice pixels are separated from water pixels, and the image is converted into a binary one. Next, the distance transform is applied to the binary image, and the seeds and radii are found. Finally, based on the seeds and radii, the circles are initialized and the snake algorithm is run. The pseudocode of the proposed algorithm is given in Algorithm 1, and its procedure carried out on a sea-ice floe image is shown in Figure 5.5.

Algorithm 1 Ice image segmentation.

Input: Ice image

Start algorithm:

1: $GVF \leftarrow$ GVF derived from grayscale of input image
2: $SEGMENTATION \leftarrow$ binary ice image
3: $D \leftarrow$ distance map of $SEGMENTATION$
4: $M \leftarrow$ local maximum of D
5: $S \leftarrow$ Seeds of $SEGMENTATION$ found by merging the local maximum in M within a short distance (T_{seed})
6: **for** each seed $s \in S$ **do**
7: $r \leftarrow$ local maxima values at s
8: $c \leftarrow$ initial contours locate at s with its radius r
9: $B \leftarrow$ boundary detected by performing the snake algorithm on c
10: $SEGMENTATION \leftarrow SEGMENTATION$ with B superimposed
11: **end for**
12: **return** $SEGMENTATION$

Output: Segmented ice image

(a) Sea-ice floe image.

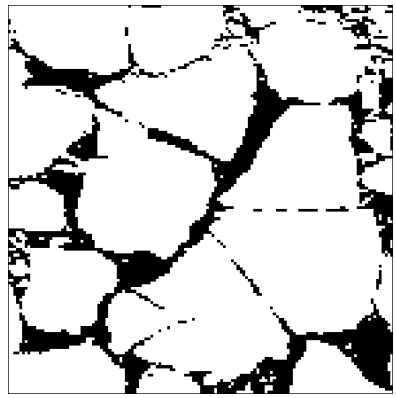

(b) Binary image. The ice floes are connected.

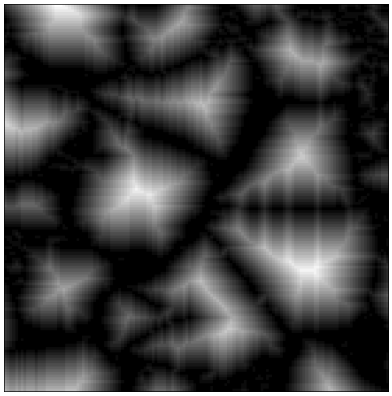

(c) Distance transform.

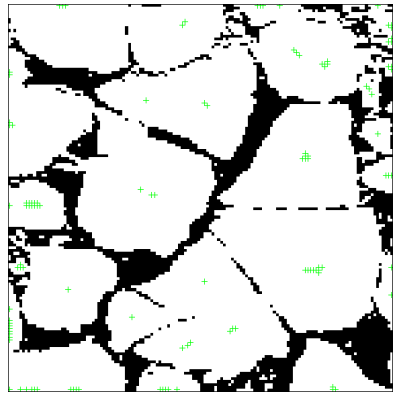

(d) Binary image with local maxima (green '+').

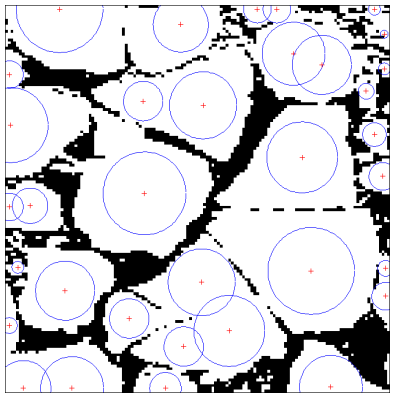

(e) Binary image with seeds (red '+') and initial contours (blue circles).

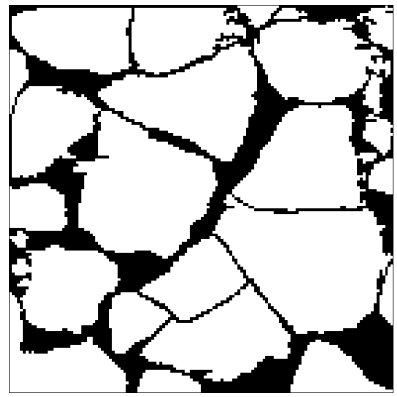

(f) Segmentation result. The connected ice floes are separated.

Figure 5.5: The procedure of ice segmentation algorithm.

It should be noted that the local maximum whose distance is larger than the given threshold T_{seed} will not be merged into one seed. This means that some floes may have more than one seed. However, two or more seeds for one ice floe will not affect its boundary detection, but it may increase the computational time.

5.4 Ice Shape Enhancement

After segmentation, some segmented ice floes may contain holes or smaller ice pieces inside because of the noise, as shown in Figure 5.6, and the shape of the detected ice floe is rough. To smoothen the shape of the ice floe, morphological cleaning [82] is used after ice floe segmentation.

(a) Ice floe image with speckle. (b) Segmentation result of (a).

Figure 5.6: The segmentation of ice floe image with speckle. The segmented floes contain holes and smaller ice pieces inside.

Morphological cleaning is a combination of first morphological closing and then morphological opening [63] on an image. The morphological closing of A by B, denoted $A \bullet B$, is a dilation followed by an erosion:

$$A \bullet B = (A \oplus B) \ominus B \tag{5.12}$$

where A is the image, B is the structuring element, "$\oplus$" is the dilation operation, and "$\ominus$" is the erosion operation (the details of dilation and erosion operations can be found in Chapter 3). It is the complement of the union of all translations of B that do not overlap A.

The morphological opening of A by B, denoted $A \circ B$, is an erosion followed by a dilation:

$$A \circ B = (A \ominus B) \oplus B \tag{5.13}$$

It is the union of all the translations of B that fit entirely within A.

The morphological closing tends to smooth the contours of objects, generally joins narrow breaks, fills long thin gulfs, and fills holes smaller than the structuring element, while the morphological opening removes complete regions of an object that cannot contain the structuring element, smooths object contours, breaks thin connections, and removes thin protrusions. Figure 5.7 illustrates the morphological cleaning and shows the effects of closing and opening.

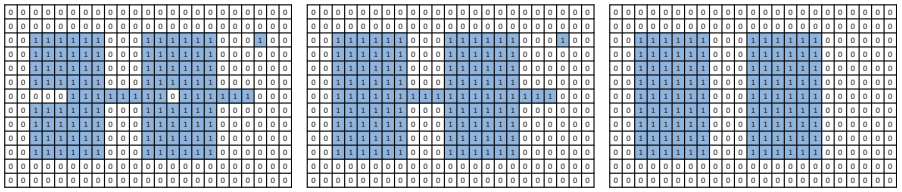

(a) Binary image. (b) Closing of (a). (c) Opening of (b).

Figure 5.7: Morphological cleaning by using a 2×2 square structuring element.

Using the morphological cleaning, all the segmented ice pieces derived from the ice floe segmentation result of Algorithm 1 are first arranged from small to large. Then, morphological cleaning with a proper structuring element is performed and holes are filled to the arranged ice pieces in sequence. The pseudocode of the proposed ice shape enhancement algorithm is concluded in Algorithm 2, and the ice shape enhancement result of Figure 5.6(b) is shown in Figure 5.8.

Algorithm 2 Ice shape enhancement.

Input: Ice segmentation from Algorithm 1.

Start algorithm:

1: $PIECES \leftarrow$ labeled regions in $SEGMENTATION$ arranged from small to large.
2: $BW \leftarrow$ empty black image.
3: **for** each labeled region $piece \in PIECES$ **do**
4: $\quad piece \leftarrow$ morphological clean and fill hole.
5: $\quad BW \leftarrow BW$ with $piece$ superimposed and labeled.
6: **end for**
7: $IDENTIFICATION \leftarrow$ labeled regions in BW.
8: **return** $IDENTIFICATION$.

Output: Individual ice piece identification.

Figure 5.8: Ice shape enhancement result of Figure 5.6(b). The holes and smaller ice pieces inside larger floes are removed.

It should be noted that the arrangement of ice pieces in order of increasing size is required for the morphological cleaning. Otherwise, the smaller ice piece contained in a larger ice floe may not be removed.

5.5 Discussion

In this chapter, we have proposed an automatic contour initialization procedure based on the distance transform for the GVF snake algorithm to separate seemingly connected ice floes into individual ones and an ice shape enhancement algorithm based on the morphological cleaning for segmented ice image to accomplish the identification of individual ice floes. The proposed methods are applicable for non-ridged ice floe segmentation. Additionally the implementations on sea-ice images, which contain multiple ice floes connected together, produce acceptable segmentation results and demonstrate that the proposed algorithms are effective for individual ice floe identification. The further applications and discussions of the methods are presented in Chapter 6 and Chapter 7.

Chapter 6

Model Ice Image Processing

An image processing method based on a GVF snake and a distance transform was proposed to identify ice floe boundaries in Chapter 5. Ice floe characteristics, such as position, area, and size distribution, which are important ice parameters in ice-structure analyses, can then be obtained. Before performing an analysis at full-scale, the DP experiments in model ice at the Hamburg Ship Model Basin (HSVA) allow for the testing of relevant image processing algorithms. A complete overview image of the ice floe distribution in the ice tank was generated from the experiments. The main focus of this chapter is on model-ice images in model-scale. Based on the characters of the model-ice floes, a model of the managed ice field's configuration, including identification of overlapping floes, is proposed in this chapter for further studies in ice-force numerical simulations. Finally, the proposed algorithm is applied to an ice surveillance video to further illustrate its applicability to ice management. The work presented in this chapter was published in [55].

6.1 Locating Initial Contours for Crowded Model-ice Floes

Figure 5.5 in Chapter 5 presents an acceptable result of the proposed algorithm applied in a case with only two or three connected ice floes. However, in a complex case (e.g., Figure 6.1), when multiple model-ice floes are crowded together, it then becomes more difficult to locate the seeds for each ice floe (as shown in Figure 6.1(b)) with the result that some connected ice floes could not be separated (as shown in Figure 6.1(c)). It follows that an additional round of contour initialization and segmentation is necessary.

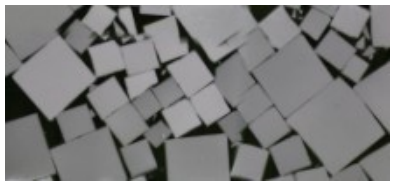

(a) Model-ice image with crowded floes.

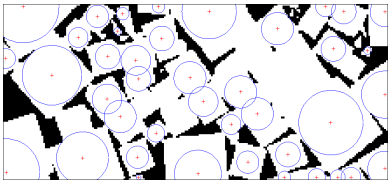

(b) Initializing the contours once.

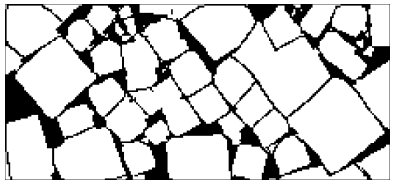

(c) Results after first round.

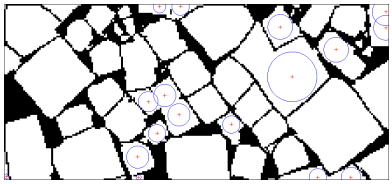

(d) Initializing the contours twice.

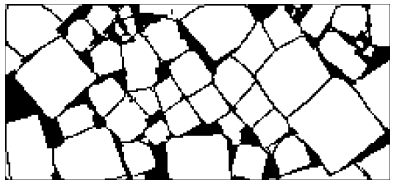

(e) Final result.

Figure 6.1: Crowded model-ice floes segmentation.

In this model-ice test, the ice floes were modeled square shapes with predefined side lengths. Hence, the largest floe has an area less than a predefined value. Although they are not perfect squares, most of the floes could be approximated as rectangles with a length-to-width ratio less than the given threshold. Based on these characteristics, we use three criteria to determine whether it is necessary to initialize the contours and conduct a second segmentation:

- The ice floe area is less than the given threshold.
- The ice floe has a convex shape (the ratio between the floe area and its minimum bounding polygon area is larger than the threshold).
- The length-to-width ratio of the minimum bounding rectangle of the ice floe is less than the threshold.

After a segmentation step, the algorithm will stop if all the identified floes satisfy these criteria. Otherwise, the algorithm must find the floes that do not satisfy any of these criteria, calculate their distances, find the new seeds, initialize new contours, and perform the segmentation again. Some boundaries may exist that are too weak to be detected, and there may be some floes that do not satisfy the criteria after a new step. However, the total number of identified floes will converge to a final solution. Therefore, the algorithm is made to stop if the total number of floes identified after step N and $N + 1$ are equal, in combination with an absolute stop criterion.

6.2 Algorithm Overview

According to Section 6.1, we propose the following algorithm to segment the model-ice floe image. First, the GVF is derived from the grayscale input image. Then, the ice floes are separated from water by using the thresholding method, and the floes are labeled. Each labeled floe should then be checked to determine whether it satisfies all of the criteria in Section 6.1. Next, the seeds and radii of the floes that do not satisfy any of the criteria are found. Based on the seeds and radii, the circles are initialized and the snake algorithm is run. The algorithm will stop when meet the maximum iteration time, or the total number of floes identified after step N and $N + 1$ are equal. The pseudocode of the proposed algorithm, as well as a maximum iteration time, is given in Algorithm 3.

Algorithm 3 Model ice floe segmentation.

Input: Model ice image

Start algorithm:

1: $T \leftarrow$ max iteration time
2: $N_0 \leftarrow 0$
3: $GVF \leftarrow$ GVF derived from gray-scale of input image
4: $BW \leftarrow$ binary image
5: $FLOE \leftarrow$ labeled ice floes in BW
6: $N_1 \leftarrow$ total number of ice floes in BW
7: **if** $N_0 \neq N_1$ && $T \neq 0$ **then**
8: **for** each labeled $floe \in FLOE$ **do**
9: $f \leftarrow$ floes that do not satisfy any of the criteria
10: **end for**
11: $k \leftarrow$ number of f
12: **if** $k \neq 0$ **then**
13: $S \leftarrow$ Seeds of f found by local maxima of distance transform
14: **for** each seed $s \in S$ **do**
15: $r \leftarrow$ local maxima values at s
16: $ic \leftarrow$ initial contours locate at s with its radius r
17: $B \leftarrow$ boundary detected by performing the snake algorithm on ic
18: $BW \leftarrow BW$ with B superimposed
19: **end for**
20: **end if**
21: $N_0 \leftarrow N_1$
22: $T \leftarrow T - 1$
23: go back to 4
24: **end if**
25: **return** BW

Output: Segmented image

6.3 Experimental Results and Discussions

In the model ice test carried out at the ice model basin of the HSVA in the summer of 2011 [50], a managed ice condition was obtained by cutting a manufactured level ice layer into square pieces with specific dimensions and distributing them over a specific testing area. After preparing the ice field and before the test run started, a top-view camera was positioned over the total ice-covered basin to produce an overall image of the complete ice field.

To validate the proposed algorithm, it has been tested on both sub-images and an overall ice tank image. In these tests, the segmented ice pieces with the area less than 20 pixels were taken as brash ice and removed from the ice floe segmentation results. However, the removed pixels can be presented in another separated layer for further use.

6.3.1 Sub-image tests

The sub-images were manually extracted from the overall ice tank image, and the algorithm was tested on both the simple and complex cases.

Figure 6.2 presents the simplest case, that is, only two or three ice floes connected with clear boundaries. The proposed algorithm found all of the seeds in the first iteration and rapidly located the boundaries. In the case illustrated in Figure 6.3, many ice floes are crowded in the image. After several iterations of seed locating, the algorithm produced satisfactory results in the high-density part of the image while failing to find a few weak boundaries.

(a) Model-ice image 1.

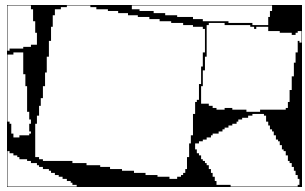

(b) Segmentation 1.

Figure 6.2: Segmentation result 1.

The junctions between a number of ice floes and ice rubble were also too weak to be detected, as shown in Figure 6.4(b). Because the area of the ice rubble is too small relative to the area of its connected ice floe, the snake was rapidly attracted to the rubble boundaries when it deformed at the junction.

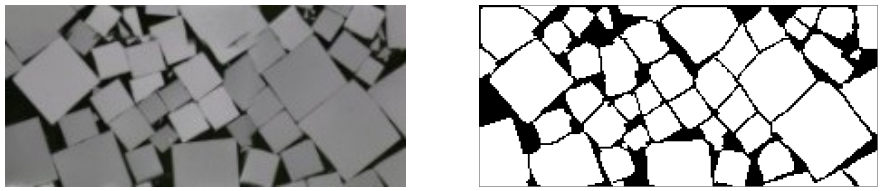

(a) Model-ice image 2. (b) Segmentation 2.

Figure 6.3: Segmentation result 2.

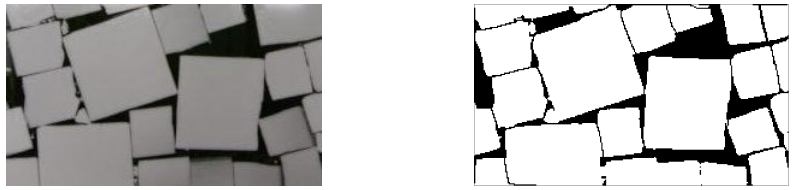

(a) Model-ice image 3. (b) Segmentation 3.

Figure 6.4: Segmentation result 3.

The most complex case is shown in Figure 6.5, where the crowded ice floes were aligned in the image. The segmentation result indicates that the proposed algorithm still performs well with the exception of a number of border effects.

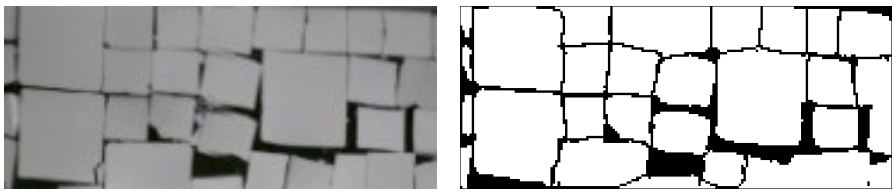

(a) Model-ice image 4. (b) Segmentation 4.

Figure 6.5: Segmentation result 4.

The segmentation of the floes situated at the border of the analyzed image is more prone to error. The algorithm failed to detect a number of ice floe boundaries connected to the border of the image, as shown in Figures 6.4(b) and6.5(b). This occurred not only because these floes were being "cut" by the image border and do not fulfill the criteria formulated in Section 6.1, but also because the incompleteness of the floe influences the GVF field and makes some boundary information weaker. As shown in Figure 6.6, the GVF field of a complete floe radiates from the floe center to its boundaries. The proposed

algorithm then successfully finds all the boundary pixels. Contrary to this, if some of the floe boundary is lost due to an image border, the GVF field of this incomplete floe will radiate from the image border to the floe boundaries, with the result that the segmentation by the snake algorithm fails.

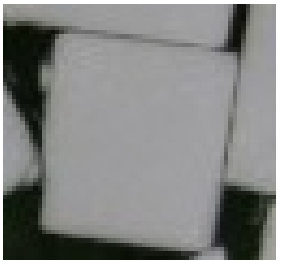

(a) Model-ice image contained a complete floe.

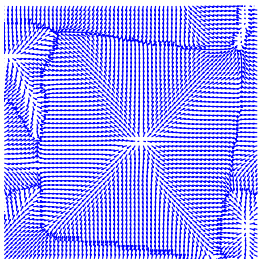

(b) The GVF field of (a) radiates from the floe center to its boundaries.

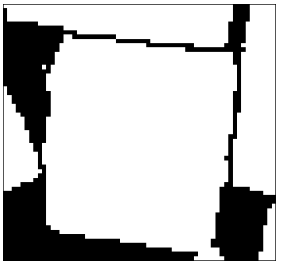

(c) Segmentation result of (a). All the boundary pixels are found.

(d) Model-ice image contained an incomplete floe.

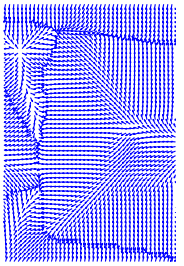

(e) The GVF field of (d) radiates from the image border to the floe boundaries.

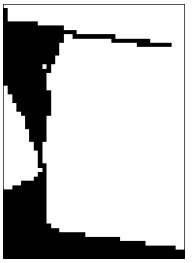

(f) Segmentation result of (d). Some of the floe boundary is lost.

Figure 6.6: Image border effects.

6.3.2 Overall ice tank image

The overall ice tank image, obtained by a top-view camera, provides a complete overview of the ice floe distribution in the ice tank (see Figure 6.7). The lightness of the image is rather uneven, and the nonuniform illumination will affect the segmentation result. An illumination correction, such as homomorphic filtering [59] that normalizes the brightness across an image, is adopted to preprocess the image. After performing the proposed segmentation algorithm, the black spots inside the segmented ice floes caused by noise will be filled in the ice shape enhancement step. The identification result is shown in Figure

6.8(a).

The floes are labeled using different colors based on their areas (calculated by counting the pixel number of the floe) according to

$$\mathbf{Color}(p) = \begin{cases} 0 & \text{if } p \notin FLOE \\ (1 - \exp(-area(i)/1000)) * 10000 & \text{if } p \in floe(i), \end{cases} \quad (6.1)$$

where $FLOE = \{floe(1), floe(2), floe(3), \cdots\}$ is a set of identified floes, $floe(i) \in FLOE$, and $area(i)$ is the area of $floe(i)$. Smaller floes are blue, and larger floes are red. The floe positions, found by averaging the positions of the pixels of each floe, are denoted using black dots. The corresponding size distribution histogram is presented in Figure 6.8(b).

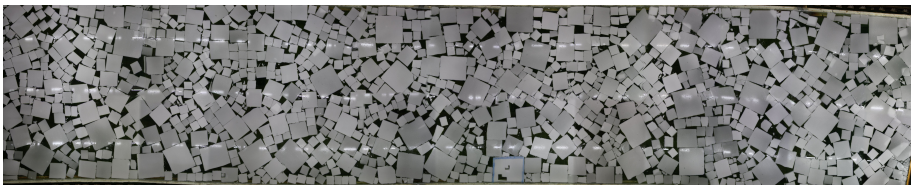

Figure 6.7: Overall model-ice tank image.

However, the identification result shown in Figure 6.8(a) is not ideal. A number of over- and under-segmentations still exist because a uniform parameter for the GVF field cannot represent the overall ice image. For instance, if we switch the GVF capture ranges of Figure 6.4 and Figure 6.5, then error segmentations will occur (see Figure 6.9).

When using the same GVF parameter, which controls the capture range of the GVF, the external forces near weak connections are weaker than those near strong boundaries. If the GVF capture range is too strong, the capture range of the strong boundaries will dominate the entire external force field while the external force near the weak connections will be too weak to pull the snake toward the desired boundaries. Usually, weak connections tend to be more difficult to detect when increasing the GVF capture range, which results in under-segmentation. In contrast, if the capture range is decreased, the noise is enhanced and leads to over-segmentation.

In an image containing overlapping ice floes, as shown in Figure 6.10(a), the overlapping part is brighter than the rest of the floe. When segmenting the image using a low GVF capture range, boundaries are extracted, but the two overlapped floes are identified as three individual floes (Figure 6.10(b)). When increasing the GVF capture range, the weaker boundary is lost, and the two

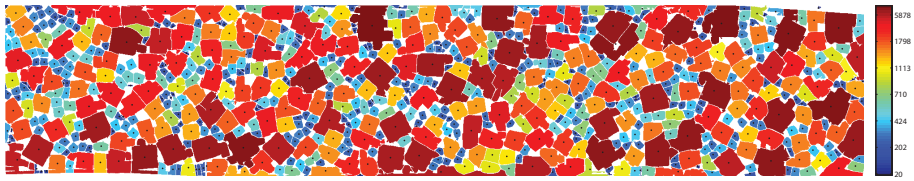

(a) Segmentation result after illumination correction.

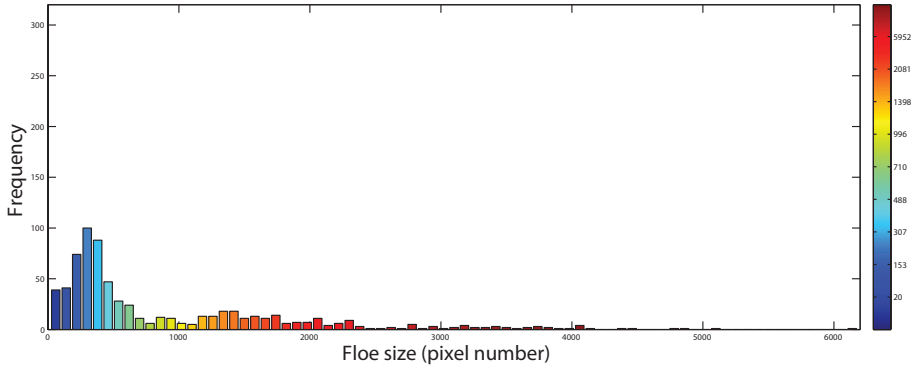

(b) Ice floe size distribution histogram of (a).

Figure 6.8: Ice floe identification after illumination correction and floe size distribution.

overlapped floes are divided. However, one of the floes loses half of its area. Thus, processing the local sub-images of the overall ice image locally is recommended in order to identify all of the boundaries.

Figure 6.9: Error segmentation by using improper parameters.

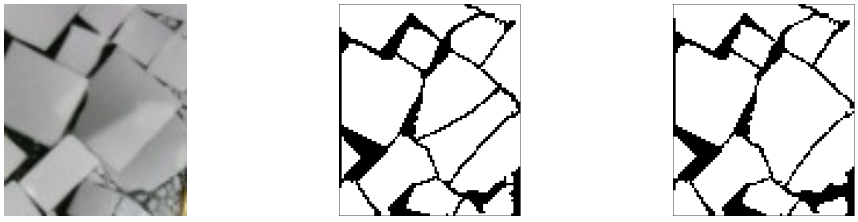

(a) Overlapping floes image.

(b) Segmentation result via low GVF capture range (100 iterations for GVF).

(c) Segmentation result via high GVF capture range (150 iterations for GVF).

Figure 6.10: Overlapping floes image segmentation.

To derive a more precise result, the overall image is first divided into several smaller, overlapping (to avoid image border effects) sub-images, and we perform the proposed algorithm locally on each sub-image. The parameter values of the GVF field for each sub-image are listed in Table 6.1. The final segmentation result and its floe size distribution histogram are shown in Figures 6.11(a) and 6.11(b), respectively.

By comparing the color distribution in Figures 6.8(a) and 6.11(a) and their histograms, one can see that there are more blue ice floes and fewer red floes in Figure 6.11(a) than in Figure 6.8(a). This result indicates that a greater number of connected floes have been separated and that under-segmentation has been reduced in Figure 6.11(a). The minor under- and over-segmentation that still exists in Figure 6.11(a) is due to "overly weak" boundaries and a lingering border effect. This issue can be improved by adjusting the number, position, and size of the sub-images. These parameters were found by trial-and-error in

Table 6.1: The parameter values of the GVF field for each sub-image.

Sub-image no.	1	2	3	4	5	6	7
The GVF iteration number	150	65	65	65	160	60	110
Sub-image no.	8	9	10	11	12	13	14
The GVF iteration number	130	90	130	170	160	100	90
Sub-image no.	15	16	17	18	19	20	
The GVF iteration number	90	100	90	80	90	80	

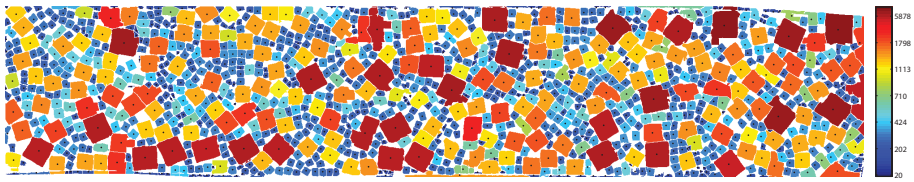

(a) Final segmentation result.

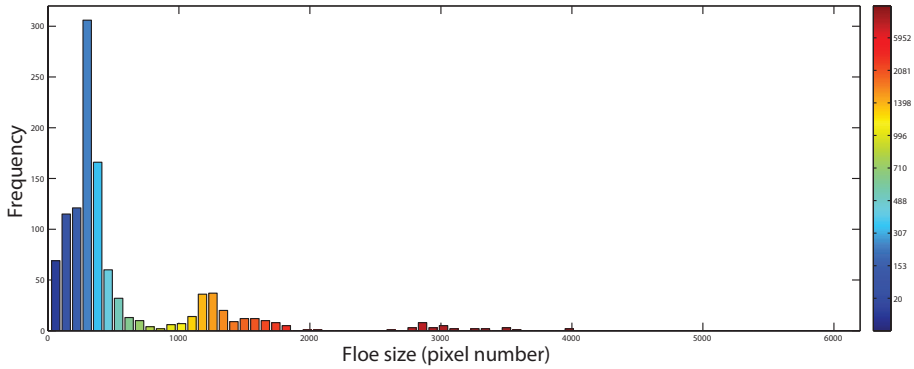

(b) Ice floe size distribution histogram of (a).

Figure 6.11: Final model-ice floe identification result and floe size distribution.

this case. The investigation on how to optimally choose these parameters is left for future research.

Light reflection also affects the segmentation results. Several lights were installed at the bottom of the ice tank to supply a sufficient brightness for the ice observation. However, these lights are detrimental to the ice image analysis because they can be identified as ice floes due to their brightness, and the light reflection on the ice floe may induce erroneous segmentation. As shown in Figure 6.12, the initial circle meets a strong light reflection when deforming, and some boundaries around the reflection become too weak to be detected. Hence, a part of the circle deformed toward the reflection rather than toward the true floe boundary. Fortunately, the light reflection did not significantly affect our result, but we still suggest that the lights be disabled or that a polarizer be placed in front of camera before taking the picture.

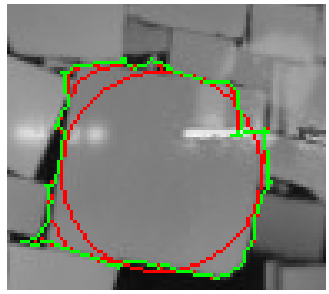

Figure 6.12: Light reflection impact, which may induce erroneous segmentation.

6.3.3 Model-ice floe modeling

In the numerical simulation of the ice-structure interaction, all of the ice floes are modeled as rectangular floes, and the positions of the vertices are important to an ice-structure analysis. Therefore, we proposed to perform ice floe rectangularization. Ice floe rectangularization was achieved by assigning the minimum area-bounding rectangle to each ice floe. Due to under- and over-segmentation, the rectangles with a length-to-width ratio less than the given threshold were removed. The final rectangularization result is shown in Figure 6.13(a). If the floes are not segmented well, the rectangularized floes will be smaller or larger than the actual segmented floes. Furthermore, because of the rectangularization, some rectangularized floes will overlap, as seen in Figure 6.13(b). To indicate overlaps, a “flag” was added to each rectangular floe to record the serial number of the floes with which the current floe overlaps.

Identifying the overlap between ice floes is important when using the resulting image analysis and identified ice floes as a starting condition for the validation of a numerical simulation with a 3D capacity against a real test and data set.

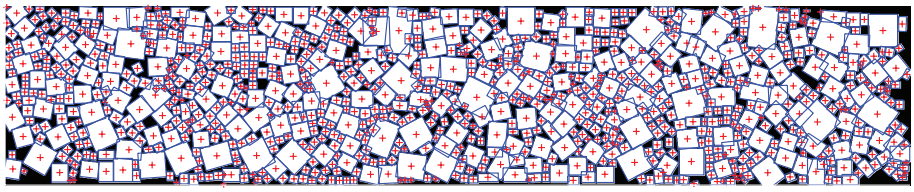

(a) Rectangularization of Figure 6.11(a).

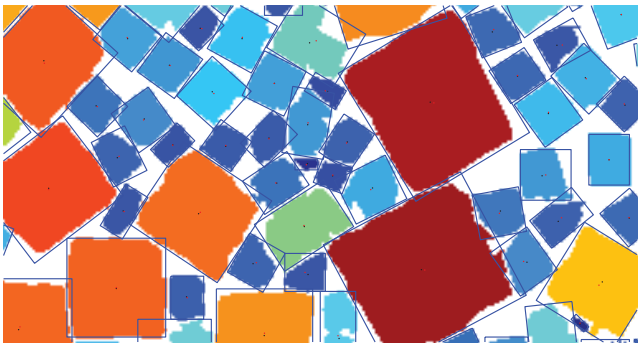

(b) Comparison between identification and rectangularization results. The blue rectangles are the boundaries of the modified floes. The black '.' are the centers of identified ice floes (brash ice pieces), and the red '.' are the centers of rectangularized floes.

Figure 6.13: Ice floe rectangularization.

The colorized histogram of the rectangular floe size distribution is presented in Figure 6.14(a). Under-segmentation could induce a large area difference as well as overlapping, which explains why the largest floe in Figure 6.13(a) is much larger than the largest identified floe in Figure 6.11(a), as seen in Figure 6.14(b) by comparing Figures 6.14(a) and 6.11(b).

6.3.4 Ice concentration

The target ice concentration in this test was 90%. The ice concentration derived from Figure 6.11(a) is 76.96%, while it is 83.17% when calculated using the threshold method [50] (estimated by counting the number of pixels for each respective area in the image). In the proposed algorithm, the ice pixels

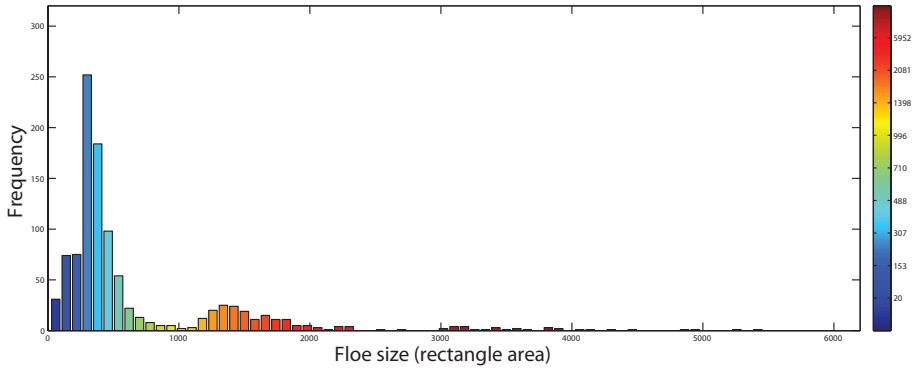

(a) Ice floe size distribution histogram of Figure 6.13(a).

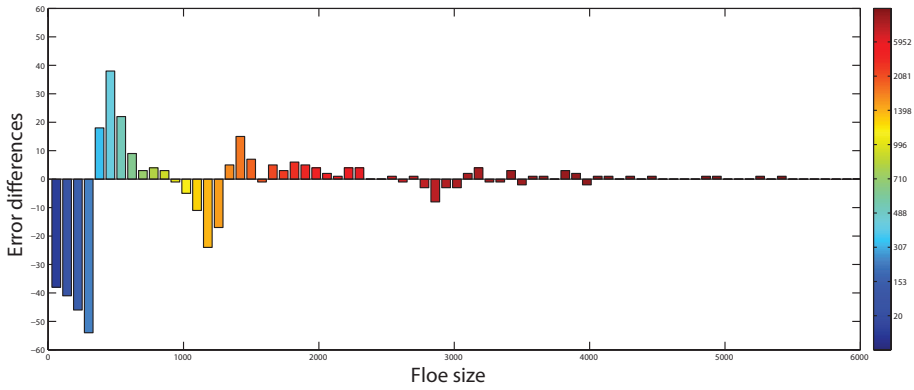

(b) Error differences between the resulting floe size distributions from Figures 6.14(a) and 6.11(b).

Figure 6.14: Rectangular floe size distribution and its error differences.

detected as a boundary were changed to water pixels (e.g., Figure 6.10), so the calculated ice concentration was reduced in Figure 6.11(a).

The ice concentration calculated by summing all the areas of the rectangular floes in Figure 6.13(a) over the image domain is 87.75%. This value is slightly higher than the thresholding result because the overlapping parts have been identified and considered. The overlapping parts compensate for the loss of ice concentration, and increase the calculated ice concentration closer to the target value.

6.4 Application: Monitoring Maximum Floe Size

An example of the proposed algorithm is to monitor the maximum floe size entering the protected vessel from a physical ice management operation. In the analyzed runs, the heading of the Arctic drillship [50] was constant at 180° and the velocity of the towing carriage with the model was increased halfway during the run. From the full-scale, velocity of 0.25 to 0.50 knots was simulated. The motion captured by the video is retrieved by analyzing at one frame per second.The impediments around the tank were removed first (as shown in Figure 6.15(a)) [50], the proposed algorithm was applied to segment the connected ice floe (Figure 6.15(b)), and the maximum floe area for each frame was calculated. Figure 6.16 presents the maximum floe size entering the protected vessel as a function of time. Based on this result, a warning can be sent to the risk management system if the estimated risk based on the maximum floe size is too large.

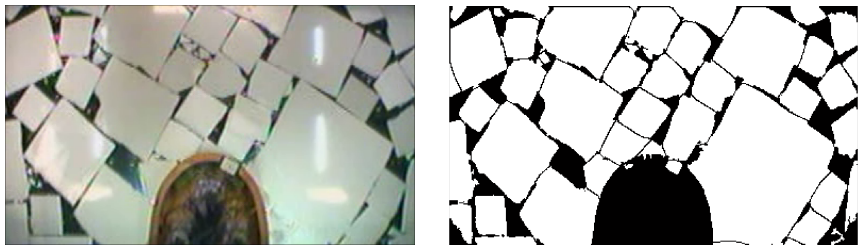

(a) Pre-processed frame at 965s. (b) Segmentation result of (a).

Figure 6.15: Model-ice video processing.

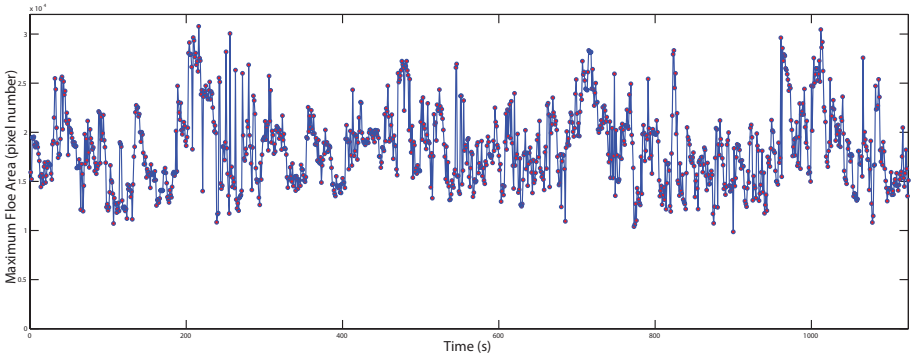

Figure 6.16: Maximum floe size entering the protected vessel.

Chapter 7

Sea-ice Image Processing

Several image processing algorithms have been applied to sea-ice images to extract useful information of sea-ice. Sea-ice, defined as any form of ice that forms as a result of sea water freezing [33, 34, 35], covers approximately 7% of the total area of the world's oceans [83]. This ice is turbulent because of wind, wave, and temperature fluctuations. Various types of ice are found in ice-covered regions. Ice floes and brash ice can range from approximately one meter to kilometers in size. The size distribution of ice floes is a basic parameter of sea-ice that affects the behavior of sea-ice extent both dynamically and thermodynamically. Particularly for relatively small ice floes, the ice floe size distribution is critical to the estimation of melting rate [27]. Hence, estimating floe size distributions contributes to the understanding of the behavior of the sea-ice extent on a global scale.

Chapter 5 proposes a method based on the GVF snake algorithm to separate seemingly connected ice floes into individual ones. This method is adopted for processing model-ice images in Chapter 6 to obtain the floe size distributions and give acceptable results. Processing a sea-ice image, however, is more challenging than a model-ice image. Sea-ice typically has a greater variability of ice floe sizes, together with a larger content of brash ice/slush and possibly a snow cover, than it has for more deterministic model-ice. On the other hand, this means that it is possible to extract the desired ice data quite accurately based on the presented methods in model-ice image processing. The main focus of this chapter is on identifying the non-ridged ice floe in the marginal ice zone and the managed ice resulting from offshore operations in sea-ice. The discussion and suggested procedure of the proposed method for processing a larger area covered and geometric distorted sea-ice image are given in the case studies. Moreover, the applications of the proposed method for ice engineering

conclude the chapter. The work presented in this chapter was published in [56, 57].

7.1 Ice Image Processing Methods

7.1.1 Sea-ice pixel extraction

Because sea-ice is whiter than water, the pixel values differ under normal conditions. Ice pixels have higher intensity values than those belonging to water in a uniform illumination ice image. Therefore, ice pixels can be extracted by using the thresholding method [58]. Most of the ice in Figure 7.1 can then be identified, as shown in Figure 7.2. Of the ice pixels identified, however, only "light ice" has larger pixel intensity values than the threshold. "Dark ice" with pixel intensity values between the threshold and water, such as ice pieces under the water surface, may not be identified, are considered to be water according to the thresholding method. Both "light ice" and "dark ice" pixels are required for an accurate analysis. To distinguish "dark ice" from open water, the k-means clustering algorithm [62] can be applied.

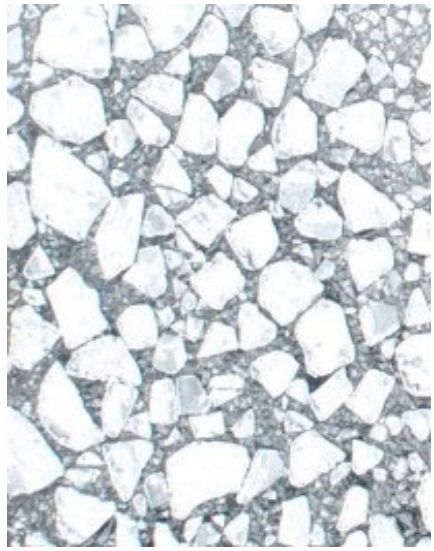

Figure 7.1: Original sea-ice image.

The image is then divided into three or more clusters using the k-means algorithm. The cluster with the lowest average intensity value is considered to be water, while the other clusters are considered to be ice, as shown in Figure 7.3.

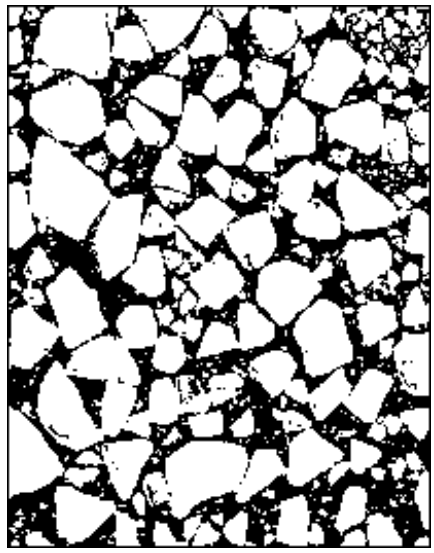

Figure 7.2: “Light ice” extracted by the thresholding method.

The “dark ice” is then obtained by comparing the difference between Figure 7.2 and 7.3, as shown in Figure 7.4.

7.1.2 Sea-ice edge detection

Chapter 6 and [55] discuss three criteria to check whether it is necessary to reinitialize the contours and segment a second time based on the size and shape of model ice floe. However, this is not necessary for the sea-ice image because of the irregular floe sizes and shapes. To obtain a more accurate result and reduce the computational time, the contours are initialized in both the “light ice” image (Figure 7.2) and “dark ice” image (Figure 7.4). The GVF snake algorithm is then run to individually derive “light ice” segmentation (the white ice pieces in Figure 7.5) and “dark ice” segmentation (the gray ice pieces in Figure 7.5). Collecting all the ice pieces in both “light ice” and “dark ice” segmentation images resulted in the segmented image, as shown in Figure 7.5. It should be noted that the “light ice” and “dark ice” should be labeled differently in the segmentation result. Otherwise, it may be impossible to separate some “light ice” and “dark ice”.

The pseudocode of the proposed ice edge detection algorithm is concluded in Algorithm 4.

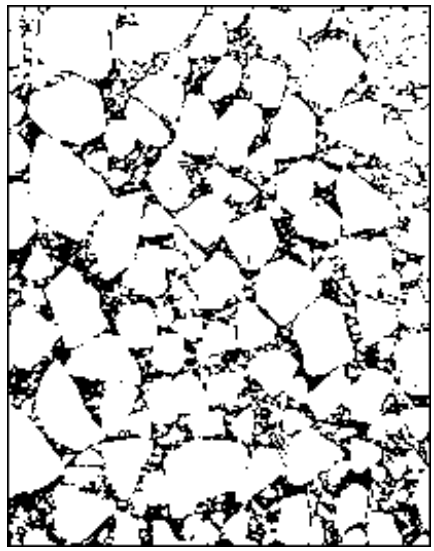

Figure 7.3: Ice extraction using the k-means method.

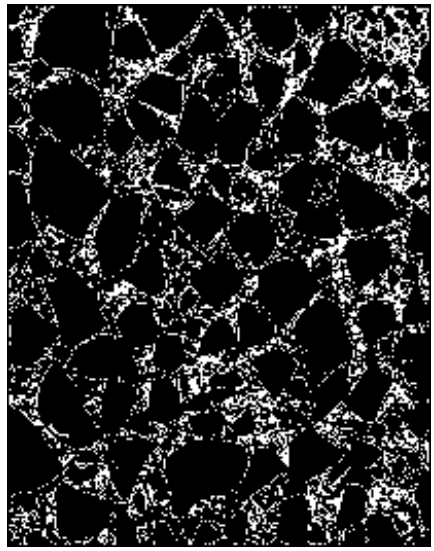

Figure 7.4: "Dark ice" found by subtracting Figure 7.2 from Figure 7.3.

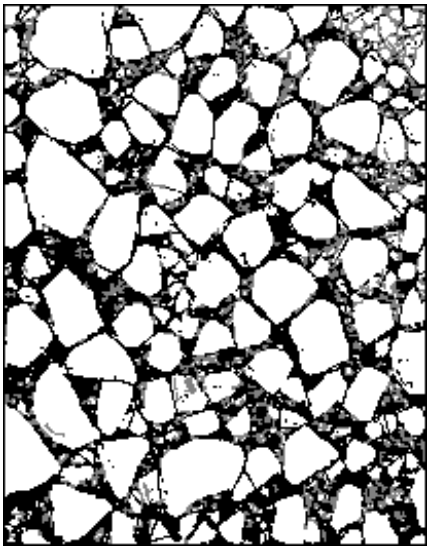

Figure 7.5: Sea-ice segmentation image. The white ice is the segmentation result from the "light ice" in Figure 7.2, and the gray ice is the segmentation result from the "dark ice" in Figure 7.4.

Algorithm 4 Sea-ice edge detection.

Input: Sea-ice image

Start algorithm:

1: $GVF \leftarrow$ GVF derived from greyscale of input image
2: $ICE \leftarrow$ binary ice image by the K-means method
3: $LIGHT \leftarrow$ binary "light" ice image by the thresholding method
4: $DARK \leftarrow ICE - LIGHT$
5: $SEG_L \leftarrow$ ice floe segmentation (Algorithm 1) on $LIGHT$
6: $SEG_D \leftarrow$ ice floe segmentation (Algorithm 1) on $DARK$
7: $SEGMENTATION_{sea-ice} \leftarrow SEG_L + SEG_L$ (SEG_L and SEG_D are marked differently in $PIECES$)
8: **return** $SEGMENTATION_{sea-ice}$

Output: Sea-ice segmentation

7.1.3 Sea-ice shape enhancement

Figure 7.6(a), which is extracted from Figure 7.1, shows an ice floe with speckle. Because of uneven grayscale of the ice floe, the lighter part of the floe is considered as "light ice" (the white pixels in Figures 7.6(b) and 7.6(c)), while the darker part is considered as "dark ice" (the gray pixels in Figures 7.6(b) and 7.6(c)) by the k-means and threshold method. This means the ice floe, as shown in Figure 7.6(b), cannot be completely identified when it has both "light ice" pixels and "dark ice" pixels. Therefore, the ice shape enhancement is particularly important for sea-ice image processing.

If we perform the ice shape enhancement to the "light ice" segmentation and "dark ice" segmentation independently, there will be overlap between the resulted "individual light ice piece identification" and "individual dark ice piece identification". This means some ice pixels are identified as belonging to different ice floes at the same time, and large ice floes are still at risk of incompleteness.

To perform the ice shape enhancement algorithm to the sea-ice segmentation image, all the collected ice pieces, including both segmented "light ice" and "dark ice" pieces, should be labeled as an input to the step of ice shape enhancement. A disk-shaped structuring element is chosen for the ice shape enhancement, and the radius of disk-shaped structuring element can be automatically adapted to the size of each ice piece according to some rules, such as Equation 7.1.

$$r = \begin{cases} r_1 & \text{if } size_{ice} < size_{th} \\ r_2 & \text{if } size_{ice} \geq size_{th}, \end{cases} \tag{7.1}$$

where r is the radius of disk-shaped structuring element. It is equal to r_1 when the size of ice piece $size_{ice}$ is less than a thresholding $size_{th}$. Otherwise it is equal to r_2.

The pseudocode of the sea-ice shape enhancement algorithm is concluded in Algorithm 5. This process will ensure the completeness of the ice floe and that smaller ice floes or brash pieces contained in a lager ice floe are removed, as shown in the shape enhancement result in Figure 7.6(c).

After shape enhancement, collecting and labeling all the cleaned ice pieces in different colors based on the Equation 6.1, results in Figure 7.7.

Algorithm 5 Sea-ice shape enhancement.

Input: Sea-ice segmentation from Algorithm 4.

Start algorithm:

1: $PIECES_{sea-ice} \leftarrow$ labeled regions in $SEGMENTATION_{sea-ice}$.

2: $IDENTIFICATION_{sea-ice} \leftarrow$ ice shape enhancement (Algorithm 2).

3: **return** $IDENTIFICATION_{sea-ice}$.

Output: Individual sea-ice piece identification.

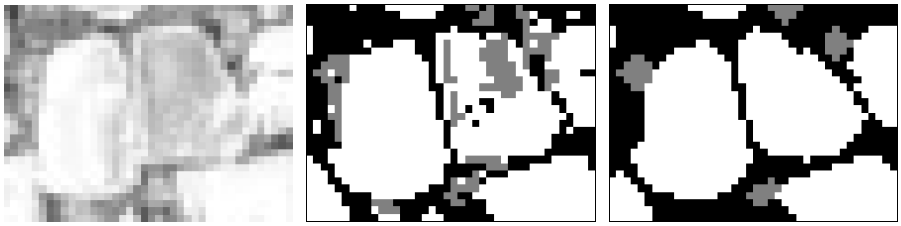

(a) Ice floe image extracted from Figure 7.1.

(b) Segmentation result of Figure 7.6(a).

(c) Shape enhancement result of 7.6(b).

Figure 7.6: Sea-ice shape enhancement. The white pixels are "light ice" pixels, and the gray pixels are "dark ice" pixels.

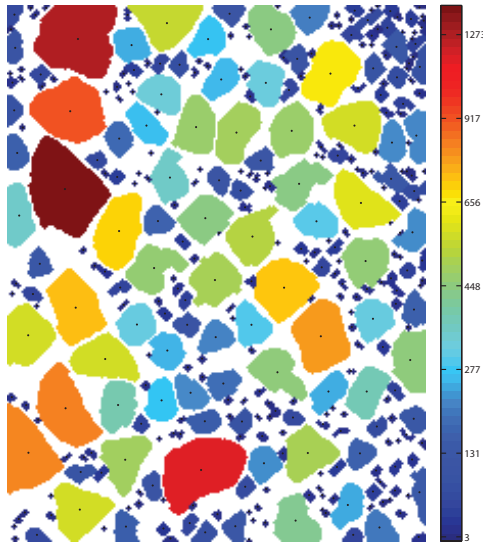

Figure 7.7: Labeled and colorized ice pieces.

7.1.4 Ice types classification and floe size distribution

According to [84], brash ice is considered as floating ice fragments no more than 2 m across. To distinguish brash ice from ice floes in our algorithm, we define a brash-ice threshold parameter (pixel number or area) that can be tuned for each application. The ice pieces with sizes larger than the threshold are considered to be ice floes, while smaller pieces are considered to be brash ice. The remaining ice pixels in Figure 7.3 are labeled as slush. The result is four layers of a sea-ice image (using Figure 7.1 as an example): ice floe (Figure 7.8(a)), brash ice (Figure 7.8(b)), slush (Figure 7.8(c)), and water (Figure 7.8(d)). Based on the four layers, a total of 154 ice floes and 189 brash ice pieces are identified from Figure 7.1. The coverage percentages are 60.52% ice floe, 3.34% brash ice, 16.03% slush, and 20.11% water. The ice floe size distribution histogram is shown in Figure 7.9.

The residue ice, which is the detected boundary pixels between the connected floes, was above considered as slush (since there often is a boundary layer of slush ice between two ice floes) and is included in Figure 7.8(c). However, the residue ice, as shown in Figure 7.10, can also be handled specifically according to the applied subsequent processing by the user.

7.2 Case Studies and Discussions

To test the validity of the algorithms, the aerial sea-ice images obtained from the remote sensing mission at Ny-Ålesund in early May 2011 are used as the case studies.

7.2.1 Simple sea-ice image case

Figure 7.11 shows an aerial image of the marginal ice zone without distortion. Since part of the ice pixels have intensity values close to water, both the "light ice" image and the "dark ice" image are used to obtain an accurate result. The procedure is as follows:

Step 1: Derive the "light ice" image and "dark ice" image from Figure 7.11 by the method mentioned in Section 7.1.1.

Step 2: Initialize the contours in both "light ice" image and "dark ice" image by the method mentioned in Section 7.1.2.

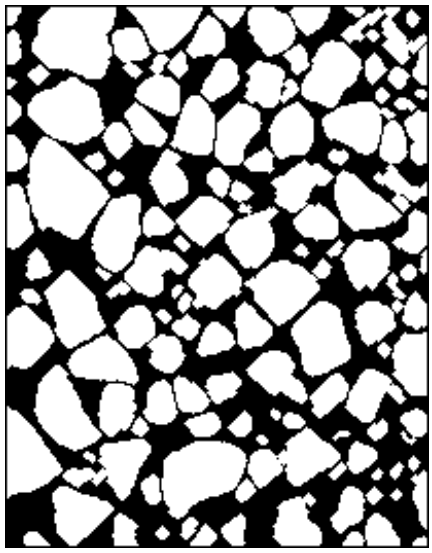

(a) Layer showing the “ice floes” of Figure 7.1

(b) Layer showing the “brash ice” of Figure 7.1

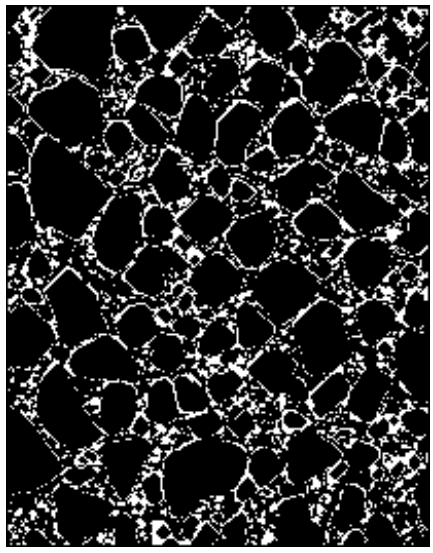

(c) Layer showing the “slush” of Figure 7.1

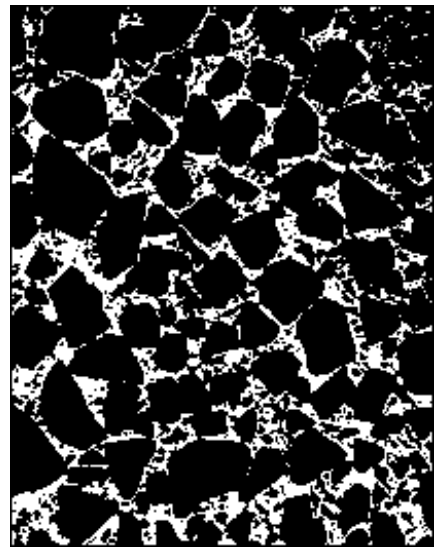

(d) Layer showing the “water” of Figure 7.1

Figure 7.8: Sea-ice image classification.

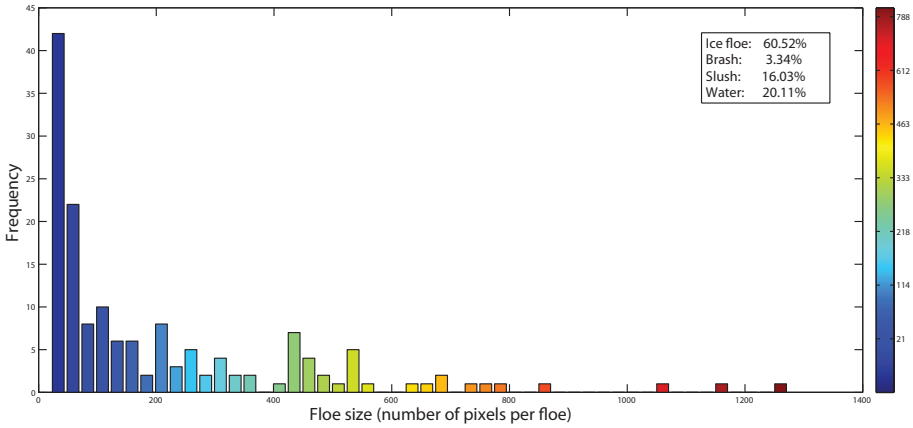

Figure 7.9: Floe size distribution histogram of Figure 7.8(a).

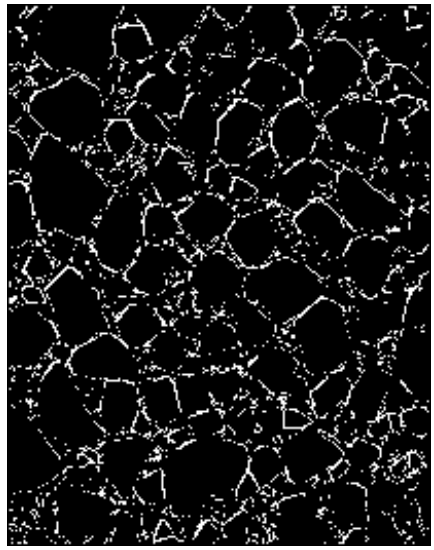

Figure 7.10: Residue ice (boundary pixels).

Step 3: Run the GVF snake algorithm on the initial contours to individually derive "light ice" segmentation and "dark ice" segmentation.

Step 4: Collect all the ice pieces in both "light ice" and "dark ice" segmentations, and perform the shape enhancement algorithm mentioned in Section 7.1.3.

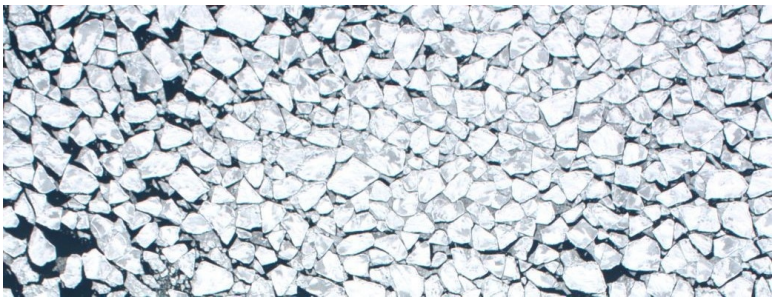

Figure 7.11: Aerial image of the marginal ice zone.

The resulting four layers of a sea-ice image and their coverage percentages are 76.73% ice floe shown in Figure 7.12(a), 0.46% brash ice shown in Figure 7.12(b), 9.05% slush shown in Figure 7.12(c), and 13.17% water shown in Figure 7.12(d). Based on the four layers, a total of 498 ice floes and 201 brash ice pieces are identified from Figure 7.11.

The ice floe (brash) size can be determined by the number of pixels in the identified floe (brash). The ice floe and brash ice are labeled in different colors based on their sizes with '$*$' and '.' at their centers, as shown in Figure 7.13. The resulting ice floe size distribution histogram is then shown in Figure 7.14.

7.2.2 Complex sea-ice image case

Section 7.2.1 gives a case study of processing the sea-ice image with uniform illumination and without any distortion problem. Most of the time, however, the aerial sea-ice images usually cover a large area, and the illumination of the images is often non-uniform. Besides this, perspective distortion may also exist in the image data because of the shooting angle of the camera. Perspective distortion usually exists when an aerial vehicle orbits the observation field. Both of these issues will affect the final ice floe identification and size distribution results. This case study illustrates how to apply the proposed algorithm to process the sea-ice image, shown in Figure 7.15, covering a large area with perspective distortion.

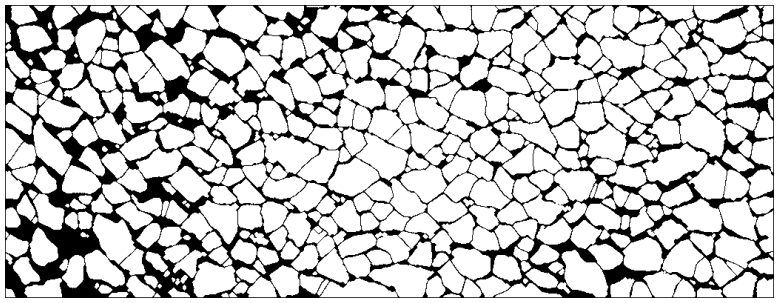

(a) Layer showing the “ice floes” of Figure 7.11

(b) Layer showing the “brash ice” of Figure 7.11

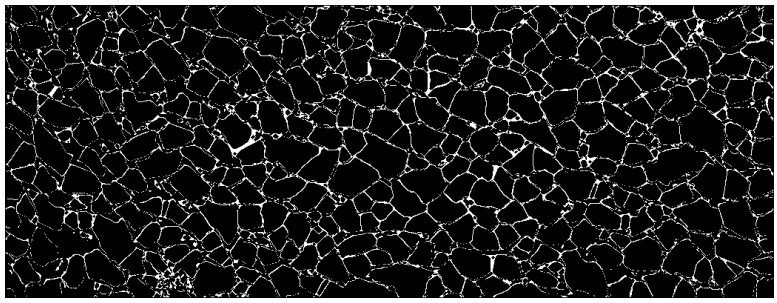

(c) Layer showing the “slush ice” of Figure 7.11

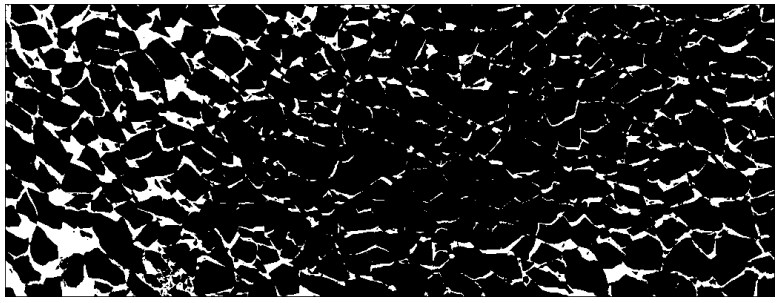

(d) Layer showing the “water” of Figure 7.11.

Figure 7.12: Identification result producing four layers for Figure 7.11.

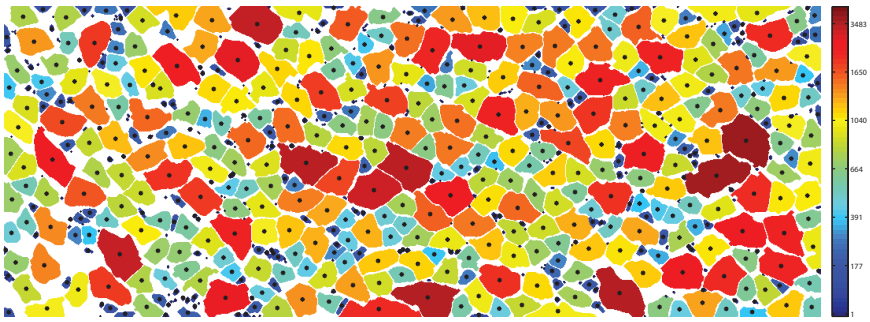

Figure 7.13: Floe and brash ice size distribution for Figure 7.11.

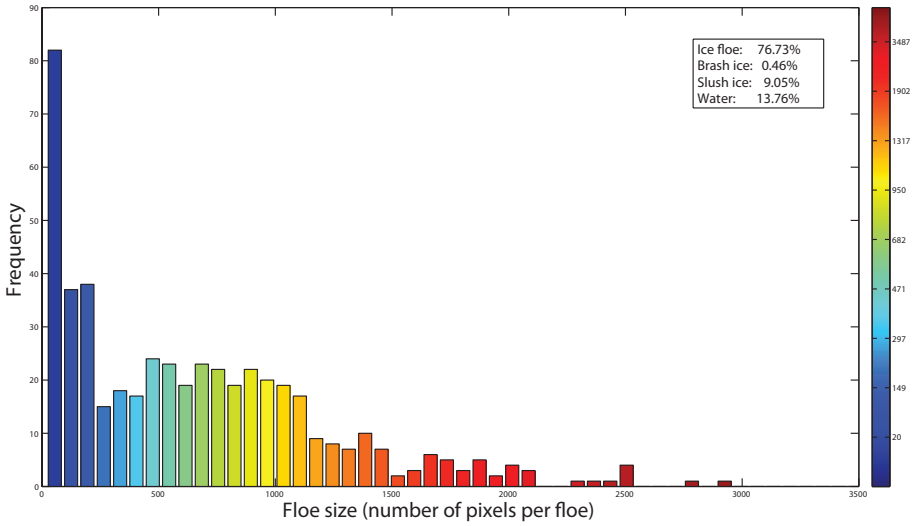

Figure 7.14: Floe size distribution histogram obtained from Figure 7.13.

Figure 7.15: Sea-ice image with perspective distortion.

Local processing

Some ice information can be lost when globally extracting "light ice" and "dark ice" from a sea-ice image when non-uniform illumination or shadow problems exist in the sea-ice image. Moreover, a sea-ice image typically contains multiple ice floes that crowd together, as shown in Figure 7.15, where parts of floe boundaries become weaker than others. As discussed in Chapter 6, the GVF capture range cannot represent an overall ice image and should be adjusted according to each sub-image. Therefore, processing the local sub-images of the large-area covered sea-ice image is recommended to obtain an accurate segmentation result (but at the expense of more processing time and manual intervention).

The image is first divided into smaller, overlapping regions such that each region can be analyzed locally [82]. The ice edge detection algorithm (Algorithm 4) is performed on each region to obtain a sub-segmentation image. Then we remove the overlapping part and superimpose the sub-segmentation images into their locations (by stitching the sub-segmentation images), resulting in an overall segmentation image. This procedure is shown in Figure 7.16.

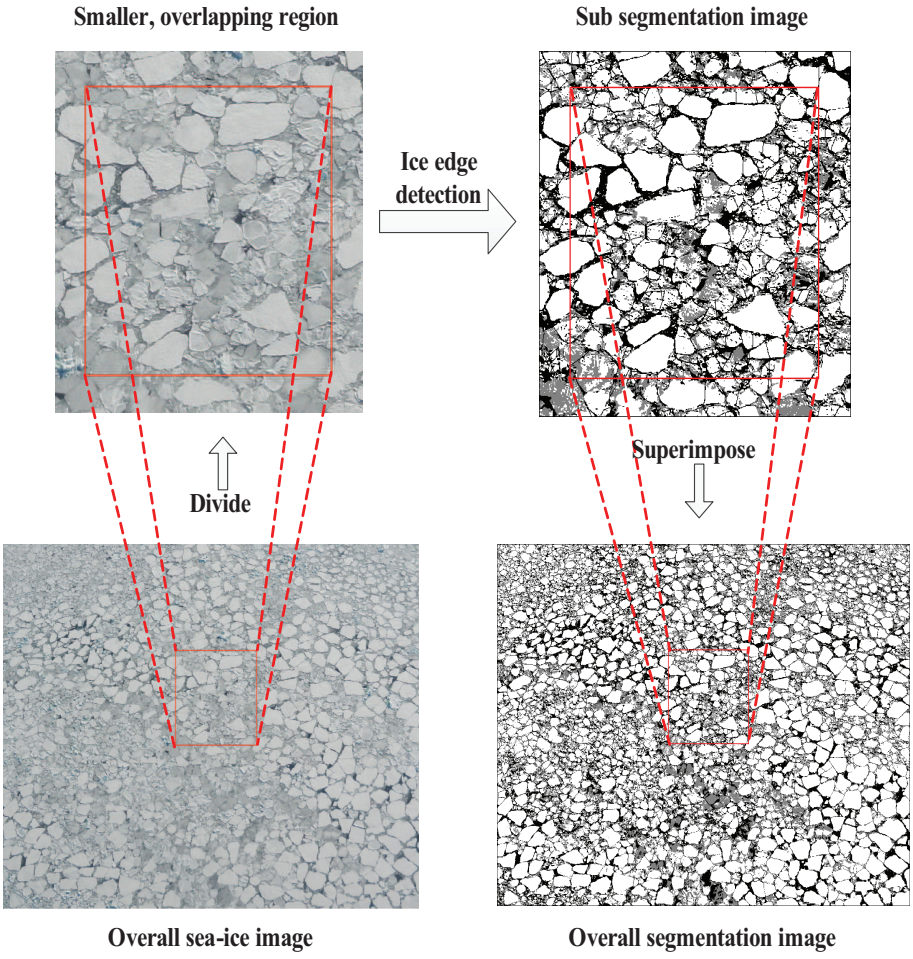

Figure 7.16: Local segmentation procedure. The white pixels are “light”ice pixels, and the gray pixels are “dark” ice pixels.

Geometric calibration

When the perspective distortion exists in the image data, the final identification result, as illustrated in Figure 7.17, is not adequate for the calculation of size distribution statistics. The ice floes in the far range of the image will seem smaller than those in the near range. This distortion will, therefore, induce errors in further analyses.

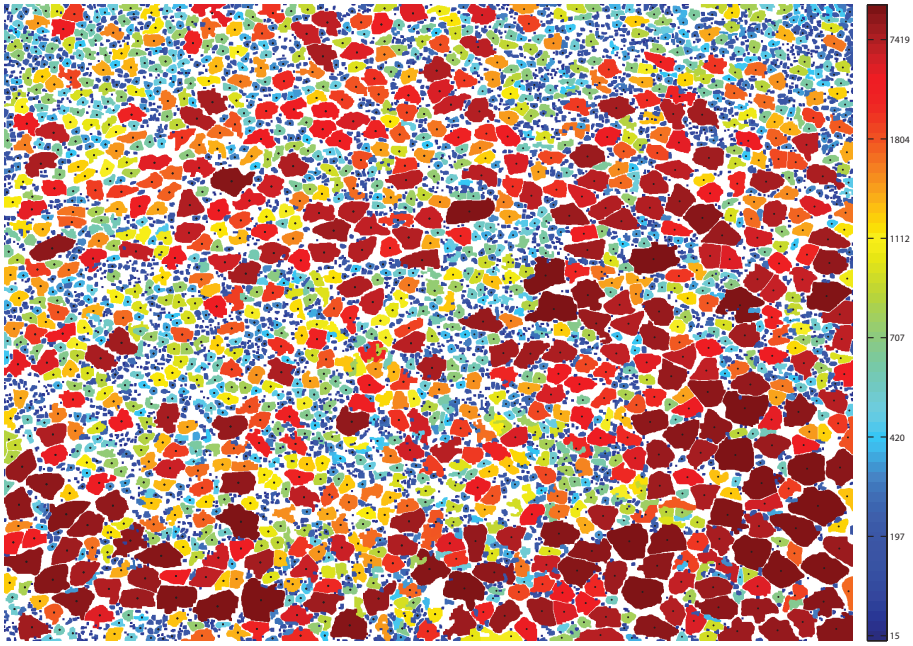

Figure 7.17: Ice floe and brash size distribution without orthorectification.

According to [37, 85] and Appendix A, the image can be orthorectified when the values of the shooting angle and the field of view of the camera are known, thus requiring a sensor to measure the camera's shooting angle. However, the actual parameters of the camera were not measured in this mission. Hence, to give an example to illustrate the overall algorithm, we have estimated the shooting angle to be approximately 20° and the field of view to be 46° (using the statistical similarities between the size distributions of near and far range of the image). Using this, we can orthorectify the overall segmentation image.

For non-ridged and non-shielded image, the geometric calibration should be performed on the segmented sea-ice image (after Algorithm 4) before sea-ice shape enhancement (Algorithm 5). Otherwise, the small ice floes located at

the far end of the image could be still considered to be brash ice. Furthermore, to reduce the visual distortion caused by the fractional zoom calculation, the image will be enlarged, and the total number of pixels will increase after orthorectification. The points between the pixels in the orthorectification coordinates that are mapped from the image coordinates must be interpolated. Each pixel holds quantized values that represent the color or gray level of the image at a particular point. Image interpolation [86], therefore, plays an important role in filling the values in those interpolated pixels by using known data to estimate values at unknown points.

The calibrated image, however, may be blurred because the values of the interpolated pixels are not the real values captured from the objects; as the number of interpolated pixels increase, the objects in the calibrated image become more blurry. The ice floe boundaries may become weaker or even be lost. The floe boundaries will become more difficult to detect. If the geometric calibration is performed before the ice floe identification, the proposed algorithm may fail to detect the ice floes in the far range of the image because of their blurred boundaries.

Results

After orthorectification, we enhance the shapes of all the ice pieces (Algorithm 5), and finally, we obtain the ice floe and brash ice size distribution, as shown in Figure 7.18. Brash ice is dark blue, smaller floes are light blue, and larger floes are red. Brash positions are not shown, while the floe positions are denoted using a black dot.

A total of 2511 ice floes and 2624 brash ice are identified from Figure 7.15. The coverage percentages are 65.98% ice floe, 5.03% brash ice, 17.52% slush, and 11.47% water. Instead of actual size of ice floe and brash (since we do not have the height above sea-level for the camera), the ice floe (brash) size is calculated by the number of pixels in the identified floe (brash). The relative ice floe distribution histogram is derived and shown in Figure 7.19, and the overall algorithm of the case study is concluded in Algorithm 6.

7.2.3 Sea-ice modeling

To modify the sea-ice floes and brash ice for the numerical simulation of the ice-structure interaction, the sea-ice floes were simplified by assigning the minimum-area-polygon to each floe, and the brash ice were reshaped by assigning the same-area-circle to each brash ice piece.

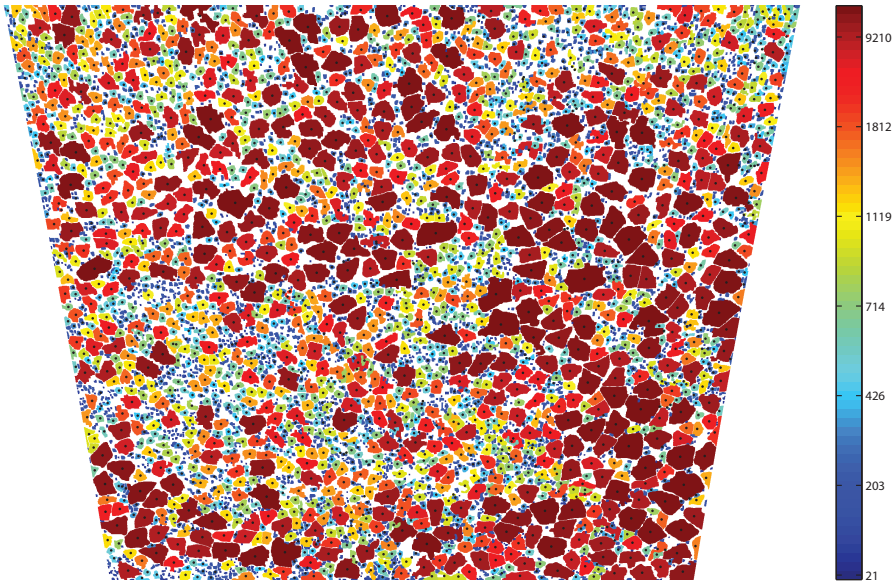

Figure 7.18: Ice floe and brash size distribution after orthorectification.

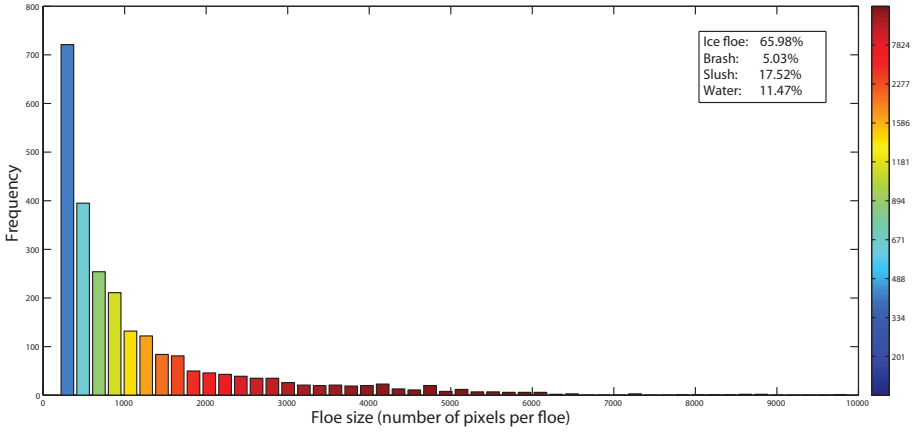

Figure 7.19: Ice floe size distribution histogram of Figure 7.18.

Algorithm 6 Overall sea-ice floe and brash identification algorithm.

Input: Sea-ice image.

Start algorithm:

$SUB \leftarrow$ sub-images divided from the input image.
for each sub-image $sub \in SUB$ **do**
  $seg \leftarrow$ ice edge detection (Algorithm 4) on sub.
end for
$SEG \leftarrow$ overall segmentation image with all seg stitched.
$SEG \leftarrow$ geometric calibrated SEG.
$ID \leftarrow$ sea-ice shape enhancement (Algorithm 5) on SEG.
$FLOE \leftarrow$ labeled regions in ID with large sizes.
$BRASH \leftarrow$ labeled regions in ID with small sizes.
$DISTRIBUTION \leftarrow$ floe size distribution.
return $FLOE, BRASH, DISTRIBUTION$.

Output: Segmented layers and Floe size distribution.

Figure 7.20 shows an example of sea-ice modeling for Figure 7.13. A close-up view of a few ice floes and brash ice in the middle of Figure 7.13 is given in Figure 7.21, with the blue boundaries of the polygons (circles) in Figure 7.20 superimposed on top of it. The centers of identified ice floes (brash ice) are marked with black '$*$ (.)', while the centers of polygonized floes (circularized brash ice) are marked with red '$+$ (.)'.

Figure 7.21 shows how the polygonization (circularization) modifies the floes (brash ice). It is obviously to see that, the polygonized floes will not be smaller than the actual identified floes, and may overlap with other floes and brash ice pieces. Therefore, similar to the model-ice floe modeling, the "overlap flags" of floe-floe and floe-brash were added to each polygonized floe besides its position, area, perimeter, and vertices. Moreover, the position, area, radius of each circularized brash ice, and the "overlap flags" of brash-brash and brash-floe were also registered in this modeling.

Figure 7.22(a) presents the colorized histogram of the polygonized floe size distribution of Figure 7.20(a), and Figure 7.22(b) subtracts the histograms of Figure 7.20(a) from Figure 7.13, so that we can see the "error differences" between the resulting floe size distributions.

The sea-ice modeling results have been used to generate a sea-ice field for numerical simulation of ice-structure interaction. Further applications are under consideration.

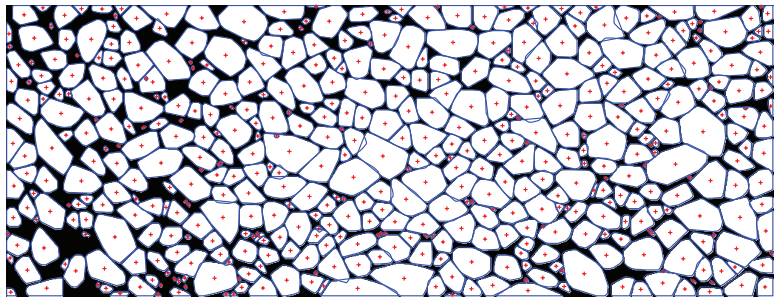

(a) Polygon fitting to ice floes in Figure 7.13.

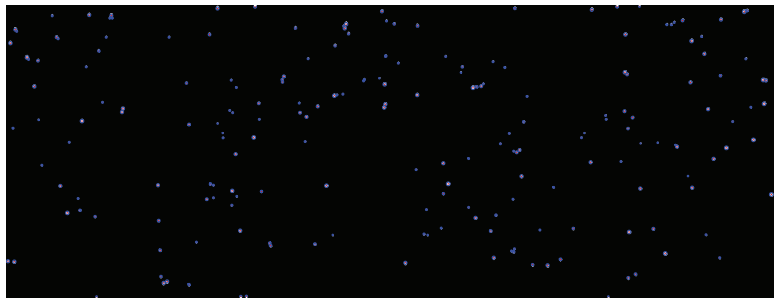

(b) Circle fitting to brash ice in Figure 7.13.

Figure 7.20: Sea-ice modeling for Figure 7.13.

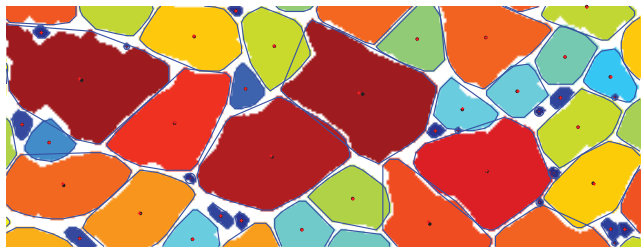

Figure 7.21: Comparison between identification and modification results. The blue closed curves are the boundaries of the modified floes (brash ice). The black '$*$ (.)' are the centers of identified ice floes (brash ice pieces), and the red '$+$ (.)' are the centers of polygonized floes (circularized brash ice).

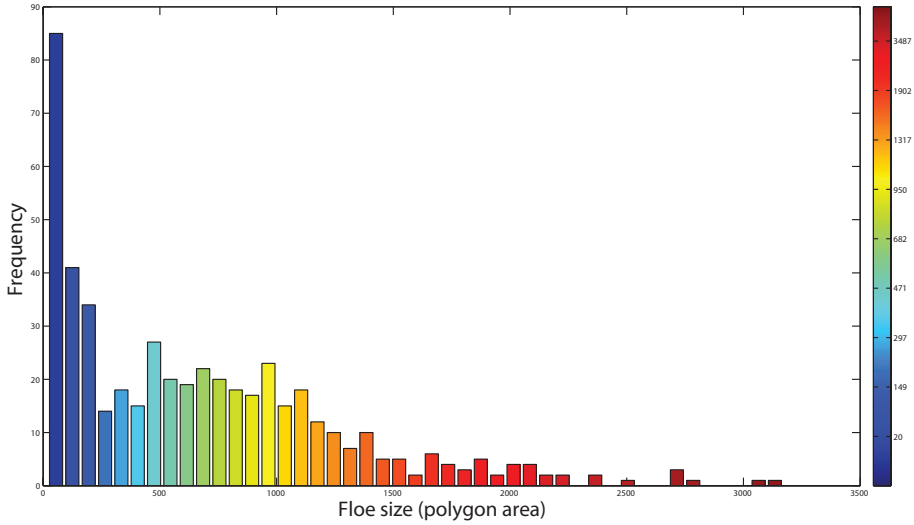

(a) Ice floe size distribution after polygon fitting.

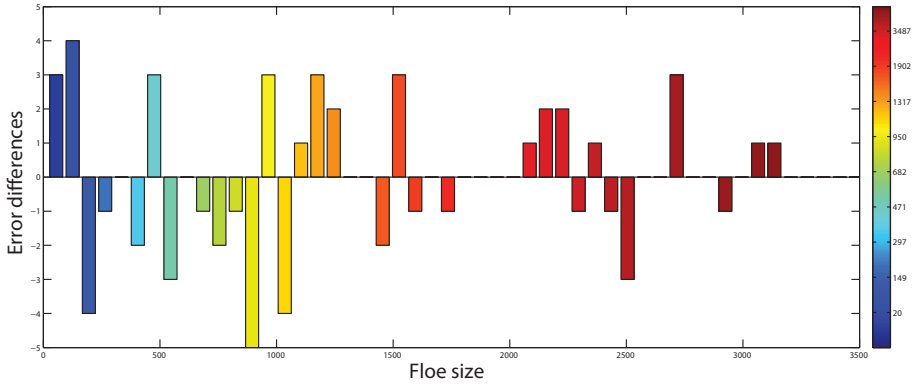

(b) Error differences between the resulting floe size distributions from Figure 7.14 and Figure 7.22(a).

Figure 7.22: Polygonized floe size distribution and its error differences.

7.3 Applications on Ice Engineering

7.3.1 Application 1: Processing of shipboard sea-ice image with fisheye distortion

The performance of KV Svalbard (a Norwegian Coast Guard icebreaker that operates in the Norwegian Arctic) in ice was studied by SAMCoT researchers, and a set of full-scale experimental data was collected in the Fram Strait from the 8th to the 18th of March in 2012. In this cruise, GoPro HD HERO2 cameras were employed and mounted out of the hatch to capture the ice condition in front of KV Svalbard's bow during the experiments. Figure 7.23(a) shows a sample image of the downward looking camera (the perspective distortion can be ignored), and Figure 7.23(b) is its corresponding segmentation result of both "light" and "dark" ice by using *Step 1 - 3* in Section 7.2.1.

The camera provided 170° field of view (FOV) angle [87] to give a wide view of the sea-ice at the expense of obtaining distorted images. The apparent effect of ice floes in the image is mapped around a sphere. The image magnification decreases with the distance from the optical axis. Besides the deformation, the size of the floe located in the center of the image is larger than it is closer to the image border. This affects the further ice floe size distribution results. To remove the fisheye distortion, the FOV angle is required by the calibration method, as illustrated in Appendix B.

The "wide" FOV angle was measured approximately to 119° (see Figure B.2 in Appendix B) by image width as opposed to the claimed 170°. The calibration should be performed after the detection of the floe boundaries (Section 7.1.2) since the calibrated image becomes enlarged and part of the image may be blurred. This may induce errors in the detection of the floe boundaries, as discussed in Section 7.2.2.

After that, we perform the sea-ice shape enhancement (Algorithm 5, *Step 4* in Section 7.2.1) to the calibrated image to obtain the final floe size distribution result, as shown in Figure 7.24. All floes in Figure 7.24 are actually found from Figure 7.23(a), although some large floes have odd shapes. This is because their distorted shapes in Figure 7.23(a) are corrected by the fisheye calibration algorithm. About 29 ice floes and 9 brash ice pieces are found, and the ice concentration is calculated as 74.17%.

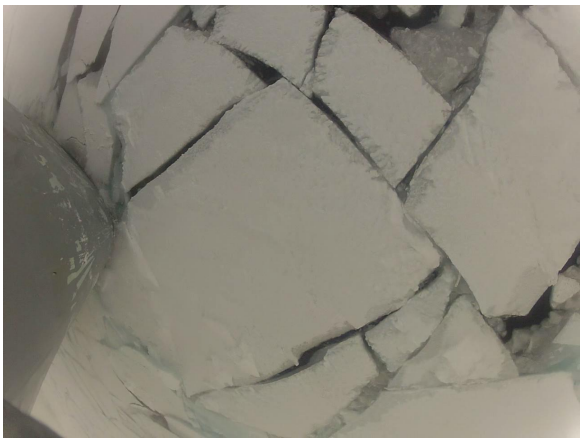

(a) Shipboard sea-ice image with fisheye distortion.

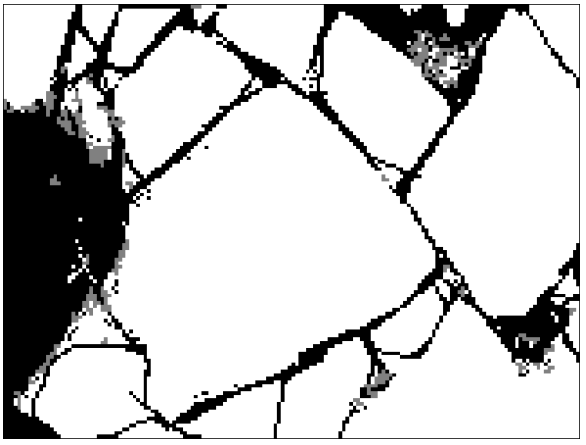

(b) Segmentation result of (a). The white pixels are "light ice" pixels, and the gray pixels are "dark ice pixels.

Figure 7.23: Shipboard sea-ice image with fisheye distortion and its segmentation result.

Figure 7.24: Floe and brash ice size distribution of Figure 7.23(b).

7.3.2 Application 2: The 360-degree camera system and ice image processing

A 360-degree camera system was used in the Oden Arctic Technology Research Cruise (OATRC 2013) to monitor the ice condition around the vessel. This system consisted of two 360° Arecont Vision 20365DN-HB video camera units, a 20 megapixel camera unit that includes a set of four independent cameras (four objectives) with heater and blower housing option to provide normal camera functioning in cold and wet conditions. The system was installed on the helicopter deck of icebreaker Oden, allowing the construction of 360° panorama images of ice conditions around the vessel [88].

In order to stitch together the individual camera images into a single panorama, [88] used the commercial software PTGui Pro v9.1.8. A set of pictures with clearly visible ice structures was selected and stitched together manually to create the template. Based on this template, batches of images may then be automatically stitched together. To estimate the ice concentration around the icebreaker based on the panorama images, rectilinear (flat) projection that projects the image onto a plane is chosen to remove the geometric distortion.

In OATRC 2013, a pushing test was conducted, where the icebreaker slowly pushed the ice floes aside, instead of simply breaking them. An advantage of pushing an ice floe away is that a larger wake region can be created behind the floe, and less ice breaking is needed. Figure 7.25 shows a resulting panorama image from the pushing test. When applying the algorithms to these panorama images, one image per minute was found sufficient. Each image was then fed to the program for processing.

Figure 7.25: 360 degree panorama image.

Significant distortion exists in the resulting panorama images as a result of camera vibration and influence of the pitch and roll of the icebreaker during maneuvers. The images are stitched from a single template created from a particularly clear set of images. The resulting images are also highly blurred because of the occasional icing/fogging on the camera dome due to insufficient heating, as shown in Figure 7.25. The ice pixel detection by Otsu thresholding method is insufficient since the occasional icing/fogging parts are considered as ice pixels because of their high intensity. This will increase the manual work for the local processing.

Instead, the k-means method is used and divides the image into three clusters. Only the cluster with the highest average intensity value is considered to be ice, and the other clusters are considered to be water. Then, manual local

processing is done using the methods in Section 7.1.1 and 7.1.2 to identify all the missing ice and floe boundaries, resulting in a segmented image. After performing the shape enhancement method (Section 7.1.3) to the segmented image, 128 ice floes and brash ice pieces are identified. The ice concentration is calculated to 41.79%, as presented in Figure 7.26.

Figure 7.26: Identified ice floe distribution of Figure 7.25.

By processing the sequence of panorama images obtained from the pushing test experiment, the ice concentration was calculated as a function of time and presented in Figure 7.27.

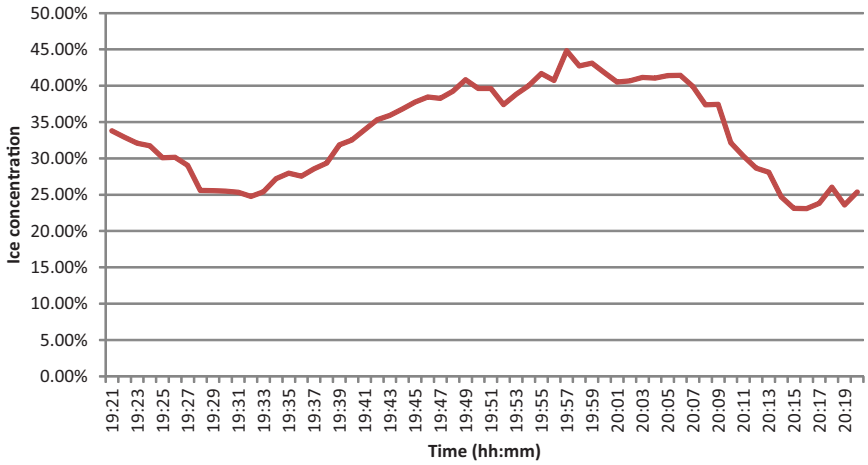

Figure 7.27: Time-varying ice concentration of pushing test.

Chapter 8

Conclusion

This thesis is about image processing for ice observations. Various image techniques have been developed and applied to the collected ice images for analyses to give some results applicable to ice engineering and ice management.

The ice concentration from a digital visual ice image is defined in Chapter 1 and indicates that the extraction of ice pixels from ice image is required for calculating ice concentration. To accomplish this, Chapter 2 first adopts the Otsu thresholding to divide the ice image into "ice region" and "water region". This works well in model-ice images and part of sea-ice images when all the ice pixels are significantly brighter than water. However, the ice pixels with the intensity values close to water cannot be detected by this method when the sea-ice images contain brash ice, slush, or the ice submerged in the water. Therefore, the k-means clustering method is used to detect more ice pixels from such images by dividing the image into three or more clusters, where the cluster with the lowest average intensity value is considered as "water region" while the others are considered as "ice regions".

Ice boundaries are important for obtaining the ice floe size distribution from ice images. Two common edge detection methods - the derivative edge detection and morphology edge detection - are introduced in Chapter 3 to try to detect ice boundaries. Compared with the morphology method, the derivative method is more sensitive to the differences between regions, and more weak-boundaries between the connected floes are found. The downside of this method, on the other hand, is that it will produce more non-closed boundaries, which are unable to separate the connected floes. Instead, the morphology method can close the floe boundaries and break the thin connections between floes, which is beneficial for the separation of the connected floes. However, only weakly connected ice floes can be separated by the morphology method.

Neither method can separate strongly connected ice floes, and the connected floes will be considered as a big floe.

The separation of seemingly connected floes into individual ones challenges ice floe size distribution analysis due to their weak boundaries. To solve this problem, the watershed transform, which is the state-of-art method for separating connected objects, is adopted in Chapter 4. Due to the over-segmentation caused by the watershed transform, each ice floe is first assumed to have a convex boundary. Then, the chain code is used to find the concave corners of floe boundaries, and a neighboring-region merging algorithm based on those detected concave corners is proposed to automatically remove the over-segmentation. However, the watershed-based method should only be used for separating the connected ice floe with invisible junctions because the actual boundary information is lost when using the watershed transform.

To operate on the actual ice floe boundaries, Chapter 5 introduces the gradient vectorfFlow (GVF) snake algorithm, which has a good ability for detecting weak boundaries and identifying individual ice floes. To evolve the GVF snake correctly for ice floe boundary detection, a proper initial contour is required. Chapter 5 shows that the initial contour close to the actual floe boundary, located inside the floe and centered as close as possible to the ice floe center, is most effective. To accomplish the requirements of the initial contour without manual interaction, an automatic contour initialization algorithm based on the distance transform and its local maxima is proposed. After initializing the contours, the GVF snake algorithm is run on each contour to identify the floe boundary. Superimposing all the boundaries over the binarized ice image then results in separation of the connected ice floes. Furthermore, to effectively enhance the shape of the ice floe, the ice shape enhancement algorithm is performed after segmentation.

When ice floes crowd together, some connected ice floes may not be separated by the method proposed in Chapter 5 because of the loss of the seeds found by the proposed contour initialization algorithm. Additional efforts are required for such issues. For the model-ice images, the ice floes are modeled as square shapes with predefined side lengths. Chapter 6 proposes three criteria based on the characteristics of the model-ice floes. The algorithm will determine whether it is necessary to initialize the contours and conduct a second segmentation after each segmentation step. The floes that do not satisfy any of these criteria and new seeds will be found. Then we initialize new contours based on the new seeds and perform another round of segmentations.

For the sea-ice images where the ice are of various types, sizes, and shapes, Chapter 7 first derives a "light ice" image and a "dark ice" image based on the thresholding and k-means clustering methods. Then, the contours are ini-

tialized in both the "light ice" image and the "dark ice" image, and the GVF snake algorithm is run on the initial contours to individually derive "light ice" segmentation and "dark ice" segmentation. Finally, the ice shape enhancement is performed on the collection of all the segmented ice pieces from both "light ice" and "dark ice" segmentations, resulting in the sea-ice floe identification.

Our experiments on both model- and sea-ice images show that the proposed algorithms are effective for identifying individual ice floes. The colorized ice floe maps and the corresponding ice floe size distribution histograms are obtained thereafter. Besides, Chapter 6 rectangularizes the identified model-ice floes for the validation of a numerical simulation and monitors the maximum floe size entering the protected vessel from a physical ice management operation. Chapter 7 distinguishes the different types of sea-ice and, based on the identification result, divides the image into four layers: ice floes, brash ice, slush, and water. Chapter 7 also draws on case studies to illustrate a procedure for processing the sea-ice image covering a large area with geometric distortion, and modifies identified sea-ice floes and brash ice for the numerical simulation.

Future Work

To calculate ice concentration, the Otsu thresholding and k-means clustering methods were adopted in this thesis to divide an image into two or more classes in a mandatory manner. This will fail in the boundary conditions when ice concentration is 0% or 100%, which have to be dealt with as particular cases. Furthermore, these two methods do not include detailed ice physics except the grayscale value of the image. Therefore, the "learning-based object detection", such as machine learning (e.g., support vector machine, deep learning, etc.) [89] and texture feature descriptors [63], could be a future research direction.

The GVF-snake based ice floe identification algorithm proposed in this thesis performs well in ice floe identification and presentation of the floe size distribution of model-ice images and marginal ice zone images. However, manual intervention may be necessary for processing other sea-ice images. The main limitation of this method is that the parameters for the GVF field are, unfortunately, tuned manually, which is a limitation to the applicability of the algorithm in real-world situations, especially when a large number of images must be analyzed. As of now, no explicit performance criterion exist for when reasonable identification is achieved other than the operator's own judgment, and it is, therefore, very difficult to optimize the value of the parameters. Thus, further sensitivity studies are needed to focus on the automatic optimization of

the critical parameters for a given image or image fragment. This is a topic of ongoing research, with the expectation of more results and better information of sea-ice from visual images by the further development of these image processing methods for real-time applications.

Statistical analysis on the floe size distribution is another topic of ongoing research. The cumulative distribution can be calculated following some probabilistic models and compared with previous studies [26]. The applicability of the proposed methods for generating a statistical data set for ice engineering should be studied.

Appendix A

Geometric Orthorectification

The location of any object in the image is a function of the spatial orientation of the camera in relation to ground topography. Figure A.1 illustrates the relationship between the image coordinates and the orthorectification coordinates.

The image coordinates lay in the focal plane and are denoted with small letters (x, y). The orthorectification plane coordinates are parallel to the ground and are denoted with capital letters (X, Y). The optic center of the camera is S. The camera $nadirline$ intersects the orthorectification plane at the nadir T. The optic axis is perpendicular to the focal plane and intersects the center of the focal plane at principal point r, forming the shooting angle φ with the vertical nadir line. The optic axis extends to the orthorectification plane at point R. The principal line passes through point R (r) and the image border at O (or o), and it bisects the orthorectification (focal) plane. The point O (or o) acts as the origin for the image coordinate system, with the y-axis as the principal line, and the origin for the orthorectification coordinate system with the principal line in the orthorectification plane defining the positive Y-axis. $p(x, y)$ is any point on the image plane. $P(X, Y)$ is the corresponding point on the orthorectification plane.

From Figure A.1, we obtain:

$$TO = SO \sin(\varphi - \theta) = f \sec\theta \sin(\varphi - \theta) \tag{A.1}$$

$$TQ = ST \tan(\varphi + \vec{\alpha}) = f \sec\theta \cos(\varphi - \theta) \tan(\varphi + \vec{\alpha}) \tag{A.2}$$

$$SQ = ST \sec(\varphi + \vec{\alpha}) = f \sec\theta \cos(\varphi - \theta) \sec(\varphi + \vec{\alpha}) \tag{A.3}$$

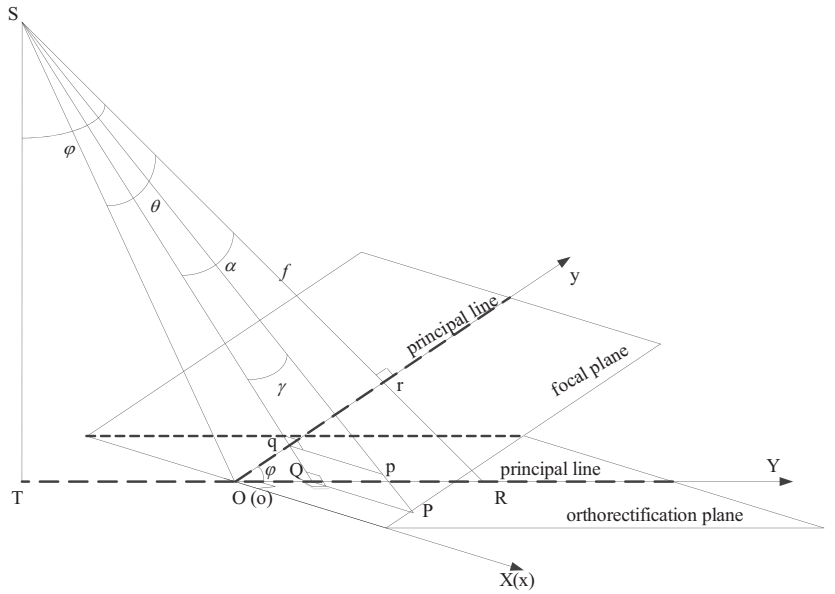

Figure A.1: Geometric orthorectification.

$$\vec{\gamma} = \arctan(qp/Sq) = \arctan\frac{qp\cos\vec{\alpha}}{f}, \tag{A.4}$$

where θ is half of the len's vertical field of view angle, f is the focal length, and $\vec{\alpha} = \arctan(\vec{qr}/f)$.

According to equations (A.1)-(A.4), we derive

$$\begin{aligned} OQ &= TQ - TO \\ &= f\sec\theta[\cos(\varphi-\theta)\tan(\varphi+\arctan\frac{\vec{qr}}{f}) - \sin(\varphi-\theta)] \end{aligned} \tag{A.5}$$

$$\begin{aligned} QP = SQ\tan\gamma &= qp\frac{\cos\vec{\alpha}\cos(\varphi-\theta)}{\cos\theta\cos(\varphi+\vec{\alpha})} \\ &= qp\frac{f}{\sqrt{f^2+\vec{qr}^2}}\frac{\cos(\varphi-\theta)}{\cos\theta\cos(\varphi+\arctan\frac{\vec{qr}}{f})}. \end{aligned} \tag{A.6}$$

A digital image is a numeric representation of a two-dimensional picture and is composed of pixels that are the smallest individual elements of the image. We assume that the pixel magnification of the image is μ, yielding

$$\begin{cases} oq = y\cdot\mu \\ qp = x\cdot\mu \end{cases} \tag{A.7}$$

$$\begin{cases} OQ = Y \cdot \mu \\ QP = X \cdot \mu \end{cases} \tag{A.8}$$

Therefore,

$$\vec{qr} = \vec{(}oq) - \vec{(}or) = (y - \frac{n_y}{2}) \cdot \mu \tag{A.9}$$

where n_y is the number of pixels in image length. Instead of working from a $1:1$ positive, we counted image pixels on a computer screen. Hence, the apparent focal length of the image is altered by

$$f^{'} = \frac{y_e}{\tan\theta} = \frac{\mu \cdot n_y/2}{\tan\theta}, \tag{A.10}$$

where y_e is the half-length of the image. Substituting Equations A.7 - A.10 into Equations A.5 and A.6, the location of any point, $P(X, Y)$, in the orthorectification coordinates can be determined from its image coordinates, $p(x, y)$, by:

$$\begin{cases} Y = \frac{n_y}{2} \csc\theta \{\cos(\varphi - \theta) \tan[\varphi + \arctan(\frac{y - n_y/2}{n_y/2} \tan\theta)] \\ \qquad - \sin(\varphi - \theta)\} \\ X = x \cdot \frac{\frac{n_y}{2} \csc\theta \cos(\varphi - \theta) \sec[\varphi + \arctan(\frac{y - n_y/2}{n_y/2} \tan\theta)]}{\sqrt{(\frac{n_y/2}{\tan\theta})^2 + (y - \frac{n_y}{2})^2}}, \end{cases} \tag{A.11}$$

and the image is orthorectified.

From Equation A.11, we can find that, although μ varies with the magnification ratio of the image, the relationship between different coordinates will not change. This is because the influence of μ is counteracted based on Equations A.7 - A.10. Consequently, the relationship between the image coordinates and the orthorectification coordinates is a function of the shooting angle φ and the camera's (vertical) field of view 2θ. An example of orthorectification result is shown in Figure A.2.

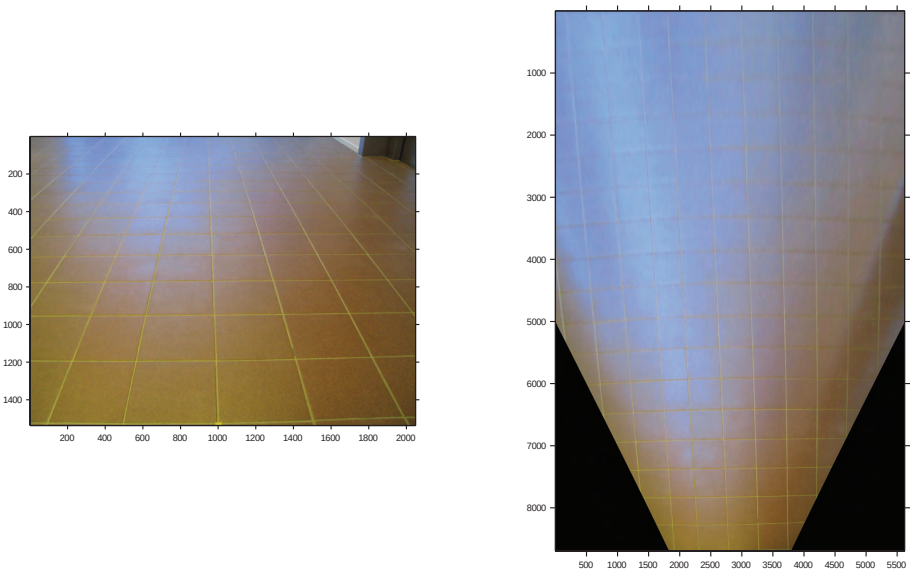

Figure A.2: Orthorectification result.

Appendix B

Fisheye Calibration

The location of any object in the image is a function of the field of view (FOV) angle of the camera in relation to its calibrated flat surface. Figure B.1 illustrates the mapping between fisheye image coordinates and the corresponding calibration coordinates.

The fisheye image coordinates, denoted with small letters (x, y), is located at the bottom of the fisheye sphere and is perpendicular to the Z-axis (the optical axis of the lens). The calibration coordinates, denoted with capital letters (X, Y), are on the top of the fisheye sphere parallel to the image coordinates. The center of the fisheye image, 'o', located in the Z-axis, acts as the origin of the image coordinates. The intersection point O of the calibration plane and Z-axis acts as the origin of the calibration coordinates. φ is half the lens FOV angle, which is known. For any point, $p(x, y)$, on the image plane and its corresponding point, $P(X, Y)$, on the calibration plane, the radial distance, $|\vec{OP}|$, in the distorted fisheye image plane, $|\vec{op}|$, is equivalent to the length of the arc segment, r, between the Z-axis and P_0, which is the intersection point of the projection ray of the point P and the fisheye sphere. Therefore,

$$\begin{aligned} |\vec{op}| = r &= R \cdot \alpha \\ &= R \cdot \arctan \frac{|\vec{OP}|}{R}, \end{aligned} \tag{B.1}$$

where R is the radius of the fisheye sphere, obtained by:

$$R = \frac{r_{max}}{\varphi} = \frac{r_m \cdot \mu}{\varphi}, \tag{B.2}$$

and r_{max} is half the capture range of the fisheye image in length, r_m is the pixel number in maximum semidiameter, obtained by counting half the number of

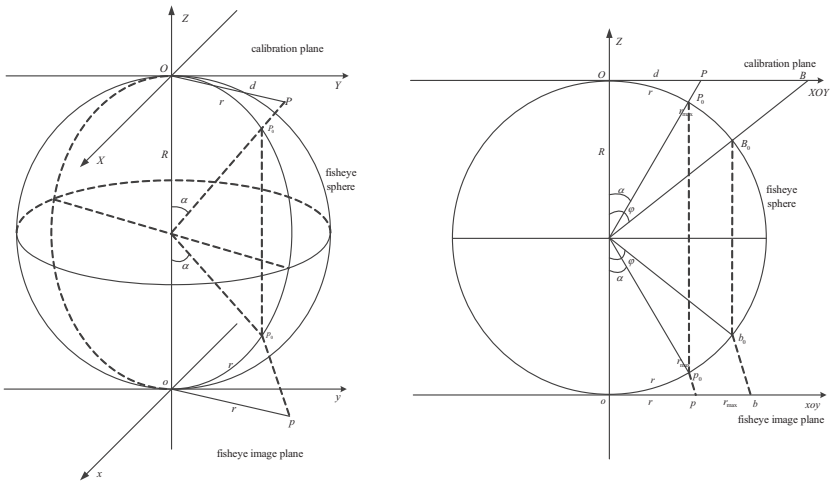

(a) 3-D spherical perspective. (b) 2-D spherical perspective.

Figure B.1: Fisheye calibration.

pixels in the image length, and μ is the pixel magnification of the image. From Figure B.1(a), we also find that

$$|\vec{op}| = \sqrt{x^2 + y^2} \cdot \mu \tag{B.3}$$

$$|\vec{OP}| = \sqrt{X^2 + Y^2} \cdot \mu \tag{B.4}$$

$$\frac{x}{y} = \frac{X}{Y} \tag{B.5}$$

Substituting Equations B.2 - B.5 into B.1, the location of any point, $P(X, Y)$, in the calibration coordinates can be determined from its fisheye image coordinates, $p(x, y)$, by:

$$X = \frac{x}{\sqrt{x^2 + y^2}} \cdot \frac{r_m \tan \frac{\varphi\sqrt{x^2+y^2}}{r_m}}{\varphi}, \tag{B.6}$$

$$Y = \frac{y}{\sqrt{x^2 + y^2}} \cdot \frac{r_m \tan \frac{\varphi\sqrt{x^2+y^2}}{r_m}}{\varphi}.$$

From Equation B.6, we find that the relationship between the fisheye image coordinates and its calibration coordinates only depend on the camera's FOV angle 2φ. The magnification μ will not affect the relationship since it is counteracted based on Equations B.2 - B.4. The calibration result is illustrated in Figure B.2.

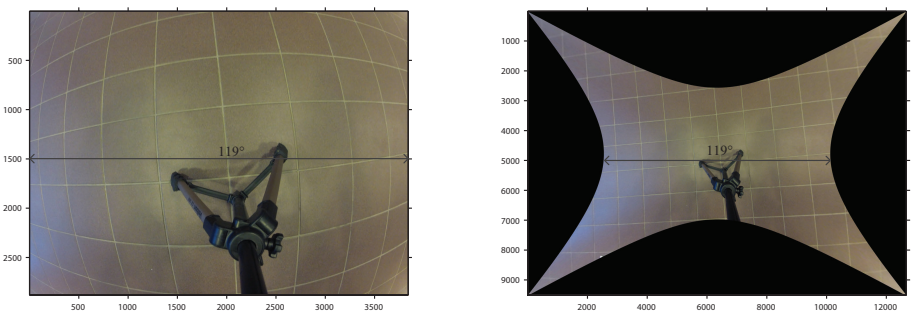

Figure B.2: Fisheye calibration result.

Bibliography

[1] K. J. Bird, *Circum-Arctic resource appraisal: Estimates of undiscovered oil and gas north of the Arctic Circle*. US Department of the Interior, US Geological Survey, 2008.

[2] A. Gürtner, *Experimental and numerical investigations of ice-structure interaction*. PhD thesis, Norwegian University of Science and Technology, 2009.

[3] A. Keinonen, H. Wells, P. Dunderdale, R. Pilkington, G. Miller, and A. Brovin, "Dynamic positioning operation in ice, offshore sakhalin, may-june 1999," in *The Proceedings of the International Offshore and Polar Engineering Conference*, vol. 1, pp. 683–690, International Society of Offshore and Polar Engineers, 2000.

[4] K. Moran, J. Backman, and J. W. Farrell, "Deepwater drilling in the arctic ocean's permanent sea ice," in *Proc. IODP| Volume*, vol. 302, p. 2, 2006.

[5] D. T. Nguyen, A. Sørbø, and A. Soerensen, "Modelling and control for dynamic positioned vessels in level ice," in *Manoeuvring and Control of Marine Craft*, pp. 229–236, 2009.

[6] K. R. Simmonds, *The International Maritime Organization*. Simmonds & Hill Pub, 1994.

[7] T. I. Fossen, *Handbook of marine craft hydrodynamics and motion control*. John Wiley & Sons, 2011.

[8] A. J. Sørensen, "Marine control systems propulsion and motion control of ships and ocean structures lecture notes," 2011.

[9] G. Wilkman, R.-A. Suojanen, S. Saarinen, T. Mattsson, and T. Leiviskä, "Dp in ice conditions' challenges and opportunities," in *Dynamic positioning conference, Houston*, 2009.

[10] R. Skjetne, L. Imsland, and S. Løset, "The arctic dp research project: Effective stationkeeping in ice," *Modeling, Identification and Control*, vol. 35, no. 4, p. 191, 2014.

[11] A. Keinonen, "Ice management for ice offshore operations," in *Proceedings of the Offshore Technology Conference. Houston, TX*, 2008.

[12] R. Skjetne, L. Imsland, and S. Løset, "The Arctic DP research project: Effective stationkeeping in ice," *Modeling, Identification and Control*, vol. 35, no. 4, pp. 191–210, 2014.

[13] K. Eik, "Review of experiences within ice and iceberg management," *Journal of Navigation*, vol. 61, no. 04, pp. 557–572, 2008.

[14] J. Haugen, *Autonomous Aerial Ice Observation*. PhD thesis, Norwegian University of Science and Technology, 2014.

[15] A. Makrygiannis, "Design and simulation of an ice-capable dp system," Master's thesis, Norwegian University of Science and Technology, The address of the publisher, 2012.

[16] Ø. K. Kjerstad, I. Metrikin, S. Løset, and R. Skjetne, "Experimental and phenomenological investigation of dynamic positioning in managed ice," *Cold Regions Science and Technology*, vol. 111, pp. 67–79, 2015.

[17] I. Metrikin, *Experimental and Numerical Investigations of Dynamic Positions in Discontinuous Ice*. PhD thesis, Norwegian University of Science and Technology, 2014.

[18] G. Timco, B. Gorman, and J. Falkingham, "Scoping study: Ice information requirements for marine transportation of natural gas from the high arctic," tech. rep., NRC Report CHC-TR-020, Ottawa, Ont., Canada, 2005.

[19] K. Eik and S. Løset, "Specifications for a subsurface ice intelligence system," in *ASME 2009 28th International Conference on Ocean, Offshore and Arctic Engineering*, pp. 103–109, American Society of Mechanical Engineers, 2009.

[20] U. Jørgensen and R. Skjetne, "Online reconstruction of drifting underwater ice topography: The 2d case," *Asian Journal of Control*, 2016.

[21] J. Haugen, L. Imsland, S. Løset, and R. Skjetne, "Ice observer system for ice management operations," in *Proceeding of the 21st International Ocean and Polar Engineering Conference*, (Maui, Hawaii, USA), 2011.

[22] C. Gignac, Y. Gauthier, J.-S. Bédard, M. Bernier, and D. Clausi, "High resolution radarsat-2 SAR data for sea-ice classification in the neighbour-

hood of Nunavik's marine infrastructures," in *Proceedings of the 21st International Conference on Port and Ocean Engineering under Arctic Conditions*, (Montréal, Canada), 2011.

[23] A. V. Bogdanov, S. Sandven, O. M. Johannessen, V. Y. Alexandrov, and L. P. Bobylev, "Multisensor approach to automated classification of sea ice image data," *IEEE Transactions on Geoscience and Remote Sensing*, vol. 43, no. 7, pp. 1648–1664, 2005.

[24] L.-K. Soh, C. Tsatsoulis, D. Gineris, and C. Bertoia, "ARKTOS: An intelligent system for SAR sea ice image classification," *IEEE Transactions on Geoscience and Remote Sensing*, vol. 42, no. 1, pp. 229–248, 2004.

[25] D. Haverkamp and C. Tsatsoulis, "Information fusion for estimation of summer MIZ ice concentration from SAR imagery," *IEEE Transactions onGeoscience and Remote Sensing*, vol. 37, no. 3, pp. 1278–1291, 1999.

[26] D. Rothrock and A. Thorndike, "Measuring the sea ice floe size distribution," *Journal of Geophysical Research: Oceans (1978–2012)*, vol. 89, no. C4, pp. 6477–6486, 1984.

[27] T. Toyota and H. Enomoto, "Analysis of sea ice floes in the sea of okhotsk using ADEOS/AVNIR images," in *Proceedings of the 16th IAHR International Symposium on Ice, Dunedin, New Zealand*, pp. 211–217, 2002.

[28] S. Ji, H. Li, A. Wang, and Q. Yue, "Digital image techniques of sea ice field observation in the bohai sea," in *POAC11-077, Proceedings of the 21st International Conference on Port and Ocean Engineering under Arctic Conditions (POAC'11), Montréal, Canada*, 2011.

[29] J. Millan and J. Wang, "Ice force modeling for DP control systems," in *Proceedings of the Dynamic Positioning Conference*, (Houston, Texas, USA), 2011.

[30] Q. Zhang, R. Skjetne, S. Løset, and A. Marchenko, "Digital image processing for sea ice observations in support to Arctic DP operations," in *ASME 2012 31st International Conference on Ocean, Offshore and Arctic Engineering*, pp. 555–561, American Society of Mechanical Engineers, 2012.

[31] S. van der Werff, A. Haase, R. Huijsmans, and Q. Zhang, "Influence of the ice concentration on the ice loads on the hull of a ship in a managed ice field," in *ASME 2012 31st International Conference on Ocean, Offshore and Arctic Engineering*, pp. 563–569, American Society of Mechanical Engineers, 2012.

[32] G. Comfort, S. Singh, and D. Spencer, "Evaluation of ice model test data for moored structures," tech. rep., PERD/CHC, 1999.

[33] Common terms used in sea ice research, accessed 2015-03-09. `http://seaiceatlas.snap.uaf.edu/glossary`.

[34] W. M. Organization, *WMO Sea-ice Nomenclature: Terminology, Codes, Illustrated Glossary and Symbols*. No. 259, Secretariat of the World Meteorological Organization Geneva, 1970.

[35] S. Løset, K. N. Shkhinek, O. T. Gudmestad, and K. V. Høyland, *Actions from Ice on Arctic Offshore and Coastal Structures*. St. Petersburg, Russia, 2006.

[36] Sea ice types, accessed 2015-03-09. `http://www.antarctica.gov.au/about-antarctica/environment/icebergs-and-ice/sea-ice`.

[37] P. Lu and Z. Li, "A method of obtaining ice concentration and floe size from shipboard oblique sea ice images," *IEEE Transactions on Geoscience and Remote Sensing*, vol. 48, no. 7, pp. 2771–2780, 2010.

[38] A. Keinonen and I. Robbins, "Icebreaker characteristics synthesis, icebreaker performance models, seakeeping, icebreaker escort," *Icebreaker Escort Model User's Guide: Report prepared for Transport Development Centre Canada (TP12812E)*, vol. 3, p. 49, 1998.

[39] A. Palmer and K. Croasdale, *Arctic Offshore Enginnering*. World Scientific Publishing Company, 2012.

[40] J. S. Brown, E. H. Martin, and A. Keinonen, "Ice management numerical modeling and modern data sources," in *The International Conference and Exhibition on Performance of Ships and Structures in Ice (ICETECH 2012)*, (Banff, Alberta, Canada), 2012.

[41] C. Daley, S. Alawneh, D. Peters, B. Quinton, and B. Colbourne, "GPU modeling of ship operations in pack ice," in *The International Conference and Exhibition on Performance of Ships and Structures in Ice (ICETECH 2012)*, (Banff, Alberta, Canada), 2012.

[42] G. Vachon, M. Sayed, and I. Kubat, "Methodology for determination of ice management efficiency," in *The International Conference and Exhibition on Performance of Ships and Structures in Ice (ICETECH 2012)*, (Banff, Alberta, Canada), 2012.

[43] M. Sayed, I. Kubat, B. Wright, A. Iyerusalimskiy, A. Phadke, and B. Hall, "Numerical simulations of ice interaction with a moored struc-

ture," in *The International Conference and Exhibition on Performance of Ships and Structures in Ice (ICETECH 2012)*, (Banff, Alberta, Canada), 2012.

[44] M. Sayed, I. K. Kubat, and B. Wright, "Numerical simulations of ice forces on the kulluk: the role of ice confinement, ice pressure and ice management," in *Proceedings of OTC Arctic Technology Conference*, (Houston, Texas, USA), 2012.

[45] A. Gürtner, B. Bjørnsen, T. H. Amdahl, S. R. Søberg, and S. H. Teigen, "Numerical simulations of managed ice loads on a moored Arctic drillship," in *Proceedings of OTC Arctic Technology Conference*, (Houston, Texas, USA), 2012.

[46] I. Metrikin, S. Løset, N. A. Jenssen, and S. Kerkeni, "Numerical simulation of dynamic positioning in ice," *Marine Technology Society Journal*, vol. 47, no. 2, pp. 14–30, 2013.

[47] B. Wright *et al.*, "Evaluation of full scale data for moored vessel station-keeping in pack ice," *PERD/CHC Report*, pp. 26–200, 1999.

[48] M. Steele, J. H. Morison, and N. Untersteiner, "The partition of air-ice-ocean momentum exchange as a function of ice concentration, floe size, and draft," *Journal of Geophysical Research: Oceans (1978–2012)*, vol. 94, no. C9, pp. 12739–12750, 1989.

[49] M. Steele, "Sea ice melting and floe geometry in a simple ice-ocean model," *Journal of Geophysical Research: Oceans (1978–2012)*, vol. 97, no. C11, pp. 17729–17738, 1992.

[50] Q. Zhang, S. van der Werff, I. Metrikin, S. Løset, and R. Skjetne, "Image processing for the analysis of an evolving broken-ice field in model testing," in *ASME 2012 31st International Conference on Ocean, Offshore and Arctic Engineering*, pp. 597–605, American Society of Mechanical Engineers, 2012.

[51] A. Haase, S. van der Werff, and P. Jochmann, "Dypic-dynamic positioning in ice: First phase of model testing," in *ASME 2012 31st International Conference on Ocean, Offshore and Arctic Engineering*, pp. 487–494, American Society of Mechanical Engineers, 2012.

[52] CryoWing technical specifications, accessed 2012-03-30. `http://uas.norut.no/UAV_Remote_Sensing/CryoWing.html`.

[53] CryoWing unmanned aerial system, accessed 2012-03-30. `http://uas.norut.no/UAV_Remote_Sensing/Welcome.html`.

[54] Q. Zhang, R. Skjetne, and B. Su, "Automatic image segmentation for boundary detection of apparently connected sea-ice floes," in *Proceedings of the 22nd International Conference on Port and Ocean Engineering under Arctic Conditions*, (Espoo, Finland), 2013.

[55] Q. Zhang, R. Skjetne, I. Metrikin, and S. Løset, "Image processing for ice floe analyses in broken-ice model testing," *Cold Regions Science and Technology*, vol. 111, pp. 27–38, 2015.

[56] Q. Zhang and R. Skjetne, "Image processing for identification of sea-ice floes and the floe size distributions," *IEEE Transactions on Geoscience and Remote Sensing*, vol. 53, no. 5, pp. 2913–2924, 2015.

[57] Q. Zhang and R. Skjetne, "Image techniques for identifying sea-ice parameters," *Modeling, Identification and Control*, vol. 35, no. 4, pp. 293–301, 2014.

[58] N. Otsu, "A threshold selection method from gray-level histograms," *Automatica*, vol. 11, no. 285-296, pp. 23–27, 1975.

[59] R. C. Gonzalez and R. E. Woods, *Digital Image Processing*. Boston, MA, USA: Addison-Wesley Longman Publishing Co., Inc., 2nd ed., 2001.

[60] M. R. Anderberg, "Cluster analysis for applications," tech. rep., DTIC Document, 1973.

[61] S. C. Basak, V. Magnuson, G. Niemi, and R. Regal, "Determining structural similarity of chemicals using graph-theoretic indices," *Discrete Applied Mathematics*, vol. 19, no. 1, pp. 17–44, 1988.

[62] J. MacQueen *et al.*, "Some methods for classification and analysis of multivariate observations," in *Proceedings of the fifth Berkeley symposium on mathematical statistics and probability*, vol. 1, p. 14, California, USA, 1967.

[63] R. C. Gonzalez, R. E. Woods, and S. L. Eddins, *Digital Image Processing Using MATLAB*. Upper Saddle River, NJ, USA: Prentice-Hall, Inc., 2003.

[64] J.-F. Rivest, P. Soille, and S. Beucher, "Morphological gradients," *Journal of Electronic Imaging*, vol. 2, no. 4, pp. 326–336, 1993.

[65] A. Talukder, D. P. Casasent, H.-W. Lee, P. M. Keagy, and T. F. Schatzki, "Modified binary watershed transform for segmentation of agricultural products," in *Photonics East (ISAM, VVDC, IEMB)*, pp. 53–64, International Society for Optics and Photonics, 1999.

[66] X. Chen, X. Zhou, and S. T. Wong, "Automated segmentation, classification, and tracking of cancer cell nuclei in time-lapse microscopy," *IEEE Transactions on Biomedical Engineering*, vol. 53, no. 4, pp. 762–766, 2006.

[67] J. Blunt, V. Garas, D. Matskevitch, J. Hamilton, and K. Kumaran, "Image analysis techniques for high Arctic, deepwater operation support," in *OTC Arctic Technology Conference*, (Houston, Texas, USA), 2012.

[68] A. M. Ghalib and R. D. Hryciw, "Soil particle size distribution by mosaic imaging and watershed analysis," *Journal of Computing in Civil Engineering*, vol. 13, no. 2, pp. 80–87, 1999.

[69] X. Yang, H. Li, and X. Zhou, "Nuclei segmentation using marker-controlled watershed, tracking using mean-shift, and kalman filter in time-lapse microscopy," *IEEE Transactions on Circuits and Systems I: Regular Papers*, vol. 53, no. 11, pp. 2405–2414, 2006.

[70] N. Malpica, C. Ortiz de Solorzano, J. J. Vaquero, A. Santos, I. Vallcorba, J. M. Garcia-Sagredo, and F. d. Pozo, "Applying watershed algorithms to the segmentation of clustered nuclei," *Cytometry*, vol. 28, pp. 289–297, 1997.

[71] Z. Lu and T. Tong, "The application of chain code sum in the edge form analysis," *China Journal of Image and Graphics*, vol. 7, no. 12, pp. 1323–1328, 2002. in Chinese.

[72] H. Freeman and L. S. Davis, "A corner-finding algorithm for chain-coded curves," *IEEE Transactions on Computers*, vol. 26, no. 3, pp. 297–303, 1977.

[73] T. Toyota, S. Takatsuji, and M. Nakayama, "Characteristics of sea ice floe size distribution in the seasonal ice zone," *Geophysical research letters*, vol. 33, no. 2, p. L02616, 2006.

[74] T. Toyota, C. Haas, and T. Tamura, "Size distribution and shape properties of relatively small sea-ice floes in the Antarctic marginal ice zone in late winter," *Deep Sea Research Part II: Topical Studies in Oceanography*, vol. 58, no. 9, pp. 1182–1193, 2011.

[75] J. Banfield, "Automated tracking of ice floes: A stochastic approach," *IEEE Transactions on Geoscience and Remote Sensing*, vol. 29, no. 6, pp. 905–911, 1991.

[76] J. D. Banfield and A. E. Raftery, "Ice floe identification in satellite images using mathematical morphology and clustering about principal curves,"

Journal of the American Statistical Association, vol. 87, no. 417, pp. 7–16, 1992.

[77] M. Kass, A. Witkin, and D. Terzopoulos, "Snakes: Active contour models," *International Journal of Computer Vision*, vol. 1, no. 4, pp. 321–331, 1988.

[78] C. Xu and J. L. Prince, "Snakes, shapes, and gradient vector flow," *IEEE Transactions on Image Processing*, vol. 7, no. 3, pp. 359–369, 1998.

[79] C. Xu and J. L. Prince, accessed 2014-09-23. `http://www.iacl.ece.jhu.edu/static/gvf/`.

[80] A. Rosenfeld and J. L. Pfaltz, "Sequential operations in digital picture processing," *Journal of the ACM (JACM)*, vol. 13, no. 4, pp. 471–494, 1966.

[81] A. Rosenfeld and J. L. Pfaltz, "Distance functions on digital pictures," *Pattern Recognition*, vol. 1, no. 1, pp. 33–61, 1968.

[82] L.-K. Soh, C. Tsatsoulis, and B. Holt, "Identifying ice floes and computing ice floe distributions in SAR images," in *Analysis of SAR Data of the Polar Oceans*, pp. 9–34, Springer, 1998.

[83] P. Wadhams, *Ice in the Ocean*. Taylor & Francis, 2000.

[84] WMO SEA-ICE NOMENCLATURE, accessed 2014-08-31. `http://www.aari.ru/gdsidb/XML/volume1.php?lang1=0&arrange=4`.

[85] T. Lippmann and R. A. Holman, "Quantification of sand bar morphology: A video technique based on wave dissipation," *Journal of Geophysical Research: Oceans (1978–2012)*, vol. 94, no. C1, pp. 995–1011, 1989.

[86] P. Smith, "Bilinear interpolation of digital images," *Ultramicroscopy*, vol. 6, no. 2, pp. 201–204, 1981.

[87] GoPro, "HD HERO2 PROFESSIONAL," accessed 2014-11-22. `http://gopro.com/product-comparison-hd-hero2-hd-hero-cameras`.

[88] H. Bjørklund, A. Prusakov, and A. Sinitsyn, "360 degree camera system," tech. rep., Department of Civil and Transport Engineering, Norwegian University of Science and Technology, 2013.

[89] E. Alpaydin, *Introduction to machine learning*. MIT press, 2014.

Previous PhD theses published at the Departement of Marine Technology (earlier: Faculty of Marine Technology) NORWEGIAN UNIVERSITY OF SCIENCE AND TECHNOLOGY

Report No.	Author	Title
	Kavlie, Dag	Optimization of Plane Elastic Grillages, 1967
	Hansen, Hans R.	Man-Machine Communication and Data-Storage Methods in Ship Structural Design, 1971
	Gisvold, Kaare M.	A Method for non-linear mixed -integer programming and its Application to Design Problems, 1971
	Lund, Sverre	Tanker Frame Optimalization by means of SUMT-Transformation and Behaviour Models, 1971
	Vinje, Tor	On Vibration of Spherical Shells Interacting with Fluid, 1972
	Lorentz, Jan D.	Tank Arrangement for Crude Oil Carriers in Accordance with the new Anti-Pollution Regulations, 1975
	Carlsen, Carl A.	Computer-Aided Design of Tanker Structures, 1975
	Larsen, Carl M.	Static and Dynamic Analysis of Offshore Pipelines during Installation, 1976
UR-79-01	Brigt Hatlestad, MK	The finite element method used in a fatigue evaluation of fixed offshore platforms. (Dr.Ing. Thesis)
UR-79-02	Erik Pettersen, MK	Analysis and design of cellular structures. (Dr.Ing. Thesis)
UR-79-03	Sverre Valsgård, MK	Finite difference and finite element methods applied to nonlinear analysis of plated structures. (Dr.Ing. Thesis)
UR-79-04	Nils T. Nordsve, MK	Finite element collapse analysis of structural members considering imperfections and stresses due to fabrication. (Dr.Ing. Thesis)
UR-79-05	Ivar J. Fylling, MK	Analysis of towline forces in ocean towing systems. (Dr.Ing. Thesis)
UR-80-06	Nils Sandsmark, MM	Analysis of Stationary and Transient Heat Conduction by the Use of the Finite Element Method. (Dr.Ing. Thesis)

UR-80-09	Sverre Haver, MK	Analysis of uncertainties related to the stochastic modeling of ocean waves. (Dr.Ing. Thesis)
UR-81-15	Odland, Jonas	On the Strength of welded Ring stiffened cylindrical Shells primarily subjected to axial Compression
UR-82-17	Engesvik, Knut	Analysis of Uncertainties in the fatigue Capacity of Welded Joints
UR-82-18	Rye, Henrik	Ocean wave groups
UR-83-30	Eide, Oddvar Inge	On Cumulative Fatigue Damage in Steel Welded Joints
UR-83-33	Mo, Olav	Stochastic Time Domain Analysis of Slender Offshore Structures
UR-83-34	Amdahl, Jørgen	Energy absorption in Ship-platform impacts
UR-84-37	Mørch, Morten	Motions and mooring forces of semi submersibles as determined by full-scale measurements and theoretical analysis
UR-84-38	Soares, C. Guedes	Probabilistic models for load effects in ship structures
UR-84-39	Aarsnes, Jan V.	Current forces on ships
UR-84-40	Czujko, Jerzy	Collapse Analysis of Plates subjected to Biaxial Compression and Lateral Load
UR-85-46	Alf G. Engseth, MK	Finite element collapse analysis of tubular steel offshore structures. (Dr.Ing. Thesis)
UR-86-47	Dengody Sheshappa, MP	A Computer Design Model for Optimizing Fishing Vessel Designs Based on Techno-Economic Analysis. (Dr.Ing. Thesis)
UR-86-48	Vidar Aanesland, MH	A Theoretical and Numerical Study of Ship Wave Resistance. (Dr.Ing. Thesis)
UR-86-49	Heinz-Joachim Wessel, MK	Fracture Mechanics Analysis of Crack Growth in Plate Girders. (Dr.Ing. Thesis)
UR-86-50	Jon Taby, MK	Ultimate and Post-ultimate Strength of Dented Tubular Members. (Dr.Ing. Thesis)
UR-86-51	Walter Lian, MH	A Numerical Study of Two-Dimensional Separated Flow Past Bluff Bodies at Moderate KC-Numbers. (Dr.Ing. Thesis)
UR-86-52	Bjørn Sortland, MH	Force Measurements in Oscillating Flow on Ship Sections and Circular Cylinders in a U-Tube Water

		Tank. (Dr.Ing. Thesis)
UR-86-53	Kurt Strand, MM	A System Dynamic Approach to One-dimensional Fluid Flow. (Dr.Ing. Thesis)
UR-86-54	Arne Edvin Løken, MH	Three Dimensional Second Order Hydrodynamic Effects on Ocean Structures in Waves. (Dr.Ing. Thesis)
UR-86-55	Sigurd Falch, MH	A Numerical Study of Slamming of Two-Dimensional Bodies. (Dr.Ing. Thesis)
UR-87-56	Arne Braathen, MH	Application of a Vortex Tracking Method to the Prediction of Roll Damping of a Two-Dimension Floating Body. (Dr.Ing. Thesis)
UR-87-57	Bernt Leira, MK	Gaussian Vector Processes for Reliability Analysis involving Wave-Induced Load Effects. (Dr.Ing. Thesis)
UR-87-58	Magnus Småvik, MM	Thermal Load and Process Characteristics in a Two-Stroke Diesel Engine with Thermal Barriers (in Norwegian). (Dr.Ing. Thesis)
MTA-88-59	Bernt Arild Bremdal, MP	An Investigation of Marine Installation Processes – A Knowledge - Based Planning Approach. (Dr.Ing. Thesis)
MTA-88-60	Xu Jun, MK	Non-linear Dynamic Analysis of Space-framed Offshore Structures. (Dr.Ing. Thesis)
MTA-89-61	Gang Miao, MH	Hydrodynamic Forces and Dynamic Responses of Circular Cylinders in Wave Zones. (Dr.Ing. Thesis)
MTA-89-62	Martin Greenhow, MH	Linear and Non-Linear Studies of Waves and Floating Bodies. Part I and Part II. (Dr.Techn. Thesis)
MTA-89-63	Chang Li, MH	Force Coefficients of Spheres and Cubes in Oscillatory Flow with and without Current. (Dr.Ing. Thesis
MTA-89-64	Hu Ying, MP	A Study of Marketing and Design in Development of Marine Transport Systems. (Dr.Ing. Thesis)
MTA-89-65	Arild Jæger, MH	Seakeeping, Dynamic Stability and Performance of a Wedge Shaped Planing Hull. (Dr.Ing. Thesis)
MTA-89-66	Chan Siu Hung, MM	The dynamic characteristics of tilting-pad bearings
MTA-89-67	Kim Wikstrøm, MP	Analysis av projekteringen for ett offshore projekt. (Licenciat-avhandling)
MTA-89-68	Jiao Guoyang, MK	Reliability Analysis of Crack Growth under Random Loading, considering Model Updating.

		(Dr.Ing. Thesis)
MTA-89-69	Arnt Olufsen, MK	Uncertainty and Reliability Analysis of Fixed Offshore Structures. (Dr.Ing. Thesis)
MTA-89-70	Wu Yu-Lin, MR	System Reliability Analyses of Offshore Structures using improved Truss and Beam Models. (Dr.Ing. Thesis)
MTA-90-71	Jan Roger Hoff, MH	Three-dimensional Green function of a vessel with forward speed in waves. (Dr.Ing. Thesis)
MTA-90-72	Rong Zhao, MH	Slow-Drift Motions of a Moored Two-Dimensional Body in Irregular Waves. (Dr.Ing. Thesis)
MTA-90-73	Atle Minsaas, MP	Economical Risk Analysis. (Dr.Ing. Thesis)
MTA-90-74	Knut-Aril Farnes, MK	Long-term Statistics of Response in Non-linear Marine Structures. (Dr.Ing. Thesis)
MTA-90-75	Torbjørn Sotberg, MK	Application of Reliability Methods for Safety Assessment of Submarine Pipelines. (Dr.Ing. Thesis)
MTA-90-76	Zeuthen, Steffen, MP	SEAMAID. A computational model of the design process in a constraint-based logic programming environment. An example from the offshore domain. (Dr.Ing. Thesis)
MTA-91-77	Haagensen, Sven, MM	Fuel Dependant Cyclic Variability in a Spark Ignition Engine - An Optical Approach. (Dr.Ing. Thesis)
MTA-91-78	Løland, Geir, MH	Current forces on and flow through fish farms. (Dr.Ing. Thesis)
MTA-91-79	Hoen, Christopher, MK	System Identification of Structures Excited by Stochastic Load Processes. (Dr.Ing. Thesis)
MTA-91-80	Haugen, Stein, MK	Probabilistic Evaluation of Frequency of Collision between Ships and Offshore Platforms. (Dr.Ing. Thesis)
MTA-91-81	Sødahl, Nils, MK	Methods for Design and Analysis of Flexible Risers. (Dr.Ing. Thesis)
MTA-91-82	Ormberg, Harald, MK	Non-linear Response Analysis of Floating Fish Farm Systems. (Dr.Ing. Thesis)
MTA-91-83	Marley, Mark J., MK	Time Variant Reliability under Fatigue Degradation. (Dr.Ing. Thesis)
MTA-91-84	Krokstad, Jørgen R., MH	Second-order Loads in Multidirectional Seas. (Dr.Ing. Thesis)

MTA-91-85	Molteberg, Gunnar A., MM	The Application of System Identification Techniques to Performance Monitoring of Four Stroke Turbocharged Diesel Engines. (Dr.Ing. Thesis)
MTA-92-86	Mørch, Hans Jørgen Bjelke, MH	Aspects of Hydrofoil Design: with Emphasis on Hydrofoil Interaction in Calm Water. (Dr.Ing. Thesis)
MTA-92-87	Chan Siu Hung, MM	Nonlinear Analysis of Rotordynamic Instabilities in Highspeed Turbomachinery. (Dr.Ing. Thesis)
MTA-92-88	Bessason, Bjarni, MK	Assessment of Earthquake Loading and Response of Seismically Isolated Bridges. (Dr.Ing. Thesis)
MTA-92-89	Langli, Geir, MP	Improving Operational Safety through exploitation of Design Knowledge - an investigation of offshore platform safety. (Dr.Ing. Thesis)
MTA-92-90	Sævik, Svein, MK	On Stresses and Fatigue in Flexible Pipes. (Dr.Ing. Thesis)
MTA-92-91	Ask, Tor Ø., MM	Ignition and Flame Growth in Lean Gas-Air Mixtures. An Experimental Study with a Schlieren System. (Dr.Ing. Thesis)
MTA-86-92	Hessen, Gunnar, MK	Fracture Mechanics Analysis of Stiffened Tubular Members. (Dr.Ing. Thesis)
MTA-93-93	Steinebach, Christian, MM	Knowledge Based Systems for Diagnosis of Rotating Machinery. (Dr.Ing. Thesis)
MTA-93-94	Dalane, Jan Inge, MK	System Reliability in Design and Maintenance of Fixed Offshore Structures. (Dr.Ing. Thesis)
MTA-93-95	Steen, Sverre, MH	Cobblestone Effect on SES. (Dr.Ing. Thesis)
MTA-93-96	Karunakaran, Daniel, MK	Nonlinear Dynamic Response and Reliability Analysis of Drag-dominated Offshore Platforms. (Dr.Ing. Thesis)
MTA-93-97	Hagen, Arnulf, MP	The Framework of a Design Process Language. (Dr.Ing. Thesis)
MTA-93-98	Nordrik, Rune, MM	Investigation of Spark Ignition and Autoignition in Methane and Air Using Computational Fluid Dynamics and Chemical Reaction Kinetics. A Numerical Study of Ignition Processes in Internal Combustion Engines. (Dr.Ing. Thesis)
MTA-94-99	Passano, Elizabeth, MK	Efficient Analysis of Nonlinear Slender Marine Structures. (Dr.Ing. Thesis)
MTA-94-100	Kvålsvold, Jan, MH	Hydroelastic Modelling of Wetdeck Slamming on Multihull Vessels. (Dr.Ing. Thesis)

MTA-94-102	Bech, Sidsel M., MK	Experimental and Numerical Determination of Stiffness and Strength of GRP/PVC Sandwich Structures. (Dr.Ing. Thesis)
MTA-95-103	Paulsen, Hallvard, MM	A Study of Transient Jet and Spray using a Schlieren Method and Digital Image Processing. (Dr.Ing. Thesis)
MTA-95-104	Hovde, Geir Olav, MK	Fatigue and Overload Reliability of Offshore Structural Systems, Considering the Effect of Inspection and Repair. (Dr.Ing. Thesis)
MTA-95-105	Wang, Xiaozhi, MK	Reliability Analysis of Production Ships with Emphasis on Load Combination and Ultimate Strength. (Dr.Ing. Thesis)
MTA-95-106	Ulstein, Tore, MH	Nonlinear Effects of a Flexible Stern Seal Bag on Cobblestone Oscillations of an SES. (Dr.Ing. Thesis)
MTA-95-107	Solaas, Frøydis, MH	Analytical and Numerical Studies of Sloshing in Tanks. (Dr.Ing. Thesis)
MTA-95-108	Hellan, Øyvind, MK	Nonlinear Pushover and Cyclic Analyses in Ultimate Limit State Design and Reassessment of Tubular Steel Offshore Structures. (Dr.Ing. Thesis)
MTA-95-109	Hermundstad, Ole A., MK	Theoretical and Experimental Hydroelastic Analysis of High Speed Vessels. (Dr.Ing. Thesis)
MTA-96-110	Bratland, Anne K., MH	Wave-Current Interaction Effects on Large-Volume Bodies in Water of Finite Depth. (Dr.Ing. Thesis)
MTA-96-111	Herfjord, Kjell, MH	A Study of Two-dimensional Separated Flow by a Combination of the Finite Element Method and Navier-Stokes Equations. (Dr.Ing. Thesis)
MTA-96-112	Æsøy, Vilmar, MM	Hot Surface Assisted Compression Ignition in a Direct Injection Natural Gas Engine. (Dr.Ing. Thesis)
MTA-96-113	Eknes, Monika L., MK	Escalation Scenarios Initiated by Gas Explosions on Offshore Installations. (Dr.Ing. Thesis)
MTA-96-114	Erikstad, Stein O., MP	A Decision Support Model for Preliminary Ship Design. (Dr.Ing. Thesis)
MTA-96-115	Pedersen, Egil, MH	A Nautical Study of Towed Marine Seismic Streamer Cable Configurations. (Dr.Ing. Thesis)
MTA-97-116	Moksnes, Paul O., MM	Modelling Two-Phase Thermo-Fluid Systems Using Bond Graphs. (Dr.Ing. Thesis)
MTA-97-117	Halse, Karl H., MK	On Vortex Shedding and Prediction of Vortex-Induced Vibrations of Circular Cylinders. (Dr.Ing.

		Thesis)
MTA-97-118	Igland, Ragnar T., MK	Reliability Analysis of Pipelines during Laying, considering Ultimate Strength under Combined Loads. (Dr.Ing. Thesis)
MTA-97-119	Pedersen, Hans-P., MP	Levendefiskteknologi for fiskefartøy. (Dr.Ing. Thesis)
MTA-98-120	Vikestad, Kyrre, MK	Multi-Frequency Response of a Cylinder Subjected to Vortex Shedding and Support Motions. (Dr.Ing. Thesis)
MTA-98-121	Azadi, Mohammad R. E., MK	Analysis of Static and Dynamic Pile-Soil-Jacket Behaviour. (Dr.Ing. Thesis)
MTA-98-122	Ulltang, Terje, MP	A Communication Model for Product Information. (Dr.Ing. Thesis)
MTA-98-123	Torbergsen, Erik, MM	Impeller/Diffuser Interaction Forces in Centrifugal Pumps. (Dr.Ing. Thesis)
MTA-98-124	Hansen, Edmond, MH	A Discrete Element Model to Study Marginal Ice Zone Dynamics and the Behaviour of Vessels Moored in Broken Ice. (Dr.Ing. Thesis)
MTA-98-125	Videiro, Paulo M., MK	Reliability Based Design of Marine Structures. (Dr.Ing. Thesis)
MTA-99-126	Mainçon, Philippe, MK	Fatigue Reliability of Long Welds Application to Titanium Risers. (Dr.Ing. Thesis)
MTA-99-127	Haugen, Elin M., MH	Hydroelastic Analysis of Slamming on Stiffened Plates with Application to Catamaran Wetdecks. (Dr.Ing. Thesis)
MTA-99-128	Langhelle, Nina K., MK	Experimental Validation and Calibration of Nonlinear Finite Element Models for Use in Design of Aluminium Structures Exposed to Fire. (Dr.Ing. Thesis)
MTA-99-129	Berstad, Are J., MK	Calculation of Fatigue Damage in Ship Structures. (Dr.Ing. Thesis)
MTA-99-130	Andersen, Trond M., MM	Short Term Maintenance Planning. (Dr.Ing. Thesis)
MTA-99-131	Tveiten, Bård Wathne, MK	Fatigue Assessment of Welded Aluminium Ship Details. (Dr.Ing. Thesis)
MTA-99-132	Søreide, Fredrik, MP	Applications of underwater technology in deep water archaeology. Principles and practice. (Dr.Ing. Thesis)
MTA-99-133	Tønnessen, Rune, MH	A Finite Element Method Applied to Unsteady Viscous Flow Around 2D Blunt Bodies With

		Sharp Corners. (Dr.Ing. Thesis)
MTA-99-134	Elvekrok, Dag R., MP	Engineering Integration in Field Development Projects in the Norwegian Oil and Gas Industry. The Supplier Management of Norne. (Dr.Ing. Thesis)
MTA-99-135	Fagerholt, Kjetil, MP	Optimeringsbaserte Metoder for Ruteplanlegging innen skipsfart. (Dr.Ing. Thesis)
MTA-99-136	Bysveen, Marie, MM	Visualization in Two Directions on a Dynamic Combustion Rig for Studies of Fuel Quality. (Dr.Ing. Thesis)
MTA-2000-137	Storteig, Eskild, MM	Dynamic characteristics and leakage performance of liquid annular seals in centrifugal pumps. (Dr.Ing. Thesis)
MTA-2000-138	Sagli, Gro, MK	Model uncertainty and simplified estimates of long term extremes of hull girder loads in ships. (Dr.Ing. Thesis)
MTA-2000-139	Tronstad, Harald, MK	Nonlinear analysis and design of cable net structures like fishing gear based on the finite element method. (Dr.Ing. Thesis)
MTA-2000-140	Kroneberg, André, MP	Innovation in shipping by using scenarios. (Dr.Ing. Thesis)
MTA-2000-141	Haslum, Herbjørn Alf, MH	Simplified methods applied to nonlinear motion of spar platforms. (Dr.Ing. Thesis)
MTA-2001-142	Samdal, Ole Johan, MM	Modelling of Degradation Mechanisms and Stressor Interaction on Static Mechanical Equipment Residual Lifetime. (Dr.Ing. Thesis)
MTA-2001-143	Baarholm, Rolf Jarle, MH	Theoretical and experimental studies of wave impact underneath decks of offshore platforms. (Dr.Ing. Thesis)
MTA-2001-144	Wang, Lihua, MK	Probabilistic Analysis of Nonlinear Wave-induced Loads on Ships. (Dr.Ing. Thesis)
MTA-2001-145	Kristensen, Odd H. Holt, MK	Ultimate Capacity of Aluminium Plates under Multiple Loads, Considering HAZ Properties. (Dr.Ing. Thesis)
MTA-2001-146	Greco, Marilena, MH	A Two-Dimensional Study of Green-Water Loading. (Dr.Ing. Thesis)
MTA-2001-147	Heggelund, Svein E., MK	Calculation of Global Design Loads and Load Effects in Large High Speed Catamarans. (Dr.Ing. Thesis)
MTA-2001-148	Babalola, Olusegun T., MK	Fatigue Strength of Titanium Risers – Defect

		Sensitivity. (Dr.Ing. Thesis)
MTA-2001-149	Mohammed, Abuu K., MK	Nonlinear Shell Finite Elements for Ultimate Strength and Collapse Analysis of Ship Structures. (Dr.Ing. Thesis)
MTA-2002-150	Holmedal, Lars E., MH	Wave-current interactions in the vicinity of the sea bed. (Dr.Ing. Thesis)
MTA-2002-151	Rognebakke, Olav F., MH	Sloshing in rectangular tanks and interaction with ship motions. (Dr.Ing. Thesis)
MTA-2002-152	Lader, Pål Furset, MH	Geometry and Kinematics of Breaking Waves. (Dr.Ing. Thesis)
MTA-2002-153	Yang, Qinzheng, MH	Wash and wave resistance of ships in finite water depth. (Dr.Ing. Thesis)
MTA-2002-154	Melhus, Øyvin, MM	Utilization of VOC in Diesel Engines. Ignition and combustion of VOC released by crude oil tankers. (Dr.Ing. Thesis)
MTA-2002-155	Ronæss, Marit, MH	Wave Induced Motions of Two Ships Advancing on Parallel Course. (Dr.Ing. Thesis)
MTA-2002-156	Økland, Ole D., MK	Numerical and experimental investigation of whipping in twin hull vessels exposed to severe wet deck slamming. (Dr.Ing. Thesis)
MTA-2002-157	Ge, Chunhua, MK	Global Hydroelastic Response of Catamarans due to Wet Deck Slamming. (Dr.Ing. Thesis)
MTA-2002-158	Byklum, Eirik, MK	Nonlinear Shell Finite Elements for Ultimate Strength and Collapse Analysis of Ship Structures. (Dr.Ing. Thesis)
IMT-2003-1	Chen, Haibo, MK	Probabilistic Evaluation of FPSO-Tanker Collision in Tandem Offloading Operation. (Dr.Ing. Thesis)
IMT-2003-2	Skaugset, Kjetil Bjørn, MK	On the Suppression of Vortex Induced Vibrations of Circular Cylinders by Radial Water Jets. (Dr.Ing. Thesis)
IMT-2003-3	Chezhian, Muthu	Three-Dimensional Analysis of Slamming. (Dr.Ing. Thesis)
IMT-2003-4	Buhaug, Øyvind	Deposit Formation on Cylinder Liner Surfaces in Medium Speed Engines. (Dr.Ing. Thesis)
IMT-2003-5	Tregde, Vidar	Aspects of Ship Design: Optimization of Aft Hull with Inverse Geometry Design. (Dr.Ing. Thesis)
IMT-2003-6	Wist, Hanne Therese	Statistical Properties of Successive Ocean Wave

		Parameters. (Dr.Ing. Thesis)
IMT-2004-7	Ransau, Samuel	Numerical Methods for Flows with Evolving Interfaces. (Dr.Ing. Thesis)
IMT-2004-8	Soma, Torkel	Blue-Chip or Sub-Standard. A data interrogation approach of identity safety characteristics of shipping organization. (Dr.Ing. Thesis)
IMT-2004-9	Ersdal, Svein	An experimental study of hydrodynamic forces on cylinders and cables in near axial flow. (Dr.Ing. Thesis)
IMT-2005-10	Brodtkorb, Per Andreas	The Probability of Occurrence of Dangerous Wave Situations at Sea. (Dr.Ing. Thesis)
IMT-2005-11	Yttervik, Rune	Ocean current variability in relation to offshore engineering. (Dr.Ing. Thesis)
IMT-2005-12	Fredheim, Arne	Current Forces on Net-Structures. (Dr.Ing. Thesis)
IMT-2005-13	Heggernes, Kjetil	Flow around marine structures. (Dr.Ing. Thesis
IMT-2005-14	Fouques, Sebastien	Lagrangian Modelling of Ocean Surface Waves and Synthetic Aperture Radar Wave Measurements. (Dr.Ing. Thesis)
IMT-2006-15	Holm, Håvard	Numerical calculation of viscous free surface flow around marine structures. (Dr.Ing. Thesis)
IMT-2006-16	Bjørheim, Lars G.	Failure Assessment of Long Through Thickness Fatigue Cracks in Ship Hulls. (Dr.Ing. Thesis)
IMT-2006-17	Hansson, Lisbeth	Safety Management for Prevention of Occupational Accidents. (Dr.Ing. Thesis)
IMT-2006-18	Zhu, Xinying	Application of the CIP Method to Strongly Nonlinear Wave-Body Interaction Problems. (Dr.Ing. Thesis)
IMT-2006-19	Reite, Karl Johan	Modelling and Control of Trawl Systems. (Dr.Ing. Thesis)
IMT-2006-20	Smogeli, Øyvind Notland	Control of Marine Propellers. From Normal to Extreme Conditions. (Dr.Ing. Thesis)
IMT-2007-21	Storhaug, Gaute	Experimental Investigation of Wave Induced Vibrations and Their Effect on the Fatigue Loading of Ships. (Dr.Ing. Thesis)
IMT-2007-22	Sun, Hui	A Boundary Element Method Applied to Strongly Nonlinear Wave-Body Interaction Problems. (PhD Thesis, CeSOS)
IMT-2007-23	Rustad, Anne Marthine	Modelling and Control of Top Tensioned Risers.

		(PhD Thesis, CeSOS)
IMT-2007-24	Johansen, Vegar	Modelling flexible slender system for real-time simulations and control applications
IMT-2007-25	Wroldsen, Anders Sunde	Modelling and control of tensegrity structures. (PhD Thesis, CeSOS)
IMT-2007-26	Aronsen, Kristoffer Høye	An experimental investigation of in-line and combined inline and cross flow vortex induced vibrations. (Dr. avhandling, IMT)
IMT-2007-27	Gao, Zhen	Stochastic Response Analysis of Mooring Systems with Emphasis on Frequency-domain Analysis of Fatigue due to Wide-band Response Processes (PhD Thesis, CeSOS)
IMT-2007-28	Thorstensen, Tom Anders	Lifetime Profit Modelling of Ageing Systems Utilizing Information about Technical Condition. (Dr.ing. thesis, IMT)
IMT-2008-29	Refsnes, Jon Erling Gorset	Nonlinear Model-Based Control of Slender Body AUVs (PhD Thesis, IMT)
IMT-2008-30	Berntsen, Per Ivar B.	Structural Reliability Based Position Mooring. (PhD-Thesis, IMT)
IMT-2008-31	Ye, Naiquan	Fatigue Assessment of Aluminium Welded Box-stiffener Joints in Ships (Dr.ing. thesis, IMT)
IMT-2008-32	Radan, Damir	Integrated Control of Marine Electrical Power Systems. (PhD-Thesis, IMT)
IMT-2008-33	Thomassen, Paul	Methods for Dynamic Response Analysis and Fatigue Life Estimation of Floating Fish Cages. (Dr.ing. thesis, IMT)
IMT-2008-34	Pákozdi, Csaba	A Smoothed Particle Hydrodynamics Study of Two-dimensional Nonlinear Sloshing in Rectangular Tanks. (Dr.ing.thesis, IMT/ CeSOS)
IMT-2007-35	Grytøyr, Guttorm	A Higher-Order Boundary Element Method and Applications to Marine Hydrodynamics. (Dr.ing.thesis, IMT)
IMT-2008-36	Drummen, Ingo	Experimental and Numerical Investigation of Nonlinear Wave-Induced Load Effects in Containerships considering Hydroelasticity. (PhD thesis, CeSOS)
IMT-2008-37	Skejic, Renato	Maneuvering and Seakeeping of a Singel Ship and of Two Ships in Interaction. (PhD-Thesis, CeSOS)
IMT-2008-38	Harlem, Alf	An Age-Based Replacement Model for Repairable Systems with Attention to High-Speed Marine

		Diesel Engines. (PhD-Thesis, IMT)
IMT-2008-39	Alsos, Hagbart S.	Ship Grounding. Analysis of Ductile Fracture, Bottom Damage and Hull Girder Response. (PhD-thesis, IMT)
IMT-2008-40	Graczyk, Mateusz	Experimental Investigation of Sloshing Loading and Load Effects in Membrane LNG Tanks Subjected to Random Excitation. (PhD-thesis, CeSOS)
IMT-2008-41	Taghipour, Reza	Efficient Prediction of Dynamic Response for Flexible amd Multi-body Marine Structures. (PhD-thesis, CeSOS)
IMT-2008-42	Ruth, Eivind	Propulsion control and thrust allocation on marine vessels. (PhD thesis, CeSOS)
IMT-2008-43	Nystad, Bent Helge	Technical Condition Indexes and Remaining Useful Life of Aggregated Systems. PhD thesis, IMT
IMT-2008-44	Soni, Prashant Kumar	Hydrodynamic Coefficients for Vortex Induced Vibrations of Flexible Beams, PhD thesis, CeSOS
IMT-2009-45	Amlashi, Hadi K.K.	Ultimate Strength and Reliability-based Design of Ship Hulls with Emphasis on Combined Global and Local Loads. PhD Thesis, IMT
IMT-2009-46	Pedersen, Tom Arne	Bond Graph Modelling of Marine Power Systems. PhD Thesis, IMT
IMT-2009-47	Kristiansen, Trygve	Two-Dimensional Numerical and Experimental Studies of Piston-Mode Resonance. PhD-Thesis, CeSOS
IMT-2009-48	Ong, Muk Chen	Applications of a Standard High Reynolds Number Model and a Stochastic Scour Prediction Model for Marine Structures. PhD-thesis, IMT
IMT-2009-49	Hong, Lin	Simplified Analysis and Design of Ships subjected to Collision and Grounding. PhD-thesis, IMT
IMT-2009-50	Koushan, Kamran	Vortex Induced Vibrations of Free Span Pipelines, PhD thesis, IMT
IMT-2009-51	Korsvik, Jarl Eirik	Heuristic Methods for Ship Routing and Scheduling. PhD-thesis, IMT
IMT-2009-52	Lee, Jihoon	Experimental Investigation and Numerical in Analyzing the Ocean Current Displacement of Longlines. Ph.d.-Thesis, IMT.

IMT- 2009-53	Vestbøstad, Tone Gran	A Numerical Study of Wave-in-Deck Impact usin a Two-Dimensional Constrained Interpolation Profile Method, Ph.d.thesis, CeSOS.
IMT- 2009-54	Bruun, Kristine	Bond Graph Modelling of Fuel Cells for Marine Power Plants. Ph.d.-thesis, IMT
IMT 2009-55	Holstad, Anders	Numerical Investigation of Turbulence in a Sekwed Three-Dimensional Channel Flow, Ph.d.-thesis, IMT.
IMT 2009-56	Ayala-Uraga, Efren	Reliability-Based Assessment of Deteriorating Ship-shaped Offshore Structures, Ph.d.-thesis, IMT
IMT 2009-57	Kong, Xiangjun	A Numerical Study of a Damaged Ship in Beam Sea Waves. Ph.d.-thesis, IMT/CeSOS.
IMT 2010-58	Kristiansen, David	Wave Induced Effects on Floaters of Aquaculture Plants, Ph.d.-thesis, CeSOS.
IMT 2010-59	Ludvigsen, Martin	An ROV-Toolbox for Optical and Acoustic Scientific Seabed Investigation. Ph.d.-thesis IMT.
IMT 2010-60	Hals, Jørgen	Modelling and Phase Control of Wave-Energy Converters. Ph.d.thesis, CeSOS.
IMT 2010- 61	Shu, Zhi	Uncertainty Assessment of Wave Loads and Ultimate Strength of Tankers and Bulk Carriers in a Reliability Framework. Ph.d. Thesis, IMT/ CeSOS
IMT 2010-62	Shao, Yanlin	Numerical Potential-Flow Studies on Weakly-Nonlinear Wave-Body Interactions with/without Small Forward Speed, Ph.d.thesis,CeSOS.
IMT 2010-63	Califano, Andrea	Dynamic Loads on Marine Propellers due to Intermittent Ventilation. Ph.d.thesis, IMT.
IMT 2010-64	El Khoury, George	Numerical Simulations of Massively Separated Turbulent Flows, Ph.d.-thesis, IMT
IMT 2010-65	Seim, Knut Sponheim	Mixing Process in Dense Overflows with Emphasis on the Faroe Bank Channel Overflow. Ph.d.thesis, IMT
IMT 2010-66	Jia, Huirong	Structural Analysis of Intect and Damaged Ships in a Collission Risk Analysis Perspective. Ph.d.thesis CeSoS.
IMT 2010-67	Jiao, Linlin	Wave-Induced Effects on a Pontoon-type Very Large Floating Structures (VLFS). Ph.D.-thesis, CeSOS.
IMT 2010-68	Abrahamsen, Bjørn Christian	Sloshing Induced Tank Roof with Entrapped Air Pocket. Ph.d.thesis, CeSOS.

IMT 2011-69	Karimirad, Madjid	Stochastic Dynamic Response Analysis of Spar-Type Wind Turbines with Catenary or Taut Mooring Systems. Ph.d.-thesis, CeSOS.
IMT - 2011-70	Erlend Meland	Condition Monitoring of Safety Critical Valves. Ph.d.-thesis, IMT.
IMT – 2011-71	Yang, Limin	Stochastic Dynamic System Analysis of Wave Energy Converter with Hydraulic Power Take-Off, with Particular Reference to Wear Damage Analysis, Ph.d. Thesis, CeSOS.
IMT – 2011-72	Visscher, Jan	Application of Particla Image Velocimetry on Turbulent Marine Flows, Ph.d.Thesis, IMT.
IMT – 2011-73	Su, Biao	Numerical Predictions of Global and Local Ice Loads on Ships. Ph.d.Thesis, CeSOS.
IMT – 2011-74	Liu, Zhenhui	Analytical and Numerical Analysis of Iceberg Collision with Ship Structures. Ph.d.Thesis, IMT.
IMT – 2011-75	Aarsæther, Karl Gunnar	Modeling and Analysis of Ship Traffic by Observation and Numerical Simulation. Ph.d.Thesis, IMT.
Imt – 2011-76	Wu, Jie	Hydrodynamic Force Identification from Stochastic Vortex Induced Vibration Experiments with Slender Beams. Ph.d.Thesis, IMT.
Imt – 2011-77	Amini, Hamid	Azimuth Propulsors in Off-design Conditions. Ph.d.Thesis, IMT.
IMT – 2011-78	Nguyen, Tan-Hoi	Toward a System of Real-Time Prediction and Monitoring of Bottom Damage Conditions During Ship Grounding. Ph.d.thesis, IMT.
IMT- 2011-79	Tavakoli, Mohammad T.	Assessment of Oil Spill in Ship Collision and Grounding, Ph.d.thesis, IMT.
IMT- 2011-80	Guo, Bingjie	Numerical and Experimental Investigation of Added Resistance in Waves. Ph.d.Thesis, IMT.
IMT- 2011-81	Chen, Qiaofeng	Ultimate Strength of Aluminium Panels, considering HAZ Effects, IMT
IMT- 2012-82	Kota, Ravikiran S.	Wave Loads on Decks of Offshore Structures in Random Seas, CeSOS.
IMT- 2012-83	Sten, Ronny	Dynamic Simulation of Deep Water Drilling Risers with Heave Compensating System, IMT.

IMT-2012-84	Berle, Øyvind	Risk and resilience in global maritime supply chains, IMT.
IMT-2012-85	Fang, Shaoji	Fault Tolerant Position Mooring Control Based on Structural Reliability, CeSOS.
IMT-2012-86	You, Jikun	Numerical studies on wave forces and moored ship motions in intermediate and shallow water, CeSOS.
IMT-2012-87	Xiang ,Xu	Maneuvering of two interacting ships in waves, CeSOS
IMT-2012-88	Dong, Wenbin	Time-domain fatigue response and reliability analysis of offshore wind turbines with emphasis on welded tubular joints and gear components, CeSOS
IMT-2012-89	Zhu, Suji	Investigation of Wave-Induced Nonlinear Load Effects in Open Ships considering Hull Girder Vibrations in Bending and Torsion, CeSOS
IMT-2012-90	Zhou, Li	Numerical and Experimental Investigation of Station-keeping in Level Ice, CeSOS
IMT-2012-91	Ushakov, Sergey	Particulate matter emission characteristics from diesel enignes operating on conventional and alternative marine fuels, IMT
IMT-2013-1	Yin, Decao	Experimental and Numerical Analysis of Combined In-line and Cross-flow Vortex Induced Vibrations, CeSOS
IMT-2013-2	Kurniawan, Adi	Modelling and geometry optimisation of wave energy converters, CeSOS
IMT-2013-3	Al Ryati, Nabil	Technical condition indexes doe auxiliary marine diesel engines, IMT
IMT-2013-4	Firoozkoohi, Reza	Experimental, numerical and analytical investigation of the effect of screens on sloshing, CeSOS
IMT-2013-5	Ommani, Babak	Potential-Flow Predictions of a Semi-Displacement Vessel Including Applications to Calm Water Broaching, CeSOS
IMT-2013-6	Xing, Yihan	Modelling and analysis of the gearbox in a floating spar-type wind turbine, CeSOS
IMT-7-2013	Balland, Océane	Optimization models for reducing air emissions from ships, IMT
IMT-8-2013	Yang, Dan	Transitional wake flow behind an inclined flat plate-----Computation and analysis, IMT

IMT-9-2013	Abdillah, Suyuthi	Prediction of Extreme Loads and Fatigue Damage for a Ship Hull due to Ice Action, IMT
IMT-10-2013	Ramìrez, Pedro Agustìn Pèrez	Ageing management and life extension of technical systems- Concepts and methods applied to oil and gas facilities, IMT
IMT-11-2013	Chuang, Zhenju	Experimental and Numerical Investigation of Speed Loss due to Seakeeping and Maneuvering. IMT
IMT-12-2013	Etemaddar, Mahmoud	Load and Response Analysis of Wind Turbines under Atmospheric Icing and Controller System Faults with Emphasis on Spar Type Floating Wind Turbines, IMT
IMT-13-2013	Lindstad, Haakon	Strategies and measures for reducing maritime CO2 emissons, IMT
IMT-14-2013	Haris, Sabril	Damage interaction analysis of ship collisions, IMT
IMT-15-2013	Shainee, Mohamed	Conceptual Design, Numerical and Experimental Investigation of a SPM Cage Concept for Offshore Mariculture, IMT
IMT-16-2013	Gansel, Lars	Flow past porous cylinders and effects of biofouling and fish behavior on the flow in and around Atlantic salmon net cages, IMT
IMT-17-2013	Gaspar, Henrique	Handling Aspects of Complexity in Conceptual Ship Design, IMT
IMT-18-2013	Thys, Maxime	Theoretical and Experimental Investigation of a Free Running Fishing Vessel at Small Frequency of Encounter, CeSOS
IMT-19-2013	Aglen, Ida	VIV in Free Spanning Pipelines, CeSOS
IMT-1-2014	Song, An	Theoretical and experimental studies of wave diffraction and radiation loads on a horizontally submerged perforated plate, CeSOS
IMT-2-2014	Rogne, Øyvind Ygre	Numerical and Experimental Investigation of a Hinged 5-body Wave Energy Converter, CeSOS
IMT-3-2014	Dai, Lijuan	Safe and efficient operation and maintenance of offshore wind farms ,IMT
IMT-4-2014	Bachynski, Erin Elizabeth	Design and Dynamic Analysis of Tension Leg Platform Wind Turbines, CeSOS
IMT-5-2014	Wang, Jingbo	Water Entry of Freefall Wedged – Wedge motions and Cavity Dynamics, CeSOS

IMT-6-2014	Kim, Ekaterina	Experimental and numerical studies related to the coupled behavior of ice mass and steel structures during accidental collisions, IMT
IMT-7-2014	Tan, Xiang	Numerical investigation of ship's continuous-mode icebreaking in leverl ice, CeSOS
IMT-8-2014	Muliawan, Made Jaya	Design and Analysis of Combined Floating Wave and Wind Power Facilities, with Emphasis on Extreme Load Effects of the Mooring System, CeSOS
IMT-9-2014	Jiang, Zhiyu	Long-term response analysis of wind turbines with an emphasis on fault and shutdown conditions, IMT
IMT-10-2014	Dukan, Fredrik	ROV Motion Control Systems, IMT
IMT-11-2014	Grimsmo, Nils I.	Dynamic simulations of hydraulic cylinder for heave compensation of deep water drilling risers, IMT
IMT-12-2014	Kvittem, Marit I.	Modelling and response analysis for fatigue design of a semisubmersible wind turbine, CeSOS
IMT-13-2014	Akhtar, Juned	The Effects of Human Fatigue on Risk at Sea, IMT
IMT-14-2014	Syahroni, Nur	Fatigue Assessment of Welded Joints Taking into Account Effects of Residual Stress, IMT
IMT-1-2015	Bøckmann, Eirik	Wave Propulsion of ships, IMT
IMT-2-2015	Wang, Kai	Modelling and dynamic analysis of a semi-submersible floating vertical axis wind turbine, CeSOS
IMT-3-2015	Fredriksen, Arnt Gunvald	A numerical and experimental study of a two-dimensional body with moonpool in waves and current, CeSOS
IMT-4-2015	Jose Patricio Gallardo Canabes	Numerical studies of viscous flow around bluff bodies, IMT
IMT-5-2015	Vegard Longva	Formulation and application of finite element techniques for slender marine structures subjected to contact interactions, IMT
IMT-6-2015	Jacobus De Vaal	Aerodynamic modelling of floating wind turbines, CeSOS
IMT-7-2015	Fachri Nasution	Fatigue Performance of Copper Power Conductors, IMT

IMT-8-2015	Oleh I Karpa	Development of bivariate extreme value distributions for applications in marine technology,CeSOS
IMT-9-2015	Daniel de Almeida Fernandes	An output feedback motion control system for ROVs, AMOS
IMT-10-2015	Bo Zhao	Particle Filter for Fault Diagnosis: Application to Dynamic Positioning Vessel and Underwater Robotics, CeSOS
IMT-11-2015	Wenting Zhu	Impact of emission allocation in maritime transportation, IMT
IMT-12-2015	Amir Rasekhi Nejad	Dynamic Analysis and Design of Gearboxes in Offshore Wind Turbines in a Structural Reliability Perspective, CeSOS
IMT-13-2015	Arturo Jesùs Ortega Malca	Dynamic Response of Flexibles Risers due to Unsteady Slug Flow, CeSOS
IMT-14-2015	Dagfinn Husjord	Guidance and decision-support system for safe navigation of ships operating in close proximity, IMT
IMT-15-2015	Anirban Bhattacharyya	Ducted Propellers: Behaviour in Waves and Scale Effects, IMT
IMT-16-2015	Qin Zhang	Image Processing for Ice Parameter Identification in Ice Management, IMT